Controlling Adsorption of Surfactants, Polymers and Particles to Fluid/Fluid Interfaces with Interfacial Processing

Submitted in partial fulfillment of the requirements for

the degree of

Doctor of Philosophy

in

Chemical Engineering

Michael L. Davidson

B.S., Chemical Engineering, The Pennsylvania State University

Carnegie Mellon University
Pittsburgh, PA

April 2020

ACKNOWLEDGEMENTS

ABSTRACT

The properties of fluid/fluid interfaces control interfacial phenomena like wetting, foaming and coalescence. Interfacial properties like interfacial tension and dilatational elasticity vary with fluid choice and with the concentration, chemistry and structure of surface-active species adsorbed to the interface. Classical experiments of adsorption are useful to quantify surface activity with simple surfactants but are lacking for more complex systems. Furthermore, common tests of surface activity are often insufficient to describe interfacial phenomena as the phenomena introduce additional timescales that go uncaptured by classical experiments. To control interfacial phenomena, experiments must be augmented by processes that introduce timescales controllable by the researcher.

In this thesis, tools for interfacial processing are developed both to quantify adsorption in complex systems and to control an elusive interfacial phenomenon, spontaneous emulsification. Simple interfacial processing tests adsorption reversibility and better defines the adsorption of simple surfactants, polymers and colloidal particles. Strongly adsorbing species like polyelectrolytes and nanoparticles form irreversibly adsorbed layers at fluid/fluid interfaces. These layers can be processed with solvent, salt solutions and surfactants. Processing can be used on the front end to drive the adsorption of solvent-responsive molecules. By decreasing solvent quality, amphiphilic polypeptoids can be driven and eventually stranded at air/water interfaces. Finally, interfacial processing is used to control the rate of spontaneous emulsification, necessary to determine the mechanism behind the complex phenomenon.

TABLE OF CONTENTS

LIST OF TABLES

LIST OF FIGURES

CHAPTER 1

INTRODUCTION

1.1 BACKGROUND

Much of interfacial science seeks to relate molecular design of surfactants with interfacial phenomena via the study of interfacial properties. Colloquially, surfactant is an umbrella term that refers to many surface-active species. This goal contains two necessary steps. First, establish structure-property relationships between a surfactant (e.g., chemistry, structure, self-assembly) in the bulk and the properties of an interface (e.g., interfacial tension, surface coverage, dilatational elasticity) once the surfactant adsorbs. Second, determine how interfacial phenomena (e.g., foam stability, emulsion stability, spontaneous emulsification) depend on specific values of those same interfacial properties.

The first goal is the simpler of the two and is often accomplished with static and/or dynamic measurements of surface coverage, interfacial tension and interfacial mechanics. A typical experiment measures the equilibration of a clean interface, initially without any adsorbed species, with an adjacent solution of a known surfactant concentration. The change in interfacial properties during adsorption is referred to as adsorption dynamics or transients, and the final values are referred to as steady state or equilibrium. For fluid/fluid interfaces, common techniques include interfacial tensiometry,[1] neutron reflectometry,[2] ellipsometry[3] and shear[4] and dilatational[5] rheometry. These techniques are complementary, and a complete picture of surfactant adsorption is rarely provided solely by one of them.

Meeting the second goal is more complicated because interfacial phenomena introduce additional timescales beyond those that are measured in typical experiments. One such phenomenon is known as spontaneous emulsification, the spontaneous appearance of droplets (typically near a larger, liquid/liquid interface) of one liquid in another immiscible liquid without the addition of mechanical energy of the application of a thermal gradient.[6,7] Without spontaneous emulsification, surfactant adsorbs to the liquid/liquid interface until equilibrated. With spontaneous emulsification, the appearance of the droplets is potentially accompanied by surfactant adsorption to the droplet interface, transport of one liquid into the other through the larger interface and motion of the larger interface. It is therefore unclear if the interfaces during emulsification resemble those during the measurements without emulsification. The introduction of these additional timescales necessitates the augmentation of classical adsorption experiments with additional timescales, broadly referred to as interfacial processing.

This thesis uses interfacial processing to describe both equilibrium and nonequilibrium behavior of a broad range of surfactant species at fluid/fluid interfaces. Chapter 2 describes the dynamic and steady state adsorption of flexible, oil-soluble block copolymers to the dodecane/water interface. Interfacial processing enables the measurement of desorption dynamics, suggesting the origins of the relaxations of dilatational stresses. In Chapter 3, processing is broadly useful in determining the composition of air/water interfaces exposed to solutions of colloidal, polyelectrolyte/surfactant aggregates. The adsorption of amphiphilic

polypeptoids in Chapter 4 is controlled by solvent quality, which is dynamically changed with processing. In Chapter 5, irreversibly adsorbed core-shell particles are processed with salt solutions to modulate surface coverage. Finally, interfacial processing in Chapter 6 is used to control the rate of spontaneous emulsification of dodecane/water interfaces with a silicone polyether.

1.2 MICROTENSIOMETER PLATFORM

Measurements of interfacial tension and dilatational modulus are made using a microtensiometer platform, shown in Figure 1.1 and described in detail elsewhere.[1,8–11] This platform is based on a capillary tensiometer and allows for efficient characterization of fluid/fluid interfaces of desirable curvature (radius of curvature between 15 and 150 μm) in response to changes in bulk solution, thus enabling quantitative modeling of adsorption and desorption kinetics. A thermoplastic cell houses a small fluid reservoir (up to 3 mL), two flow ports for the exchange of reservoir solution, and a glass capillary filled with air, water or oil submerged in the reservoir fluid (water or oil). The cell rests on an inverted light microscope, where a digital camera (Point Grey Flea) images the spherical fluid/fluid interface at the capillary tip. A pressure transducer, in line with the air inside the capillary, measures the pressure drop across the interface. Dynamic surface tension γ is determined by the Laplace equation,

$$\gamma = \frac{\Delta P \cdot R}{2},$$
(1.1)

where ΔP is the Laplace pressure across the interface and R is the radius of curvature of the spherical cap. New interfaces are generated after jettisoning the existing interface by pulsing the pressure within the capillary fluid. For
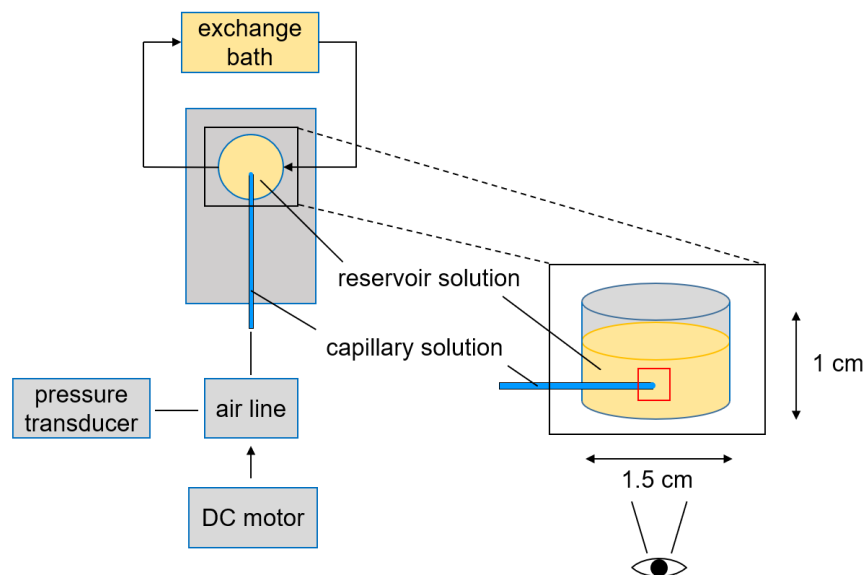
Figure 1.1. Schematic of microtensiometer platform. The spherical cap is imaged from below.

liquid/liquid systems, the field of view is cleared of the previous interface (now a droplet) with gentle motion of a metal syringe tip (wetted by oil) or of a Pasteur pipette (wetted by water). In both cases, a brief convective flow disturbs the first ~ 10 s of dynamics.[12] Bulk solution is exchanged with a bath via two reservoir ports connected to a peristaltic pump.

Glass capillaries (i.d. = 0.75 mm, o.d. = 1 mm, and L = 150 mm) are purchased from World Precision Instruments, Inc. (Sarasota, FL) and pulled to a tip radius below 50 μm using a PMP-102 capillary puller (MicroData Instrument, Inc., South Plainfield, NJ). The capillary exterior is cleaned with 200 proof ethanol before pulling. For oil/water systems, interfaces are defined to be either concave or convex from the perspective of the oil-soluble surfactants. For experiments with convex interfaces (oil/surfactant in the reservoir, water in the capillary), the capillary interior is acid-washed. For experiments with concave interfaces (oil/surfactant in the capillary, water in the reservoir), acid-washed capillaries are

4

hydrophobized using XIAMETER® OFS-6124 purchased from Dow Corning (Midland, MI) following manufacturer instructions.   Acid washing and hydrophobization help to keep the fluid/fluid/glass contact line from moving during an experiment. For air or oil within the capillary, interior pinning of the spherical interface is expected. That is, the air(oil)/water/glass contact line is at the smaller diameter of the pulled capillary tip. For water within the capillary, interior pinning usually occurs for the first several interfaces generated before transitioning to exterior pinning, where the oil/water/glass contact line as at the larger diameter of the pulled capillary tip.

Dilatational properties were determined by measuring the change in surface area of the spherical air/water interface during a prescribed low-amplitude pressure oscillation.   The dilatational modulus E is defined as the change in interfacial tension γ with interfacial area A,

$$E = \frac{d\gamma}{d \ln A} \quad .$$
(1.2)

The surface area of the spherical cap is calculated knowing the capillary radius R_c according to

$$A = 2\pi R\left(R - \sqrt{R^2 - R_C^2}\right) \quad .$$
(1.3)

The complex, dilatational modulus can be expressed as either a combination of elastic, E', and viscous, E'', components or as a magnitude, $|E^*|$, and a phase angle, θ, as

$$E = E' + iE'' = \left|E^*\right|e^{i\theta}.$$
(1.4)

A detailed description of the methodology used to determine E is given elsewhere.[5]

(1)   Alvarez, N. J.; Walker, L. M.; Anna, S. L. *Langmuir* **2010**, *26* (16), 13310–13319.

(2)   Campbell, R. A.; Angus-Smyth, A.; Yanez Arteta, M.; Tonigold, K.; Nylander, T.; Varga, I. *J. Phys. Chem. Lett.* **2010**, *1* (20), 3021–3026.

(3)   Ramírez, P.; Stocco, A.; Muñoz, J.; Miller, R. *J. Colloid Interface Sci.* **2012**, *378* (1), 135–143.

(4)   Anseth, J. W.; Bialek, A.; Hill, R. M.; Fuller, G. G. *Langmuir* **2003**, *19* (16), 6349–6356.

(5)   Kotula, A. P.; Anna, S. L. *J. Rheol. (N. Y. N. Y).* **2015**, *59* (1), 85–117.

(6)   Rang, M.; Miller, C. *Prog. Colloid Polym. Sci.* **1998**, *109*, 101–117.

(7)   Solans, C.; Morales, D.; Homs, M. *Curr. Opin. Colloid Interface Sci.* **2016**, *22*, 88–93.

(8)   Alvarez, N. J.; Walker, L. M.; Anna, S. L. *Phys. Rev. E - Stat. Nonlinear, Soft Matter Phys.* **2010**, *82* (1), 1–8.

(9)   Reichert, M. D.; Walker, L. M. *Langmuir* **2013**, *29* (6), 1857–1867.

(10)   Reichert, M. D.; Walker, L. M. *J. Colloid Interface Sci.* **2015**, *449*, 480–487.

(11)   Kirby, S. M.; Zhang, X.; Russo, P. S.; Anna, S. L.; Walker, L. M. *Langmuir* **2016**, *32* (22), 5542–5551.

(12)   Alvarez, N. J.; Vogus, D. R.; Walker, L. M.; Anna, S. L. *J. Colloid Interface Sci.* **2012**, *372* (1), 183–191.

CHAPTER 2

TRANSPORT OF FLEXIBLE, OIL-SOLUBLE DIBLOCK AND BAB TRIBLOCK COPOLYMERS TO THE OIL/WATER INTERFACE

2.1 INTRODUCTION

The interfacial properties of poly(ethylene oxide)-containing (PEO-containing) amphiphilic block copolymers have been well studied at air/water interfaces[1–10] with some work done at oil/water interfaces.[11–16] Most of the work with PEO-containing block copolymers has used diblocks and ABA triblocks, where the A (PEO in water-soluble molecules) is lyophilic and B is lyophobic. For a water-soluble ABA triblock, the hydrophobic B block—often poly(propylene oxide) (PPO) or poly(butylene oxide) (PBO)—drives adsorption to the interface, and the hydrophilic A block forms a brush region that dominates the mechanical properties of the interface. The hydrophobic block collapses at the air/water interface, enabling the clear definition of an anchor region (B) and a brush region (A). Much fewer interfacial studies have been done with BAB triblocks.[17–19] For a BAB triblock, the middle block makes up the brush region. Because the brush of a BAB triblock is anchored to the interface at both ends, the interfacial properties of a BAB triblock should be more sensitive to the chain flexibility of the middle block than those of an ABA triblock.

The adsorption of any molecule to a surface requires a negative free energy of adsorption. For block copolymer amphiphiles, adsorption occurs when the favorable enthalpy of adsorption overcomes the decrease in entropy from the confinement of the polymer at the interface. The model by Scheutjens and Fleer[20,21] (SF theory) for predicting homopolymer adsorption to solid substrates has been

modified for amphiphilic block copolymers[22] and predicts two key features of adsorption. The first is that the adsorption of a diblock will increase linearly with the size of the strongly adsorbing block. Second, a triblock copolymer with the same composition of analogous diblocks will adsorb less strongly than the diblocks either due to packing constraints of dangling tails (ABA triblocks) or to the necessity of a soluble middle block to satisfy two anchor conditions on the substrate (BAB triblocks).

Much of the data of block copolymer adsorption to fluid/fluid interfaces is of water-soluble Pluronic® molecules, ABA triblocks of PEO-PPO-PEO. PEO-PPO-PEO block copolymers are known to self-assemble into micelles in aqueous solutions at a critical solution concentration, known as the critical micelle concentration (CMC),[2] a feature that is shared with smaller, aliphatic surfactants.[23] Below the CMC, adsorption increases monotonically with solution concentration. ABA triblock copolymers initially adopt a flat, pancake-like conformation at the interface. As adsorption increases, molecules contact, resulting in the displacement of the soluble A blocks from the interface into the adjacent solution. For some PEO-PPO-PEO molecules at air/water interfaces, this structural rearrangement manifests as a small plateau in surface pressure.[24] In between the region of first overlap and the CMC, polymer chains pack more tightly until the final adsorption layer resembles that of a hydrated PEO brush.[5] Adsorption halts at the CMC as individual chains form micelles instead of adsorbing to the interface.

The dilatational elasticity of water-soluble PEO-based, amphiphilic block copolymers is most sensitive to the PEO brush. Several studies at air/water

interfaces have shown elastic moduli up to 30 mN/m for diblocks and ABA triblocks.[6–10] These studies show broadly that dilatational elasticity increases with the size of the PEO block. Elasticity also depends on the adsorbed amount of block copolymer, and it is possible for an interface to have a low elasticity despite having an adsorbed block copolymer with a large PEO group.[10] Villar-Alvarez *et al.*[19] have investigated the dilatational response of BAB triblocks at the air/water interface. Using a series of PBO-PEO-PBO copolymers at a single concentration, they observed an increase in dilatational elasticity with surfactant molecular weight, up to 20 mN/m. Their measurements show a slight frequency dependence, demonstrating the need for additional study of the dilatational response of BAB triblocks at fluid interfaces.

It is difficult to study the effect of middle-block brush flexibility of water-soluble BAB triblocks without introducing additional complexity. For example, replacing PEO with a polyelectrolyte could allow for modulating stiffness by controlling pH but introduces Coulombic interactions affecting both adsorption dynamics and equilibrium interfacial properties.[25] This problem can be circumvented by studying oil-soluble molecules at oil/water interfaces. The lyophilic A block of an oil-soluble BAB triblock can be one of any number of nonionic chemical species like stiff polystyrene (PS) or flexible poly(dimethyl siloxane) (PDMS) or poly(isoprene) (PI). Contrasting with adsorption at air/water interfaces, an adsorbed molecule at an oil/water interface can form a brush layer in either fluid phase depending on block size and solvent quality.

At oil/water interfaces, long PEO blocks still form a brush region on the water side of the interface.[11,12] Penetration into the oil depends on the size of the hydrophobic block. Surfactants with larger hydrophobic blocks can penetrate further into the oil than those with smaller ones.[13] By comparing adsorption to crosslinked and linear PDMS, the degree of penetration of the hydrophobic block of water-soluble block copolymers into the oil has been observed to correlate with their surface activity.[14] The block copolymer that penetrates further into the oil adsorbs more strongly to the interface.

For ABA triblocks, the mechanical response of interfaces dominated by a hydrated PEO brush layer seems to be controlled by a combination of adsorbed amount and PEO block size, like at air/water interfaces. By using ellipsometry and interfacial tensiometry, Ramirez *et al.*[16] show that the limiting elasticity (the thermodynamic contribution to dilatation) depends on both the amount of material at the interface and its conformation. The measured elasticities are less than the limiting elasticity, which does not reveal any obvious mechanical extra stresses.[26]

This chapter goes beyond the existing literature by providing a systematic look at the interfacial properties of a series of oil-soluble, diblock and BAB triblock copolymers at the oil/water interface. These molecules are copolymers of PEO and PDMS, enabling investigation into the effect of a flexible, oily brush on the adsorption and mechanical properties of the interface. The PEO block is too short (several statistical segments at most) to form a brush layer in the water. Block ratios and molecular weights have been carefully chosen to design a model system, useful in exploring interfacial properties from the perspective of the oil.

2.2 MATERIALS AND METHODS

The block copolymer surfactants used in this chapter are copolymers of hydrophilic poly(ethylene oxide) (PEO) and hydrophobic poly(dimethyl-siloxane) (PDMS). Two diblock and two BAB triblock surfactants are used in this study. Molecular details are provided in Table 2.1. These molecules are not water soluble but are completely soluble at the concentrations used here in at least two alkanes (isooctane and n-dodecane) and two silicone oils (100 and 2000 cSt). Molecules will be identified in an abbreviated manner. For example, the diblock copolymer with 6 PEO units and 29 PDMS units is referred to as E_6D_{29}. The triblock copolymer with two 11-unit PEO blocks and a central 160-unit PDMS block is referred to as $E_{11}D_{160}E_{11}$.

Table 2.1. Block copolymer surfactants where N_E is the number of PEO monomers, N_D is the number of PDMS monomers, M_E is the mass of the PEO block, M_D is the mass of the PDMS block and M_n is the number-averaged molecular weight. M_E and M_D have been calculated by multiplying the number of repeat units by the molecular weight of that unit's monomer (44 g/mol for PEO and 74 g/mol for PDMS). M_n has been determined by NMR or GPC within ~10% agreement with estimated values.[27] Mass is given in units of g/mol. M_E/M_{KE} and M_D/M_{KD} denote the number of Kuhn monomers that compose each block. The size and mass of a Kuhn monomer of PEO are 11 Å and 137 g/mol, respectively; those of a Kuhn monomer of PDMS are 13 Å and 381 g/mol, respectively.[28]

	N_E	N_D	M_E (g/mol)	M_D (g/mol)	M_n (g/mol)	M_E/M_{KE}	M_D/M_{KD}
E_6D_{29}	6	29	260	2100	2400	1.9	5.6
$E_{11}D_{80}$	11	80	480	5900	6400	3.5	16
$E_6D_{80}E_6$	6(2)	80	260(2)	5900	6400	1.9(2)	16
$E_{11}D_{160}E_{11}$	11(2)	160	480(2)	12000	13000	3.5(2)	31

These molecules are synthesized via anionic polymerization without an additional chemical linker between the blocks and are characterized with Nuclear Magnetic Resonance spectroscopy (NMR) and Gel Permeation Chromatography (GPC).[27] Number average molecular weights (M_n) given in Table 2.1 have been rounded for clarity to within 10% of their measured values. Polydispersity is low with PEO blocks having a polydispersity index between 1.05 and 1.08 and PDMS blocks having a polydispersity index below 1.09. For example, $E_6D_{80}E_6$ has a PDMS block with between 73 and 83 chemical monomers, and $E_{11}D_{160}E_{11}$ has a PDMS block with between 157 and 164 monomers. Table 2.1 additionally provides information on the number of statistical monomers in each block, calculated relative to solvent conditions in pure melts.[28]

N-dodecane (99%), referred to as dodecane, was purchased from Sigma and passed through serological pipettes packed with basic alumina powder to remove surface-active impurities. Deionized water, referred to as water, with a resistivity of 18.2 MΩ·cm was produced using a Barnstead Ultrapure water filtration system. Solutions were prepared in acid-washed vials.

Interfacial properties of dodecane/water interfaces have been measured with a microtensiometer platform, described in detail in Section 1.2, in two extremes of interfacial curvature. Oil/water interfaces are defined to be concave for dodecane/surfactant within the capillary and convex for dodecane/surfactant within the reservoir. The equilibrium interfacial tension of dodecane/water is initially measured to be 52.5 mN/m and decreases by less than 1 mN/m in 1000 s without surfactant.

2.3 RESULTS

Figure 2.1 shows steady state interfacial pressure, Π, with solution concentration, C_b, of four block copolymer surfactants at convex (empty points) and concave (filled points) interfaces. An interface is said to be at steady state if the measured interfacial pressure changes by less than 1 mN/m over 1000 s. For each block copolymer, Π increases monotonically with C_b. The diblock $E_{11}D_{80}$ shows the sharpest increase in Π at the lowest concentration. Requiring the highest solution concentrations for adsorption, the triblock $E_{11}D_{160}E_{11}$ is the least surface active. The diblock E_6D_{29} and the triblock $E_6D_{80}E_6$ have identical interfacial activity. The data shown in Figure 2.1 agree qualitatively with those observed at the iso-octane/water interface.[29] No simple relationship is seen between surface activity and molecular properties like block ratio, size or architecture.

Steady-state measurements do not detect a CMC, often manifesting as a plateau of interfacial pressure at higher concentrations. For E_6D_{29}, $E_{11}D_{80}$ and $E_6D_{80}E_6$, raising solution concentrations above those shown in Figure 2.1 causes interfacial pressure to fall outside the measurable range of the microtensiometer (γ < 10 mN/m, Π > 42.5 mN/m). The absence of an observable CMC agrees with data from small-angle X-ray scattering (SAXS).[27,30] Higher concentration data for $E_{11}D_{160}E_{11}$ is currently unavailable due to a limit of material availability. Statistically significant differences between steady state values at both interfacial curvatures were not observed at any point, verifying that depletion to solid surfaces in the apparatus does not affect the measurements.[31] This is not unexpected given
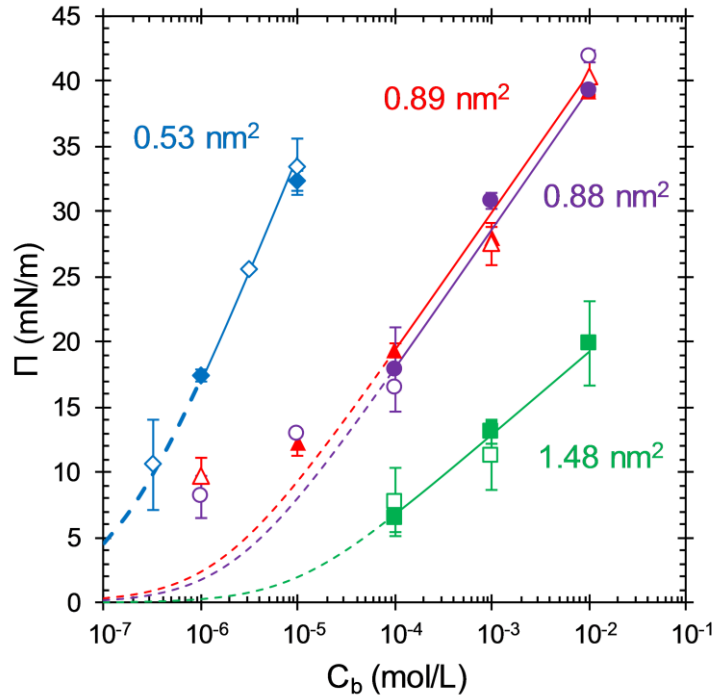
Figure 2.1. Steady state interfacial pressure with solution concentration for E_6D_{29} ($\bullet$,$\circ$), $E_{11}D_{80}$ ($\blacklozenge$,$\diamond$), $E_6D_{80}E_6$ ($\blacktriangle$,$\triangle$) and $E_{11}D_{160}E_{11}$ ($\blacksquare$,$\square$). Filled symbols are for adsorption to a concave interface; empty symbols are for adsorption to a convex interface. Lines correspond to regressions using the Gibbs adsorption equation (solid) and Langmuir isotherm (dashed).

that the radius of curvature of these interfaces ($R \sim 40$ μm) is much larger than the radius of gyration of the molecules ($R_g \sim 10$ nm).

Applying the Gibbs adsorption equation to high concentration data, the molar area of a saturated monolayer, Γ, can be calculated for each block copolymer, given by

$$\Gamma = \frac{1}{RT} \frac{d\Pi}{d \ln C_b} \tag{2.1}$$

where R is the gas constant, T is absolute temperature and Π is the steady-state surface pressure. The Gibbs adsorption isotherm is valid if these interfaces are at thermodynamic equilibrium with the adjacent solution, which is assumed to be

14

ideal. This is not strictly true for these interfaces since interfacial pressure is still slowly changing at the end of each experiment. The area occupied by a single adsorbed molecule within a saturated monolayer can be calculated using Eq 2.1 in the high-concentration limit. These areas are given in Figure 2.1.

Relating the steady-state interfacial pressure with surface excess concentration at lower concentrations requires the adoption of an adsorption isotherm. The Langmuir isotherm, Eq 2.2, is one of the simpler adsorption models available, often used to describe the adsorption of nonionic surfactants at fluid/fluid interfaces:[32]

$$\frac{\Gamma}{\Gamma_\infty} = \frac{C_b}{a + C_b}.$$

(2.2)

This isotherm has only two adjustable parameters: the surface excess concentration of a saturated monolayer, Γ_∞, and the turnover concentration, a (the bulk concentration necessary to form a half monolayer). Substitution of Eq 2.2 into Eq 2.1 and subsequent integration yields the Frumkin equation of state, Eq 2.3, as

$$\Pi = -RT\Gamma_\infty \ln\left(1 - \frac{\Gamma}{\Gamma_\infty}\right).$$

(2.3)

Substituting Eq 2.2 into Eq 2.3 results in the Szyszkowski equation, relating surface pressure and bulk concentration. The Szyszkowski equation has been regressed using linear least squares in MATLAB® to determine values of a and Γ_∞, which are given in Table 2.2.

As expected, the Langmuir isotherm recovers the values of Γ_∞ calculated using Eq 2.1. The standard errors provided by sequential linear regressions reveal uncertainty in the fit values of a and Γ_∞ of approximately 10%. Values of a are

likely to be less certain due to the sparsity of experimental data near the turnover concentration. The fits shown in Figure 2.1 reflect this uncertainty. At high concentrations where the fits describe the data well, solid lines show the region over which Eq 2.1 has been used to calculate Γ_∞. The dashed lines show the regions over which the value of the turnover concentration greatly affects the model fit. $E_6D_{80}E_6$ and E_6D_{29} have the most data below the linear region and show poor agreement with the Langmuir fits at those concentrations. Triblock copolymers have been observed to possess a pseudo-plateau at intermediate values of interfacial pressure that corresponds with the transition from pancake-like to mushroom-like adsorbed conformations.[4] The shape of the E_6D_{29} data indicate that this molecule may also experience a conformational transition at the interface.

Comparison of calculated values of Γ_∞ provides insight into the adsorbed state of the block copolymers. Block copolymers with the same architecture can be compared by molecular weight. The triblocks $E_6D_{80}E_6$ and $E_{11}D_{160}E_{11}$ occupy different interfacial areas at saturation (0.89 nm^2 vs 1.48 nm^2), and the area occupied by a single molecule is greater for the larger molecule, $E_{11}D_{160}E_{11}$. An increase in the area per molecule with molecular weight suggests some spreading

Table 2.2. Langmuir isotherm parameters fit to steady-state adsorption data from Figure 2. Self-diffusion coefficients are given for linear PDMS melts at 20 °C.[40]

	a (μmol/L)	Γ_∞ (μmol/m^2)	Area (nm^2)	D (m^2/s)
E_6D_{29}	2.2	1.9	0.88	$6\cdot10^{-11}$
$E_{11}D_{80}$	0.13	3.2	0.53	$2\cdot10^{-11}$
$E_6D_{80}E_6$	1.5	1.9	0.89	$2\cdot10^{-11}$
$E_{11}D_{160}E_{11}$	9.8	1.1	1.48	$9\cdot10^{-12}$

16

out of the molecule along the interface with adsorption. The diblocks E_6D_{29} and $E_{11}D_{80}$ show the opposite trend (0.88 nm^2 vs 0.53 nm^2), a decrease in area with increasing molecular weight. However, total molecular weight is the wrong basis for comparison. According to SF theory, the surface activity of a diblock increases linearly with the size of the sticky block (EO for these molecules). [22] $E_{11}D_{80}$ with 11 EO units adsorbs to a greater extent ($\Gamma_\infty = 3.2$ μmol/m^2) than the smaller diblock E_6D_{29}, having only 6 EO units ($\Gamma_\infty = 1.9$ μmol/m^2). In fact, the ratio of surface excess concentrations, $\Gamma_\infty(E_{11}D_{80}) \big/ \Gamma_\infty(E_6D_{29}) = 1.7$, is almost identical to the ratio

of the EO units, $N_{EO}(E_{11}D_{80}) \big/ N_{EO}(E_6D_{29}) = 1.8$. For the diblocks, surface activity seems to be controlled by the sticky EO block, and the PDMS is merely along for the ride.

Comparisons can also be made between molecules of different block architectures by molecular weight. The molecules $E_6D_{80}E_6$ and $E_{11}D_{80}$ have almost identical molecular weights and EO content. The triblock $E_6D_{80}E_6$ occupies more space (0.89 nm^2) at the interface than the diblock of similar mass, $E_{11}D_{80}$ (0.53 nm^2). This shows that the triblock adopts a flatter conformation at the interface than the diblock. In other words, the hydrophobic block of $E_{11}D_{80}$ extends further into the dodecane. This is consistent with total adsorption of both amphiphilic anchors of the triblock, resulting in a flatter conformation and thinner PDMS brush region.

The final comparison is between a triblock and the diblock that would arise from cutting the triblock into two equal parts. Figure 2.1 contains two of these

comparisons: between $E_{11}D_{80}$ and $E_{11}D_{160}E_{11}$ and between E_6D_{29} and $E_6D_{80}E_6$, although the latter is not an exact comparison. The adsorbed area per molecule more than doubles from $E_{11}D_{80}$ (0.53 nm^2) to $E_{11}D_{160}E_{11}$ (1.48 nm^2), exemplifying the conventional understanding that an adsorbing triblock pays a greater entropic penalty than the diblock.[22] E_6D_{29} (0.88 nm^2) and $E_6D_{80}E_6$ (0.89 nm^2) do not follow the same trend. Given the data for $E_6D_{80}E_6$, we would expect a single molecule of E_6D_{29} to occupy a patch of interface smaller than 0.45 nm^2. The interpretation applied to the larger diblock and triblock does not hold for the smaller molecules. For E_6D_{29} and $E_6D_{80}E_6$, doubling the number of sticky EO blocks results in an approximate doubling of the amount of PDMS transported to the interface. It would be of great interest to determine the block ratios at which the transition occurs between EO-dominated adsorption and PDMS-dominated adsorption.

The steady-state values presented in Figure 2.1 are in the long-time limit of transient behavior that is captured in the measurements. Adsorption dynamics provide insight into the adsorption mechanism, especially when viewing short-time dynamics that experience the most drastic change in interfacial pressure. Figure 2.2 shows dynamic interfacial pressure curves for the first 1000 s of adsorption for both convex (empty points) and concave (filled points) interfaces.

All interfaces are initially devoid of block copolymer molecules and approach a value of steady-state interfacial pressure that does not depend on the curvature of the interface. Initial adsorption from $\Pi = 0$ occurs beyond the resolution for all but the convex interfaces with $E_{11}D_{80}$ (◇) and E_6D_{29} (○). For 10^{-4} M E_6D_{29}, 10^{-3} M $E_6D_{80}E_6$ and 10^{-3} M $E_{11}D_{160}E_{11}$, the adsorption dynamics are also
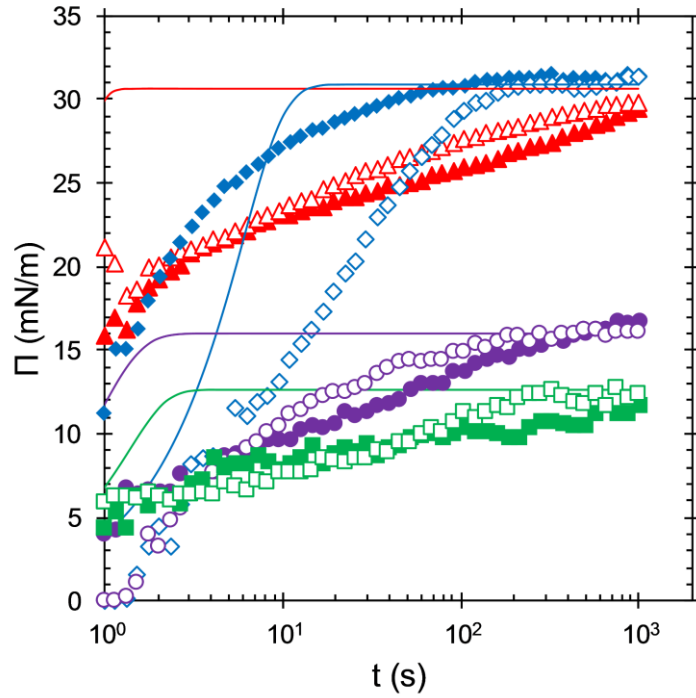
Figure 2.2. Dynamic interfacial pressure to concave (filled) and convex (empty) interfaces. Solution concentrations are 10^{-5} M for $E_{11}D_{80}$ ($\blacklozenge$,$\lozenge$), 10^{-4} M for E_6D_{29} ($\bullet$,$\circ$), 10^{-3} M for $E_6D_{80}E_6$ ($\blacktriangle$,$\triangle$) and 10^{-3} M for $E_{11}D_{160}E_{11}$ ($\blacksquare$,$\square$). Solid lines have been calculated for kinetically limited adsorption with the Langmuir isotherm.

independent of interfacial curvature. For 10^{-5} M $E_{11}D_{80}$ at this concentration, adsorption is faster to a concave interface. The solid lines are predictions for adsorption dynamics assuming Langmuirian kinetics and will be discussed later.

These concentrations have been selected because they exemplify a shared feature of the adsorption dynamics of these four block copolymers. At lower concentrations, interfacial curvature has no effect on the rate of adsorption, demonstrating that the adsorption is limited by kinetics at the interface rather than by diffusion from the bulk.[33] At the highest concentrations studied, adsorption is more rapid to a concave interface than to a convex one. This is contrary to that expected for adsorption in the diffusive limit, which favors diffusion to a comvex

interface. We would expect to see faster adsorption to a concave interface only if the adsorption caused a reduction in the bulk concentration of surfactant, a phenomenon known as depletion. Depletion results in a lower-than-expected equilibrium interfacial pressure and occurs most frequently for dilute surfactant solutions in confined volumes.[31] This behavior is puzzling and currently without explanation.

Dilatational rheology is the study of the complex stress response of an interface during compression. It serves both as an indirect structural measurement and as a probe of processes of material exchange or reorientation.[34–36] To that end, the dilatational rheological response of each steady-state interface has been characterized. Figure 2.3 shows a common way of representing the complex dilatational modulus, E: real, E', (connected by a dashed line) and imaginary, E'', (components of the dilatational modulus with oscillation frequency, ω, for convex (empty points) and concave (filled points) interfaces. For comparison, data are shown for each molecule at similar values of interfacial pressure, $\Pi = 15 \pm 1.5$ mN/m. A feature shared for every molecule studied is that both E' and E'' do not depend on interfacial curvature.

The elastic modulus of these four molecules does not show a strong frequency dependence, and all molecules except $E_{11}D_{80}$ have a low elastic modulus ($E' \leq 10$ mN/m) at this interfacial pressure. $E_{11}D_{80}$ has the highest elastic modulus ($E' \approx 30$ mN/m). All molecules show a frequency-dependent viscous modulus, with E'' of E_6D_{29} having the strongest frequency dependence. Since the moduli can depend on both oscillation frequency and surface concentration, comparison of the
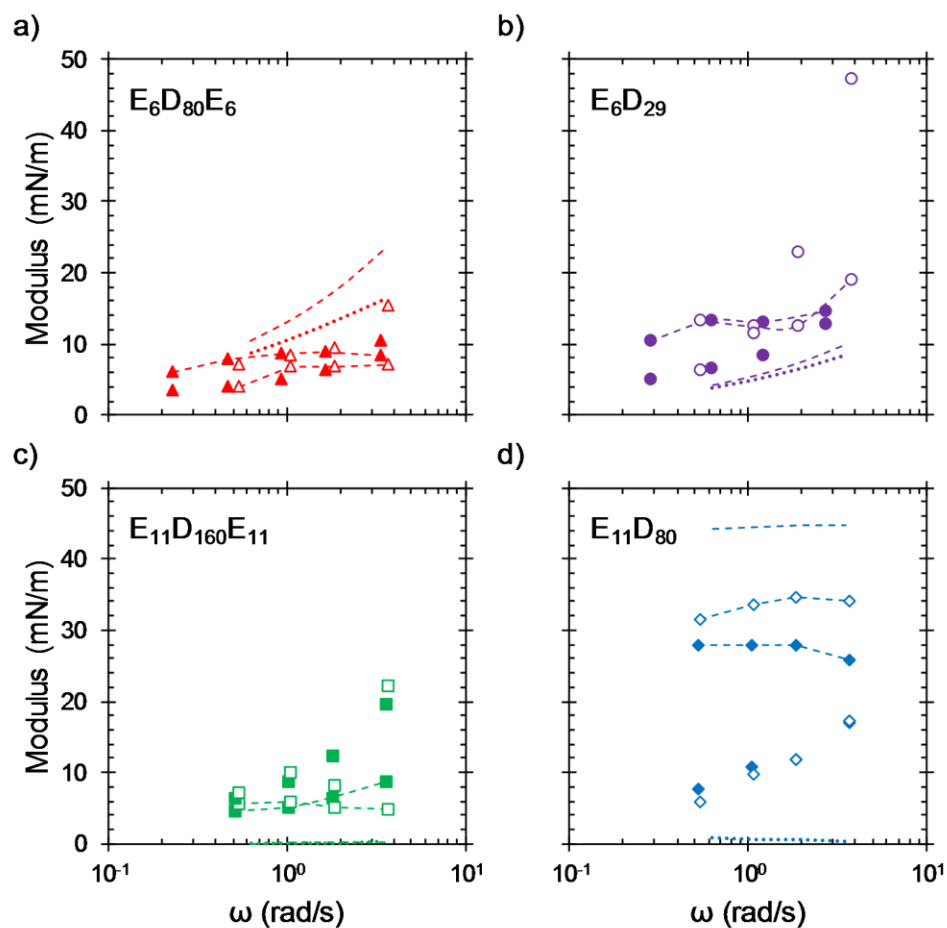
Figure 2.3. Frequency dependence of real (points connected by dashed lines) and imaginary (points only) components of the complex dilatational modulus for convex (empty) and convex (filled) interfaces at an interfacial pressure of 15 ± 1.5 mN/m. Dashed and dotted lines without points are predictions for the real and imaginary components, respectively, from the LVDT model.

dilatational response of the four block copolymers could involve the construction of many figures like Figure 2.3 at various interfacial pressures, but this would prove cumbersome. Instead, the complex modulus has been expressed as a function of interfacial pressure at a single frequency.

Figure 2.4 shows the variation of the magnitude of the complex dilatational modulus, $|E^*|$, at 0.5 rad/s with interfacial pressure for each block copolymer. $|E^*|$
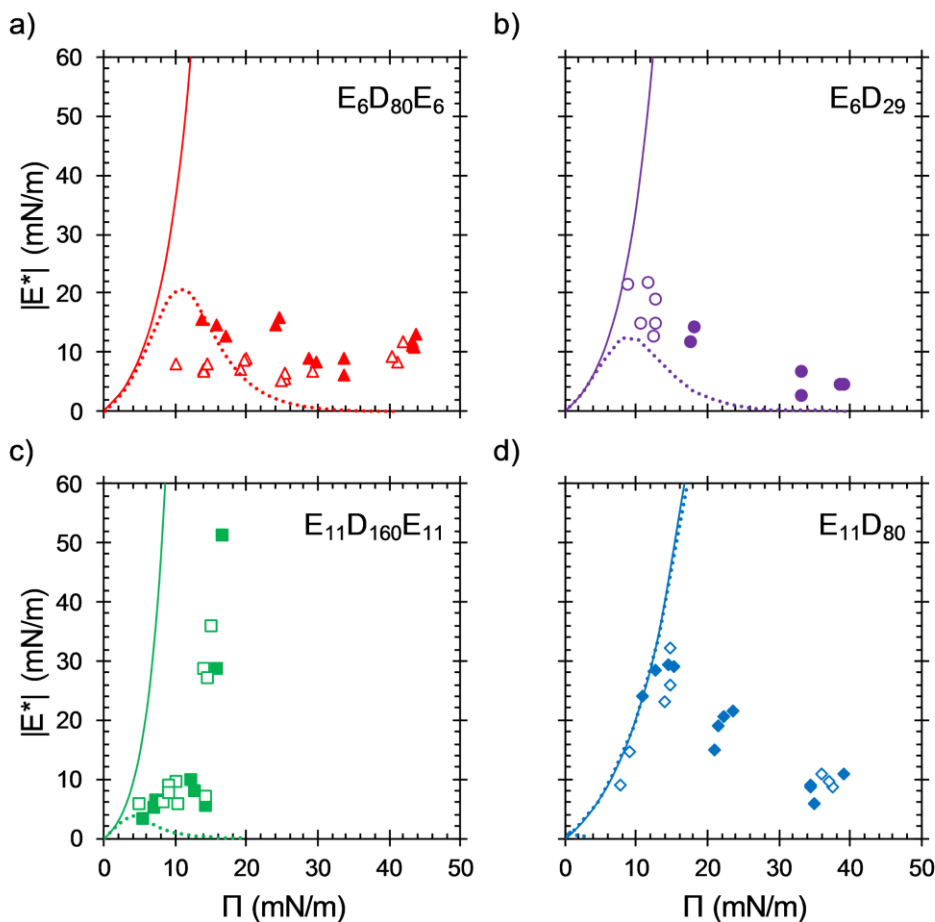
Figure 2.4. Magnitude of complex dilatational modulus at a frequency of 0.5 rad/s with interfacial pressure for convex (empty points) and convex (filled points) interfaces. Solid lines are predictions of ε_0 calculated by fitting the Langmuir adsorption isotherm to data in Figure 2.1. Dotted lines are predictions from the LVDT model.

is not observed to depend on the curvature of the interface, except possibly for $E_6D_{80}E_6$ at low interfacial pressures. For $E_6D_{80}E_6$, $|E^*|$ is low (< 20 mN/m) and varies little with interfacial pressure. The other triblock, $E_{11}D_{160}E_{11}$, shares a similar behavior at the lowest surface pressures, but modulus rapidly increases near an interfacial pressure of 16 mN/m. The diblocks show contrasting behavior to the triblocks in that $|E^*|$ of the diblocks is highest at low surface pressures and

decreases with increasing surface pressure. The lowest data points for $E_{11}D_{80}$ reveal

a nonmonotonic dependence of complex modulus on surface pressure.

The solid lines show calculated values of limiting elasticity, ε_0, sometimes

referred to as the Gibbs modulus,

$$\varepsilon_0 \equiv \frac{d\Pi}{d\ln\Gamma} \ .$$

(2.4)

The limiting elasticity is the thermodynamic contribution to the measured elasticity

and has been calculated by differentiating Eq 2.3 with respect to surface excess

concentration:[37,38]

$$\varepsilon_0 = \frac{RT\Gamma}{1 - \Gamma/\Gamma_\infty}.$$

(2.5)

Elasticities greater than the limiting elasticity indicate the presence of mechanical

extra stresses, which we do not observe here.[39] Rather, the measured magnitudes

of the complex modulus are less than the thermodynamic limit. This indicates that

dilatational stresses (of thermodynamic origin or otherwise) are being relaxed by

some process.

For small surfactants, relaxation of dilatational stresses often occurs by the

exchange of molecules between the interface and the neighboring solution.[37]

Expansion of the interface entices adsorption of additional material from the bulk,

and interfacial compression drives desorption. For material exchange to occur an

adsorbed molecule must be adsorbed reversibly, and the exchange with the bulk

must occur at least as quickly as the oscillation. Surfactants with this property are

said to be soluble from the perspective of the interface. However, an adsorbed

molecule need not be completely reversibly adsorbed (desorption to zero interfacial
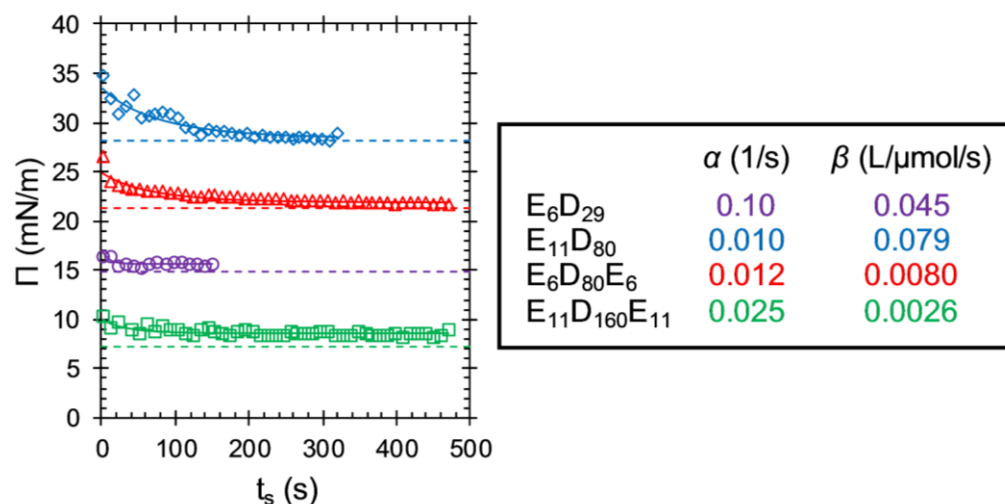
Figure 2.5. Dynamic interfacial pressure of steady-state, convex interfaces following a three-fold dilution of the block copolymer solution. The dashed lines correspond to the values of interfacial pressure expected for completely reversible adsorption, calculated using the fits provided in Table 2.2. Solid lines are single exponential fits. C_b are 10^{-5} M for $E_{11}D_{80}$, 10^{-4} M for E_6D_{29}, 10^{-3} M for $E_6D_{80}E_6$ and 10^{-3} M for $E_{11}D_{160}E_{11}$.

pressure upon infinite dilution), rather only within the magnitude of compression and expansion applied during the oscillation. To test the local adsorption reversibility, these interfaces can be processed with solvent, as shown in Figure 2.5.

Figure 2.5 shows the desorption of block copolymer molecules from steady-state, convex interfaces following a three-fold dilution of the block polymer solution. Dilution occurs at the zero value of shifted time, t_s, and has been performed by pipetting 2 mL of dodecane without surfactant into the reservoir that initially contains 1 mL of surfactant solution. Interfacial pressure decreases immediately upon dilution for all interfaces. The greatest desorption occurs from the largest interfacial pressure, which is to be expected from the slopes of steady-state adsorption in Figure 2.1. The dashed lines show the expected steady-state values after desorption, calculated using the Langmuir fits shown in Figure 2.1.

$E_6D_{80}E_6$, $E_{11}D_{80}$ and E_6D_{29} desorb to within 1 mN/m of the calculated values. $E_{11}D_{160}E_{11}$ desorbs by approximately 3 mN/m but remains more than 1 mN/m above the expected value following desorption. Steady-state adsorption data for $E_{11}D_{160}E_{11}$ are the least reproducible in this study, so a lack of quantitative agreement with the prediction is not surprising. The solid lines are calculated by fitting desorption dynamics to a single exponential, quantifying the rate of desorption with a constant, α, given in Figure 2.5.

2.4 DISCUSSION

From solvent processing, it is apparent that these block copolymers possess local adsorption reversibility, showing that the relaxation of dilatational stresses observed in Figure 2.4 may be due to material exchange between the interface and the bulk. The most common method for interpreting the dilatational rheology of soluble surfactants is with a diffusional model proposed by Lucassen and van den Tempel (LVDT).[37] The LVDT model supposes that the dilatational measurement is the result of two factors: a thermodynamic elasticity originating from the surfactant's equation of state (the limiting elasticity) and a dissipative relaxation from diffusion-limited exchange driven by the change in interfacial area, as

$$E = \varepsilon_0 \frac{1 + \zeta + i\zeta}{1 + 2\zeta + 2\zeta^2} \tag{2.6}$$

$$\zeta \equiv \frac{dC_b}{d\Gamma} \sqrt{\frac{D}{2\omega}}. \tag{2.7}$$

The relaxation is expressed in the model using a diffusion parameter, ζ, that is the ratio between the timescales of desorption and oscillation of interfacial area. Since the adsorption isotherms for each surfactant have been determined by regressing

steady state data in Figure 2.1, $\dfrac{dC_b}{d\Gamma}$ can be calculated by differentiation of Eq 2.2

following rearrangement:[38]

$$\frac{dC_b}{d\Gamma} = \frac{a}{\Gamma_\infty \left(1 - \Gamma/\Gamma_\infty\right)^2}.$$
(2.8)

As an example, Figure 2.6 shows the LVDT relaxations predicted for

$E_6D_{80}E_6$ for the concentration range studied using self-diffusion coefficients taken

from PDMS polymer melts (given in Table 2.2).[40] The magnitude of the

dilatational modulus predicted by the LVDT model (dotted lines) is identical to the

limiting elasticity at low concentrations and experiences a maximum when the

timescale of diffusion is equivalent to that of the experiment. This is often

represented as a critical frequency for a specific interface that is calculated by

substituting $\zeta = 1$ into Eq 2.7. At higher concentrations, the diffusional relaxation

dominates the interfacial response, decreasing the measured modulus to the lower

limit of resolution on the measurement.

D and ω have opposite and identical effects on the value of ζ, although in

practice it is much easier to probe the stress relaxation by changing the oscillation

frequency instead of the diffusivity. The relaxations at the oscillation frequencies

shown in Figure 2.6 are in the "shoulder" region of the LVDT relaxation. By

varying C_b or ω, the three distinct regions of the diffusional relaxation can be

observed, dominated by thermodynamics at low C_b or high ω, by transport at high

C_b or low ω and by a combination of the two at intermediate C_b and ω.

The diffusion-limited relaxation at 0.5 rad/s calculated with the LVDT

model is given by the dotted lines in Figures 2.3 and 2.4. The diffusional model
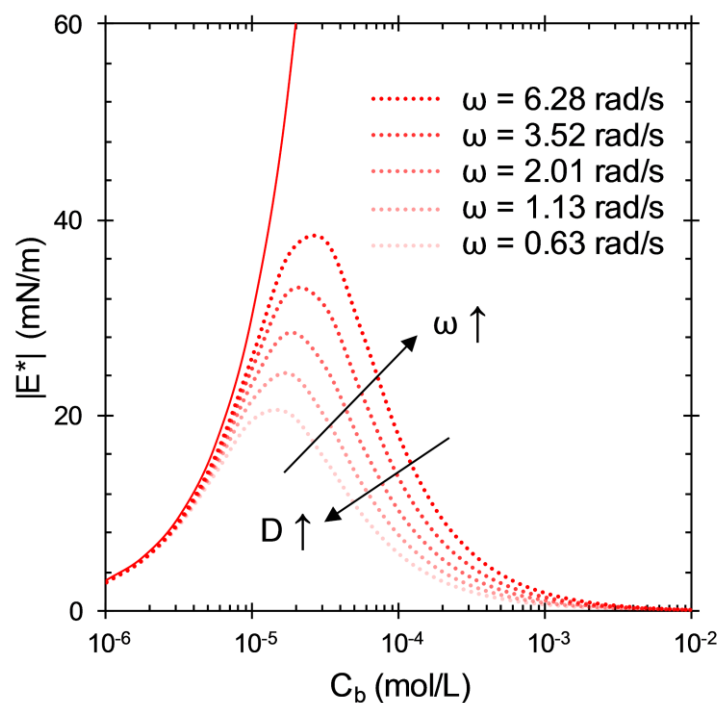
Figure 2.6. Dependence of LVDT relaxations on solution concentration and oscillation frequency for $E_6D_{80}E_6$. The solid line shows the variation of limiting elasticity with solution concentration. The dotted lines show the LVDT relaxations for frequencies specified by the legend.

does not predict the relaxation of dilatational stresses for $E_{11}D_{80}$. The model does a poor job in predicting the stress relaxation of the surfactants studied here, albeit qualitatively predicting the behavior of E_6D_{29}. E_6D_{29} is the smallest surfactant studied here with a number-averaged molecular weight of 2400 g/mol. It is most similar in size and structure to typical small-molecule surfactants (often one-tailed, ~ 1000 g/mol), so it is the most likely candidate for diffusional exchange.

The rate of diffusion to a curved interface strongly depends on the curvature of that interface,[41,42] but the LVDT relaxations have been calculated for a planar interface. Since diffusion is enhanced to a convex interface and suppressed to a concave interface, dilatational stresses would be relaxed to a greater extent at a convex interface than at a concave interface.[43] Correcting for the curvature of the

interface does not improve the ability of the diffusional model to describe the data in Figures 2.3 and 2.4, which is not surprising given that the measured E does not vary with interfacial curvature. This is consistent with known limitations of diffusional models to describe transient adsorption of block copolymers and other macromolecules to fluid interfaces.[44]

At all but the largest interfacial pressures, adsorption dynamics do not depend on the curvature of the interface (shown in Figure 2.2), demonstrating that diffusion to the interface is not the rate-limiting step during adsorption, corroborating the finding that diffusion-limited exchange is not responsible for relaxing dilatational stresses. For a small-molecule surfactant, curvature-insensitive dynamics would indicate that the adsorption is limited by adsorption kinetics from the fluid near the interface onto the interface, itself. However, the block copolymers here have shown that they do not behave as small-molecule surfactants. For polymers at solid surfaces, adsorption is often limited by slower processes such as penetration of the adsorbed layer or chain rearrangement.[45] For simplicity, these block copolymer surfactants have been modeled neglecting those slower processes. This assumption will be evaluated in a moment.

Assuming Langmuirian adsorption kinetics, the rate of change of adsorbed surfactant is described by an ordinary differential equation with the following form:

$$\frac{d\Gamma}{dt} = \beta C_b (\Gamma_\infty - \Gamma) - \alpha \Gamma \quad . \tag{2.9}$$

The quotient of the rate constants for desorption, α, and adsorption, β, is equivalent to the turnover concentration, $a = \alpha/\beta$. For material desorbing from interfaces

initially with an equilibrated layer of adsorbed surfactant, the rate of desorption will dominate Eq 2.9, and the desorption dynamics take the form of an exponential decay. The solid lines in Figure 2.5 show the results of single-exponential fits that agree well with the desorption dynamics. The fits provide α and have been calculated by regressing dynamic surface excess concentration during desorption, determined using Eq 2.3. Values of β have been calculated by combining these results with the values of a given in Table 2.2. Both α and β for each surfactant are given in Figure 2.5.

By comparing the rate constant for adsorption, β, the triblocks should adsorb between five and thirty times more slowly than the diblocks. This seems reasonable given that the enthalpic favorability of delivering a triblock's second amphiphilic anchor into the plane of the interface struggles against the entropy that drives chain extension into the dodecane. When comparing desorption constants, α, the breakpoint is by molecular weight rather than block architecture. The three larger polymers desorb between four and ten times more slowly than the smallest molecule, E_6D_{29}. It is useful to consider the thickness of the brush region. Adsorbed areas in Figure 2.1 reveal E_6D_{29} to occupy an outsized amount of interfacial area relative to the three larger molecules. This necessitates a much thinner brush region (on the oil side), resulting in less steric hindrance during desorption.

Despite reasonable values of β, Langmuirian kinetics poorly predict the adsorption dynamics shown in Figure 2.2. The predictions (solid lines) vastly overpredict the rate of adsorption and do not even capture the shape of the

measurements. E_6D_{29}, $E_6D_{80}E_6$ and $E_{11}D_{160}E_{11}$ possess a slower mode of adsorption that cannot be captured by Langmuirian kinetics even when regressing adsorption dynamics directly. This slow adsorption is likely a result of molecular rearrangements at or near the interface due to the macromolecular nature of these surfactants. These rearrangements are not influenced by the curvature of the interface because of the large size difference between a polymer chain and the radius of curvature of the interface.

While adsorption dynamics are clearly influenced by the macromolecular nature of these surfactants, solvent processing shows that they share a feature with many small-molecule surfactants, adsorption reversibility. Without a direct measure of adsorption reversibility, the interpretation of dilatational properties would have to assume that either these molecules behave as small surfactants capable of desorbing or as macromolecules whose dilatational relaxations are due to reorientation at the interface. Interfacial processing provides a richer picture wherein the structure-property relationships of these adsorbed surfactants arise from both the molecular and macromolecular.

2.5 SUMMARY

Oil-soluble diblock and BAB triblock copolymers of PEO and PDMS have been characterized at the dodecane/water interface. Steady-state interfacial pressure is independent of interfacial curvature and varies with block structure and molecular weight. Interfacial areas occupied by a single, adsorbed surfactant molecule as calculated by the Gibbs adsorption equation are mostly consistent with SF theory. Adsorption dynamics are insensitive to interfacial curvature to all but

the largest interfacial pressures studied, demonstrating that diffusion to the interface is not the rate-limiting step during adsorption. Diblock and triblock surfactants show two qualitatively distinct, dilatational rheological responses with no obvious extra stresses ($|E^*| < \varepsilon_0$). The dilatational response is not sensitive to interfacial curvature. All four block copolymers studied here possess local adsorption reversibility; however, desorption occurs too slowly for kinetically limited transport to be the mechanism responsible for relaxing dilatational stresses. The relaxations are likely of macromolecular origin, driven by chain reorientation at the interface.

(1)   Alexandridis, P. *Curr. Opin. Colloid Interface Sci.* **1996**, *1* (4), 490–501.

(2)   Alexandridis, P. *Curr. Opin. Colloid Interface Sci.* **1997**, *2* (5), 478–489.

(3)   Bodratti, A. M.; Sarkar, B.; Alexandridis, P. *Adv. Colloid Interface Sci.* **2017**, *244*, 132–163.

(4)   Alexandridis, P.; Athanassiou, V.; Fukuda, S.; Hatton, T. A. *Langmuir* **1994**, *10* (8), 2604–2612.

(5)   Muñoz, M. G.; Monroy, F.; Ortega, F.; Rubio, R. G.; Langevin, D. *Langmuir* **2000**, *16* (3), 1094–1101.

(6)   Rippner Blomqvist, B.; Wärnheim, T.; Claesson, P. M. *Langmuir* **2005**, *21* (14), 6373–6384.

(7)   Ertekin, A.; Kim, Y.; Kausch, C. M.; Thomas, R. R. *J. Colloid Interface Sci.* **2009**, *336* (1), 40–45.

(8)   Akentiev, A. V.; Miller, R.; Noskov, B. A. *Colloid J. Russ. Acad. Sci. Kolloidn. Zhurnal* **2002**, *64* (6), 653–660.

(9)   Noskov, B. A.; Lin, S.; Loglio, G.; Rubio, R. G.; Miller, R. *Langmuir* **2006**, No. 12, 2647–2652.

(10)   Hansen, F. K. *Langmuir* **2008**, *24* (1), 189–197.

(11)   Washington, C.; King, S. M.; Heenan, R. K. *J. Phys. Chem.* **1996**, *100* (18), 7603–7609.

(12)   Washington, C.; King, S. M.; Attwood, D.; Booth, C.; Mai, S. M.; Yang, Y. W.; Cosgrove, T. *Macromolecules* **2000**, *33* (4), 1289–1297.

(13)   Ramírez, P.; Muñoz, J.; Fainerman, V. B.; Aksenenko, E. V.; Mucic, N.; Miller, R. *Colloids Surfaces A Physicochem. Eng. Asp.* **2011**, *391* (1–3), 119–124.

(14)   Barnes, T. J.; Prestidge, C. A. *Langmuir* **2000**, *16* (9), 4116–4121.

(15)   Georgieva, D.; Schmitt, V.; Leal-Calderon, F.; Langevin, D. *Langmuir* **2009**, *25* (10), 5565–5573.

(16)   Ramírez, P.; Stocco, A.; Muñoz, J.; Miller, R. *J. Colloid Interface Sci.* **2012**, *378* (1), 135–143.

(17)   Naskar, B.; Ghosh, S.; Moulik, S. P. *Langmuir* **2012**, *28* (18), 7134–7146.

(18)   Pérez-Mosqueda, L. M.; Maldonado-Valderrama, J.; Ramírez, P.; Cabrerizo-Vílchez, M. A.; Muñoz, J. *Colloids Surfaces B Biointerfaces* **2013**, *111*, 171–178.

(19)   Villar-Alvarez, E.; Cambón, A.; Blanco, M.; Pardo, A.; Martínez, R.; Barbosa, S.; Váldez, M. A.; Juárez, J.; Taboada, P. *J. Phys. Chem. C* **2017**, *121* (23), 12684–12695.

(20)   Scheutjens, J. M. H. M.; Fleer, G. J. *J. Phys. Chem.* **1979**, *83* (12), 1619–1635.

(21)   Scheutjens, J. M. H. M.; Fleer, G. J. *J. Phys. Chem.* **1980**, *84* (2), 178–190.

(22)   Evers, O.; Scheutjens, J.; Fleer, G. *J. Chem. Soc. Farad. Trans.* **1990**, *86* (9), 1333–1340.

(23)   Ameri, M.; Attwood, D.; Collett, J. H.; Booth, C. *J. Chem. Soc. - Faraday Trans.* **1997**, *93* (15), 2545–2551.

(24)   Alexandridis, P.; Athanassiou, V.; Fukuda, S.; Hatton, T. A. *Langmuir* **1994**, *10* (8), 2604–2612.

(25)   Chang, C. H.; Franses, E. I. *Colloids Surfaces A Physicochem. Eng. Asp.* **1995**, *100* (C), 1–45.

(26)   Edwards, D. A.; Brenner, H.; Wasan, D. T. *Interfacial Transport Processes and Rheology*; Butterworth-Heinemann: Stoneheam, 1991.

(27)   Laufer, L. Amphiphilic block copolymers at the oil/water interface, Ben-Gurion University of the Negev, 2013.

(28)   Rubinstein, M.; Colby, R. *Polymer Physics*, 1st ed.; Oxford University Press, 2003.

(29)   Armon, M. Dynamics and Rheological Behavior of Amphiphilic Block Copolymers at the Oil / Water Interface, Ben-Gurion University of the Negev, 2015.

(30)   Precker, I. Block copolymers as surface-active agents at the oil-water interface, Ben-Gurion University of the Negev, 2011.

(31)   Alvarez, N. J.; Walker, M.; Anna, S. L. *Soft Matter* **2012**, *8*, 8917–8925.

(32)   Eastoe, J.; Dalton, J. . *Adv. Colloid Interface Sci.* **2000**, *85* (2–3), 103–144.

(33) Alvarez, N. J.; Vogus, D. R.; Walker, L. M.; Anna, S. L. *J. Colloid Interface Sci.* **2012**, *372* (1), 183–191.

(34) Noskov, B. A.; Loglio, G.; Miller, R. *Adv. Colloid Interface Sci.* **2011**, *168* (1–2), 179–197.

(35) Verwijlen, T.; Imperiali, L.; Vermant, J. *Adv. Colloid Interface Sci.* **2014**, *206*, 428–436.

(36) Davidson, M. L.; Walker, L. M. *Langmuir* **2018**, *34* (43), 12906–12913.

(37) Lucassen, J.; Van Den Tempel, M. *Chem. Eng. Sci.* **1972**, *27* (6), 1283–1291.

(38) Lucassen-Reynders, E. H.; Cagna, A.; Lucassen, J. *Colloids Surfaces A Physicochem. Eng. Asp.* **2001**, *186* (1–2), 63–72.

(39) Kotula, A. P.; Anna, S. L. *J. Rheol. (N. Y. N. Y).* **2015**, *59* (1), 85–117.

(40) Cosgrove, T.; Griffiths, P. C.; Hollingshurst, J.; Richards, R. D. C.; Semiyen, J. A. *Macromolecules* **1992**, *25* (25), 6761–6764.

(41) Ward, A. F. H.; Tordai, L. *J. Chem. Phys.* **1946**, *14* (7), 453–461.

(42) Alvarez, N. J.; Walker, L. M.; Anna, S. L. *Phys. Rev. E - Stat. Nonlinear, Soft Matter Phys.* **2010**, *82* (1), 1–8.

(43) Joos, P. *Dynamic Surface Phenomenon*; Fainerman, V., Loglio, G., Lucassen-Reynders, E. H., Petrov, P., Miller, R., Eds.; VSP BP: The Netherlands, 1999.

(44) Noskov, B. A. *Curr. Opin. Colloid Interface Sci.* **2010**, *15* (4), 229–236.

(45) Frantz, P.; Granick, S. *Phys. Rev. E - Stat. Nonlinear, Soft Matter Phys.* **1991**, *66* (7), 5–8.

CHAPTER 3

INTERFACIAL PROPERTIES OF POLYELECTROLYTE-SURFACTANT AGGREGATES AT THE AIR/WATER INTERFACE

3.1 INTRODUCTION

Interactions between macromolecules and surfactants have been studied for over a century, beginning with proteins and lipids[1,2] and rapidly growing to include the study of synthetic polymers and surfactants.[3–5] Commercial formulations containing mixtures of polymer and surfactant are commonplace in a variety of industries (personal care, cosmetics, coatings, and drug delivery to name a few), so there is much interest in relating solution behavior to dynamic interfacial properties of both solid/fluid and fluid/fluid interfaces. For systems prepared as dilute solutions, polymer/surfactant interactions are often reported as a binding isotherm. These isotherms demonstrate that the amount of polymer-bound surfactant varies with bulk surfactant concentration for a fixed number density of polymer molecules.[6–8] Since complexation alters the effective amphiphilicity of the aggregate, measuring interfacial tension (IFT) of an adjacent interface fluid/fluid interface has been useful for probing polymer/surfactant interactions.[9,10] This is especially true for weakly interacting systems (ionic surfactant, nonionic polymer), where features of the binding isotherm may appear directly in the equilibrium IFT curve.[11,12] Interpreting IFT data of strongly interacting systems (oppositely charged polyelectrolyte and surfactant) is less straightforward, complicated by the formation of insoluble or nonadsorbing structures.[13,14] A complete picture of interfacial activity requires IFT measurements to be supplemented with a technique

that measures structure or composition such as neutron reflectometry[13–15] or ellipsometry[16,17] and mechanical measurements with interfacial rheometry.[18–21]

The system of interest in this chapter is a semi-rigid, colloidal aggregate that has been polymerized from cetyltrimethylammonium 4-vinylbenzoate (CTVB) micelles. The aggregate, poly(cetyltrimethylammonium bromide) (pCTVB), has been characterized extensively in aqueous solution[22–28] and at water/silica and water/mica interfaces,[29–32] and the salient features will be discussed here. pCTVB is synthesized by polymerization of bound vinyl benzoate (VB⁻) counterions on cylindrical micelles.[22] The formation of a poly(vinyl benzoate) (pVB⁻) backbone entrained within the micelle results in the surfactant cetyltrimethylammonium (CTA⁺) assuming the role of counterion to the polyelectrolyte. This differs from the usual method of aggregate preparation of mixing two solutions, one of polyelectrolyte and one of charged surfactant (and their respective counterions), in that solutions of pCTVB possess only two distinct chemical solutes. pCTVB aggregates have been determined to be rod like with small angle neutron scattering (SANS) and static light scattering (SLS).[23] Aggregate length is controllable by varying reaction conditions, but cross-sectional diameter is set by the tail length of the monomer (d = 4 nm for the C_{16} alkane, or cetyl tail, denoted CTVB).[22–25] Polymerization conditions for the pCTVB used here produce aggregates of average length 120-150 nm.[26] Despite the molar equivalence between polymer and surfactant charges, pCTVB solutions do not exhibit the precipitation seen in some oppositely charged systems.[13,33,34] It is proposed that this stability is made possible by the ability of CTA⁺ to partition itself between aggregates and free solution.[27,28]

In light of what is known about these aggregates in solution and at the fluid/solid interface, this chapter aims to characterize the dynamic adsorption behavior of this system to the air/water interface.

3.2 MATERIALS AND METHODS

All pCTVB solutions (aggregate length = 120-150 nm) are prepared from dried material synthesized under the reaction conditions described elsewhere.[26] Deionized water, referred to as water, was produced using reverse osmosis water treated with a Barnstead Ultrapure water filtration system to 18.2 MΩ·cm resistivity. Sodium Chloride (NaCl) was purchased from Sigma (St. Louis, MO) and baked at 500 °C for 6 h to remove hydrates and impurities. Cetyltrimethylammonium bromide (CTAB) was purchased from Sigma (St. Louis, MO) and further purified by double recrystallization in ethanol. All solutions were diluted from a single stock solution in acid-washed vials. All solutions were prepared twice in the same vial to mitigate depletion of surface-active species to the vial walls.

Interfacial properties have been measured with a microtensiometer platform, described in detail in Section 1.2. All interfaces in this chapter are made between an air-filled, hydrophobized capillary and an aqueous reservoir. The equilibrium surface tension of water has been measured to be 72.4 mN/m and does not change within 1000 s. Dilatational modulus, E, has been measured at a frequency of 0.1 Hz. All studied interfaces exhibit elastic responses to dilation (phase angle $< 10°$) at this frequency. For clarity, only the magnitude of the complex modulus, $|E^*|$, is reported.

3.3 RESULTS

The adsorption to clean air/water interfaces is characterized by measuring surface tension during adsorption and then after exchange of the bulk solution with clean water. This approach allows the dynamic interfacial tension, equilibrium interfacial tension and adsorption reversibility to be determined as a function of bulk solution concentration. Figure 3.1 shows the dynamic surface tension of a spherical air/water interface that has been exposed to a 0.24 mg/ml pCTVB solution. Note that t = 0 corresponds to the formation of a clean interface as a bubble is ejected from the end of the capillary and new interface is formed. During the first ~1300 s, the surface tension decreases from its clean value (72.4 ± 0.5 mN/m) as material adsorbs from the bulk. After the surface tension reaches a plateau near 42 ± 0.5 mN/m, the dilatational modulus is measured. This appears as the block that spans ~3 mN/m starting at 1400 s. The surface tension then increases as the pCTVB reservoir solution is exchanged with deionized water. The exchange occurs for 1000 s, or 100 residence times (τ_R ~ 10 s). After exchange, the interface rests for 200 s before the dilatational modulus is measured again. At 3200 s, a new interface is created by ejecting the bubble, and surface tension is measured against the exchanged reservoir solution to verify that pCTVB has been removed from the reservoir during the solution exchange. The value of surface tension here coincides with that of a clean air/water interface. As shown previously,[25] pCTVB at this concentration lowers the interfacial tension of air/water interfaces by a significant amount, reaching approximately 40 mN/m. Adsorbed pCTVB layers at silica/water interface have been shown to maintain structure and alignment for several days
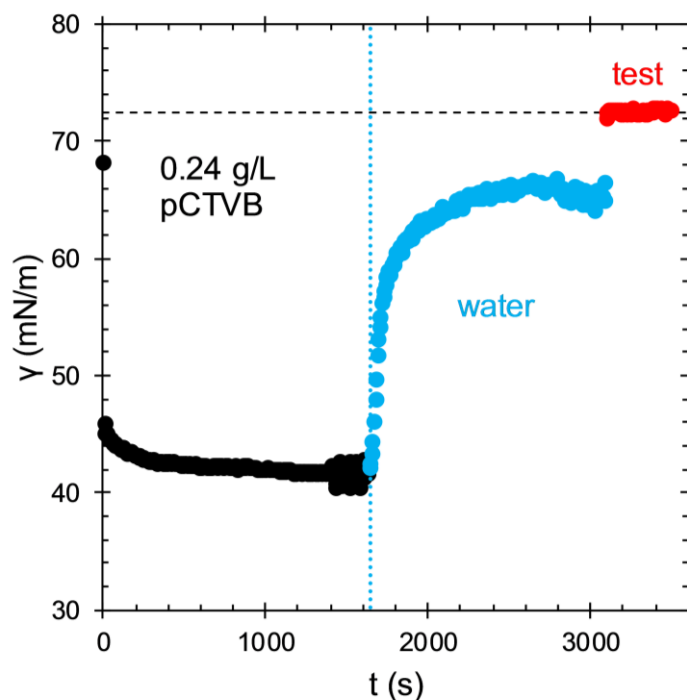
Figure 3.1. Dynamic surface tension of an aqueous 0.24 g/L pCTVB solution during adsorption (●) and reservoir exchange with water (●) and of a fresh interface after exchange (●). The dotted vertical line shows the onset of fluid exchange. The dashed horizontal line corresponds with the surface tension of a clean air/water interface.

after replacement of pCTVB solution with DI water using atomic force microscopy (AFM).[29] This contrasts with the partial desorption seen here at an air/water interface.

The experiment shown in Figure 3.1 is repeated for different bulk concentrations of pCTVB. Of interest is the region around the critical aggregation concentration, CAC. Figure 3.2a shows the steady state surface tension of an air/water interface for several concentrations of pCTVB (before and after solution exchange) and for the surfactant cetyltrimethylammonium hydroxide (CTAOH).[25] An interface is considered to be at steady state if its dynamic surface tension does not change beyond the resolution of ±0.5 mN/m within 600 seconds. Mass
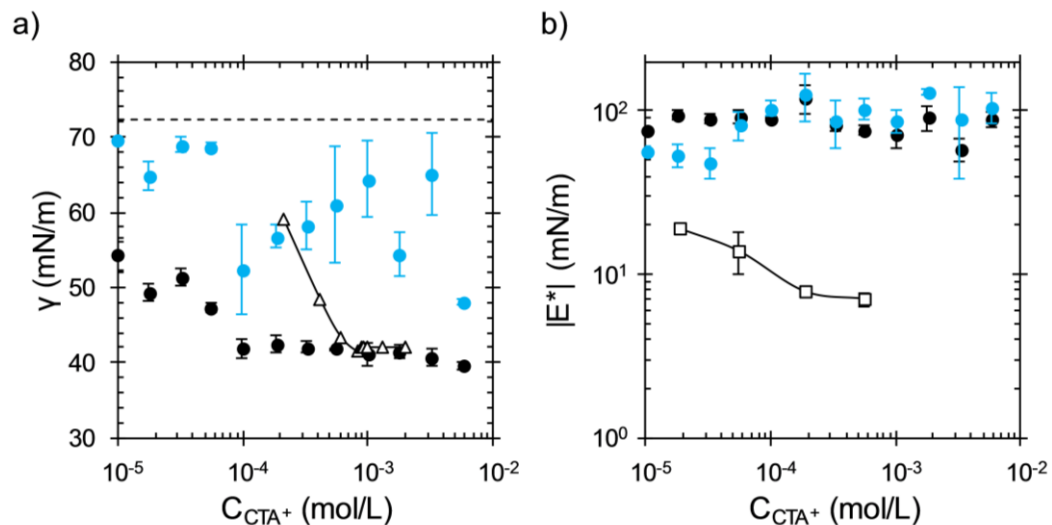
Figure 3.2. (a) Surface tension of pCTVB interfaces before (●) and after (●) reservoir exchange with water. CTAOH surface tension equilibria (△) are replotted from Kuntz and Walker.[25] (b) Magnitude of dilatational modulus at 0.1 Hz before and after reservoir exchange. The moduli of equilibrated CTAB (with 10^{-2} M NaCl) interfaces (□) are included as a reference. Error bars are standard deviations from at least three replicates.

concentration of pCTVB has been replotted as molar concentration of CTA^+ by dividing by the molecular mass of the CTVB monomer, 431.7 g/mol.

The most dilute pCTVB solutions show a steady state surface tension of 54 $\pm$ 2.2 mN/m. Steady state surface tension rapidly decreases with increasing concentration to a surface tension of 42 $\pm$ 1.5 mN/m. The surface tension reached at higher bulk concentrations is the same as that of CTAOH at and above its critical micelle concentration (CMC). The CAC is seen in the breakpoint of the steady surface tension curve of pCTVB at 10^{-4} M (0.043 g/L), occurring at a CTA^+ concentration ~10 times lower than the CMC of CTAOH which is $9 \cdot 10^{-4}$ M. The CAC coincides with the concentration at which the CTA^+ binding equilibrium has shifted almost entirely to the aggregate.[27,28] Beyond the CAC, increasing pCTVB

concentration results in minimal lowering of surface tension below its value at the CAC.

The desorption procedure for these data follow that outlined for Figure 3.1, 1000 s at $\tau_R \sim 10s$ rinsing with water followed by 200 s of rest. For the surfactant solutions of CTAOH and CTAB, the interfaces return to the clean interface value within a few residence times of rinsing the reservoir. Even after 1200 seconds, none of the adsorbed layers of pCTVB have completely desorbed. In other words, the clean air/water surface tension is not recovered. Instead, the rinsed interfaces maintain a stable surface tension denoted by the blue points in Figure 3.2a. Values of surface tension following rinsing are higher and more consistent below the CAC than above it. Below the CAC, surface tension after rinsing is high (~65-70 mN/m) but reproducible and has not returned to the value of a clean interface. Above the CAC, the surface tension after rinsing varies significantly from run to run, but in all cases, surface tension after rinsing does not return to its clean value. Above the CAC, surface tension after desorption does not seem to follow any simple dependency based either on features of the adsorption curves or operation conditions of the microtensiometer.

For example, a detailed analysis of the interface shapes does not show a preferred contact angle at the air/glass/water contact line of the microtensiometer that could arise by strong aggregate adsorption to the capillary, shown in Figure 3.3. Rinsing of the steady pCTVB interfaces results in a measurable, but difficult to reproduce quantitatively, level of surface-active material remaining on the interface. Data from Figure 3.2a have been replotted in Figure 3.3a as the change
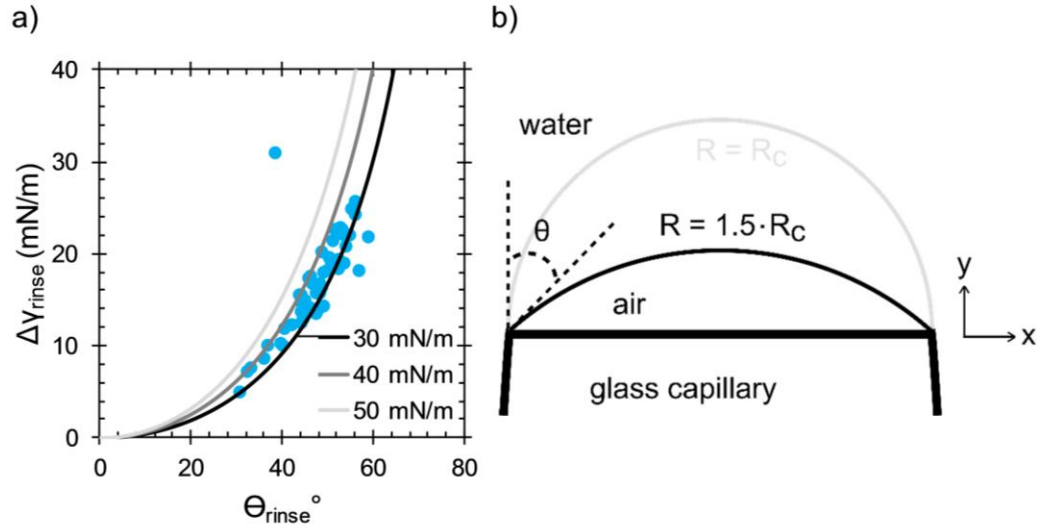
Figure 3.3. (a) Increase in surface tension after rinsing with after-rinse contact angle (●). The black, dark gray, and gray lines show the expected variation of surface tension with contact angle for minimum surface tension values of 30, 40, and 50 mN/m, respectively. (b) 2D illustration of the spherical air/water interface formed in the microtensiometer. The direction of gravitational force points into the page, but deformation of the interface due to gravity is negligible because of the small length scale of the interface ($R_c \sim 40$ µm).

in surface tension upon rinsing (steady state value subtracted from rinsed value), $\Delta\gamma_{rinse}$, with contact angle of the air/water/glass interface after solution exchange, θ_{rinse}. Contact angle is defined such that it takes on values between 0° for hemispherical ($R = R_c$) interfaces and 90° for perfectly flat ($R \to \infty$), shown in Figure 3.3b.

It is possible to rewrite the Laplace equation as a function of contact angle

$$\gamma = \frac{\Delta P \cdot R}{2} = \frac{\Delta P \cdot R_c}{2} \kappa(\theta) = \gamma_{min} \cdot \kappa(\theta) \tag{3.1}$$

where the isobaric operating conditions of the microtensiometer are given by the constant γ_{min} and the dynamics of adsorption are described by $\kappa(\theta)$. The exact functional form of $\kappa(\theta)$ is found with some simple geometry. The origin is defined

as the midpoint of the horizontal capillary edge in Figure 3.3b. In Cartesian coordinates, the shape of the air/water interface, shown as the thin black line, is described by a circle with radius R centered at a position $(0, b)$:

$$x^2 + (y-b)^2 = R^2. \tag{3.2}$$

The contact angle θ is determined by calculating $\dfrac{\partial y}{\partial x}$ at the air/water/glass contact points, $x = \pm R_c$ for the 2D interface:

$$\left.\frac{\partial y}{\partial x}\right|_{x=-R_c} = \frac{R_c}{\sqrt{R^2 - R_c^2}} = \tan\left(\frac{\pi}{2} - \theta\right). \tag{3.3}$$

Since $\kappa(\theta) = \dfrac{R}{R_c}$, rearrangement of Eq 3.3 reveals the following functional form of $\kappa(\theta)$:

$$\kappa(\theta) = \sqrt{\frac{1}{\tan^2\left(\dfrac{\pi}{2} - \theta\right)} + 1}. \tag{3.4}$$

Substituting Eq 3.4 into Eq 3.1 permits the calculation of surface tension as a function of contact angle for prescribed operating conditions (Laplace pressure and capillary radius).

It is now possible to calculate the expected variation of surface tension with contact angle in the microtensiometer. The black, dark gray, and gray lines in Figure 3.3a are three examples of a surface tension increase due to desorption for the case that the steady state adsorption occurs at $R = R_c$. In practice this occurs at small contact angles, typically $\theta < 10°$. The data in Figure 3.3a do not favor a particular contact angle as a result of the exchange of pCTVB solution with DI water. The outlier near $(38°, 31 \text{ mN/m})$ results from an increase of Laplace pressure

43

during the rinse. This is sometimes necessary to prevent the interface from becoming too flat, which increases the uncertainty in the measurement of R.

Figure 3.2b shows the magnitude of the complex dilatational modulus, $|E^*|$, at an applied frequency of 0.1 Hz for pCTVB (both before and after reservoir exchange) and for CTAB. Although not useful to determine interfacial relaxations, measurement of dilatational modulus at a single frequency has been shown to be a useful compositional probe of adsorbed layers.[19] $|E^*|$ of pCTVB interfaces both before and after solution exchange are substantially higher than those of CTAB layers, a feature of adsorbed polyelectrolyte layers seen elsewhere.[20,35,36] For the CTAB experiments, the fact that transport from the bulk solution is likely to be on similar timescales with the frequency of the dilatational moduli measurements could give rise to the concentration dependence;[37,38] these results are provided for comparison of magnitude. Below the CAC, $|E^*|$ after solution exchange is lower than that before exchange. This region corresponds with the same location on Figure 3.2a of greater, more consistent desorption. A different trend is seen above the CAC, where dilatational moduli after rinse are indistinguishable from those before rinsing, suggesting that transport to and from the interface prior to exchange does not noticeably affect the measurement of $|E^*|$.[37] This differs from the conclusion that would be reached by assuming reversible adsorption of the aggregates and applying the Lucassen and van den Tempel (LVDT) analysis of relaxation by diffusion-limited, reversible adsorption. When performed using the diffusivity of the pCTVB aggregate (2×10^{-11} m^2/s)[25] and the isotherm information of CTAB at the CMC in Figure 3.3, the LVDT analysis shows that diffusion-limited
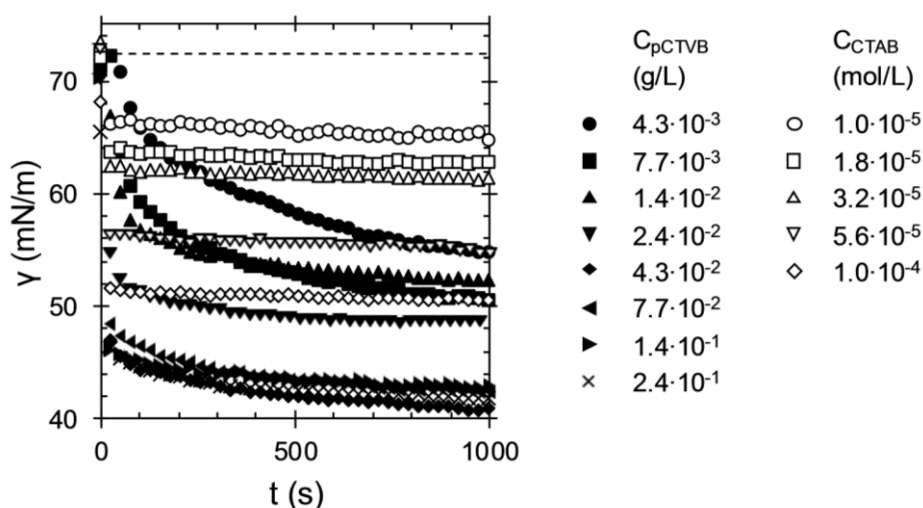
Figure 3.4. Dynamic surface tension for solutions of pCTVB (filled) and dilute CTAB in 10 mM NaCl (open) during the first 1000 s of adsorption. Symbol shapes denote solutions with identical CTA$^+$ concentration. Some data points have been omitted for clarity.

sorption is relevant to measurements of dilatational mechanics at a frequency of 0.1 Hz. For a freely desorbing species, this relaxation would be even more influential at highly curved interfaces and larger diffusivities. Overall, the dilatational moduli of the aggregate-laden interfaces are large and less dependent on the bulk concentration than the surface tension. Since the dilatational modulus is mostly independent of the surface tension of the interface, these aggregates would provide a means to generate elastic interfaces with either high or low surface tension.

Characterization of the interfaces in this chapter provides dynamic interfacial tension (or transport properties) of the pCTVB aggregates to an air/water interface. Since t = 0 is well defined in these experiments, surface relaxations can be modeled from clean to equilibrium. Figure 3.4 shows dynamic surface tension for CTAB in 10 mM NaCl and pCTVB (no added electrolyte) for several bulk concentrations. This salt concentration was chosen because it has been shown to

be sufficient to overcome slow adsorption times in ionic systems by screening charges that accumulate on the interface with minimal effect on equilibrium surface tension.[39,40]

For easier comparison, CTAB and pCTVB are identified in the figure by CTA^+ concentration. Surface tension begins at the value of a clean air/water interface, 72.4 ± 0.5 mN/m, and decreases with time. Within 1000 s, all CTAB interfaces have equilibrated while pCTVB interfaces have not yet reached steady state. For equivalent values of C_{CTA^+}, pCTVB layers reach lower values of surface tension than layers of CTAB alone, but they do so more slowly. Dynamic surface tension of pCTVB layers takes longer than that of CTAB to reach the equilibrium value of the CTAB layers. This is more pronounced at lower concentrations (C_{CTA^+} $= 10^{-5}$ M, $1.8 \cdot 10^{-5}$ M and $3.2 \cdot 10^{-5}$ M). The most concentrated pCTVB solutions are all above the CAC and reach similar values of steady state surface tension.

It cannot be known from surface tension data alone which constituent(s) of the pCTVB aggregate adsorb to the air/water interface.[25] Figure 3.1 shows incomplete desorption from the interface, a marked difference from CTA^+, known to desorb completely from air/water interfaces.[41] Incomplete desorption of the pCTVB layer to a surface pressure of 5 mN/m suggests that the polyelectrolyte coadsorbs with the surfactant counterion.[42] Coadsorption agrees with observations at silica/water and mica/water interfaces.[29–32] In Figure 3.2a, incomplete desorption is seen for each pCTVB solution. Figure 3.2b shows that despite substantial desorption for some interfaces ($\Delta\gamma \approx 25$ mN/m) $|E^*|$ remains largely unchanged. A large dilatational modulus before and after adsorption suggests that polyelectrolyte

a)

b)
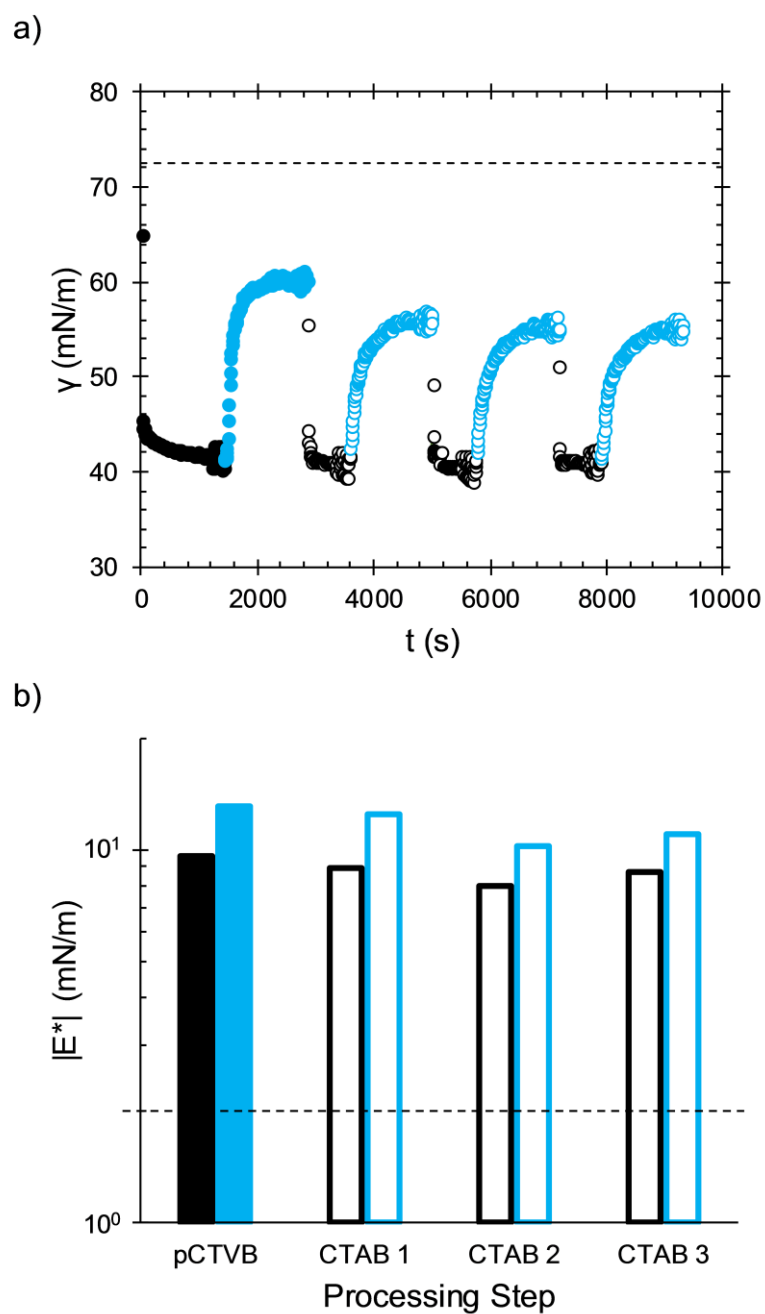
Figure 3.5. Dynamic surface tension (a) and dilatational modulus (b) after adsorption from a solution of 0.24 mg/ml pCTVB followed by alternating reservoir exchange steps with water and 10^{-4} M CTAB ($0.1 \times$ CMC). Black and blue bars denote the dilatational modulus with and without material in the bulk, respectively.

remains adsorbed despite desorption of some surface-active material. Above the CAC, values of $|E^*|$ are higher, demonstrating that more polyelectrolyte remains than below the CAC. These results are consistent with binding isotherm data of pCTVB with a twist: CTA^+ now partitions between free solution and aggregates that are no longer in solution, but instead adsorbed.[28] To test this interpretation, an experiment has been designed to probe the CTA^+ equilibrium between polyelectrolyte stranded at the interface and that in free solution.

Figure 3.5 shows the dynamic surface tension of an air/water interface initially in contact with a solution of 0.24 g/L pCTVB ($5.6 \cdot 10^{-4}$ M CTA^+), then subjected to alternating processing steps of DI and 10^{-4} M CTAB. This concentration of CTAB is equivalent to the total amount of CTA^+ in a pCTVB solution at the CAC. pCTVB initially adsorbs from solution to a surface tension of 42 mN/m and partially desorbs after solution exchange with DI water, as seen in Figure 3.1. 20 mL (10 reservoir volumes) of 10^{-4} M CTAB ($0.1 \times$ CMC) is then pipetted into the reservoir in 1 mL increments. Reservoir fluid is continuously removed to maintain a constant volume in the reservoir. Surface tension of the interface decreases to 41 mN/m after CTAB addition, close to that of the initial adsorption. The CTAB solution is then exchanged with DI water, and surface tension increases to 55 mN/m. The CTAB addition and DI water exchange steps are repeated twice. Dilatational modulus is measured and remains large (~100 mN/m) after each step.

The experiment shown in Figure 3.5 validates the interpretation of CTA^+ equilibrium between adsorbed polyelectrolyte and free solution by showing that

interfacial pCTVB layers can be stripped of some surfactant and then replenished with CTAB, restoring interfacial properties to their values before the exchange cycle. CTAB at the concentration used in Figure 3.5 (10^{-4} M) adsorbs to bare air/water interfaces to a lesser extent than that seen in Figure 3.5, $\gamma = 50$ mN/m (CTAB equilibrium adsorption in Figure 3.8).[40] The persistence of negatively charged polyelectrolyte after desorption of some CTA^+ leaves an interface more desirable to CTAB than bare air/water. This experiment provides an example of the potential for processing interfacial layers with sequential changes in bulk solution, taking advantage of multicomponent adsorption.

3.4 DISCUSSION

Although dynamic surface tension has enabled the qualitative differentiation between the adsorption and desorption of pCTVB and CTAB, thus far all quantitative insight into the composition of adsorbed pCTVB layers has come from analyzing equilibrium interfacial properties. As demonstrated previously, analysis of dynamic surface tension can be used to determine the mechanism of adsorption.[43,44] Once the mechanism is known, adsorption dynamics can be predicted for conditions not studied here (different geometries, solution conditions, flow).

Figure 3.6 shows normalized surface pressures, Φ, for pCTVB (filled symbols) and dilute CTAB with 10^{-2} M NaCl (empty symbols) calculated from the dynamics shown in Figure 3.4. A normalized surface pressure that varies from zero (clean interface) to one (steady state) is calculated by dividing dynamic surface pressure (difference between clean and dynamic surface tension) by steady state
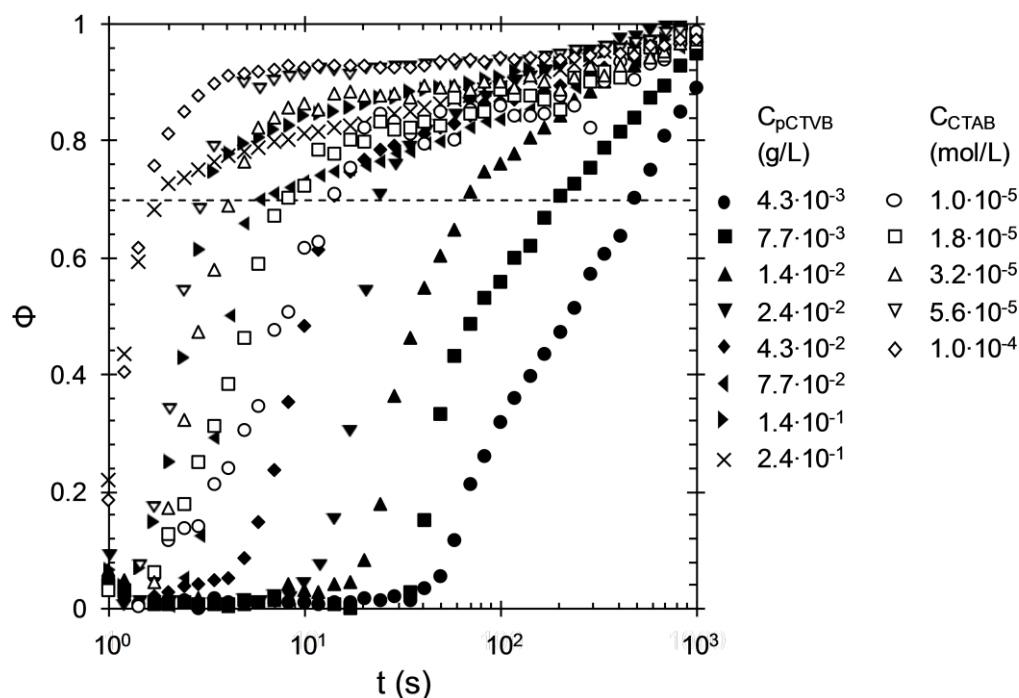
Figure 3.6. Normalized dynamic surface pressure for pCTVB (filled) and CTAB with 10 mM NaCl (empty) during the first 1000 s of adsorption. Surface pressure is normalized by its final value prior to solution exchange with deionized water. Shared symbols denote solutions with identical CTA^+ concentration. Above 0.1 mM CTAB and 0.24 mg/ml pCTVB, short-time dynamics occur too quickly to be resolved by the camera at 15 frames per second. Some data points have been omitted for clarity.

surface pressure. While this introduces some uncertainty because adsorbed layers have not truly reached equilibrium, normalization emphasizes the nature of the adsorption. Data for both systems in Figure 3.6 show a rapid increase in surface pressure followed by a plateau region of slowly increasing surface pressure with pCTVB demonstrating a more pronounced region of slower adsorption. Adsorption from lower concentrations takes longer than that from higher ones for both CTAB and pCTVB. For the same total C_{CTA^+}, adsorption takes longer for pCTVB. To quantify the timescale of adsorption, a time τ_Φ is defined at which a
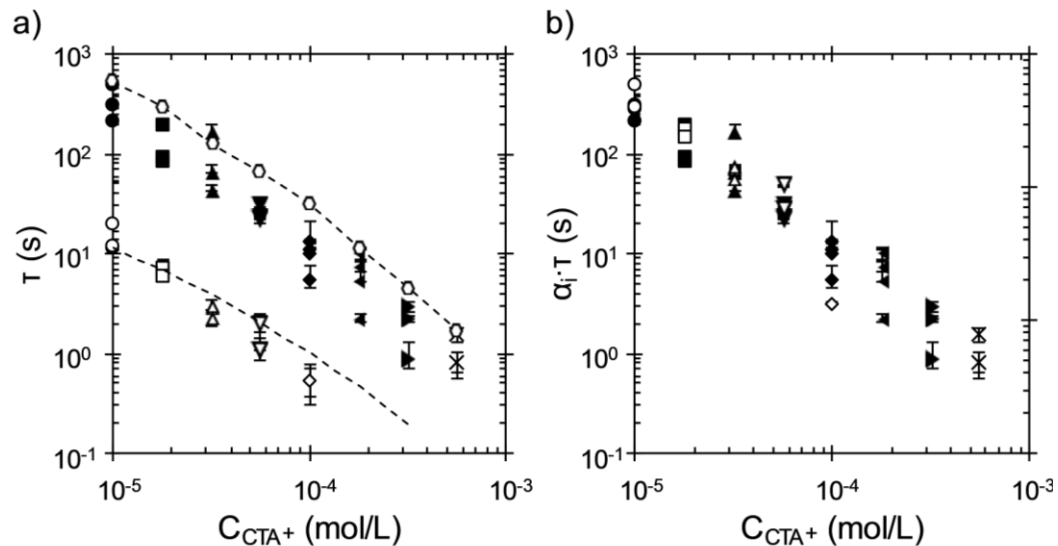
Figure 3.7. (a) Adsorption time with total bulk CTA$^+$ concentration for pCTVB (filled) and CTAB (open). Adsorption times are reported for a fractional surface pressure $\Phi = 0.7$. The dashed line denotes calculated diffusion times for CTAB for a spherical geometry.[45] Predictions of spherical diffusion times for pCTVB are shown by open hexagons.[25] The dashed line between these points is a guide for the eye. Error bars are calculated by propagation of known experimental errors. (b) Adsorption times scaled by the ratio of diffusivities D_i/D_{pCTVB} (i = CTAB, pCTVB).

certain fractional surface pressure Φ is reached. The dashed line in Fig 3-6 correspond with $\Phi = 0.7$, which occurs near the transition from rapid adsorption to the slower region. While the choice of a specific value of Φ is arbitrary, selecting a timescale in this way is a consistent measure of adsorption without knowing the actual amount of adsorbed material or adopting an isotherm and its model parameters.

Figure 3.7a shows both the observed and predicted adsorption times of pCTVB and CTAB in 10^{-2} M NaCl for several concentrations. Measured adsorption time τ_Φ for $\Phi = 0.7$ is replotted from Figure 3.6 against C_{CTA^+}. The timescale at $\Phi = 0.7$ decreases with increasing C_{CTA^+} (higher concentrations have faster dynamics). Both data show a similar negative slope and lie approximately

an order of magnitude apart along either the time or the concentration axis. Figure 3.7b shows that the data nicely collapse when the time axis is rescaled by a constant value, α_i, the quotient of the diffusivity of species i (either CTAB, $D_{CTAB} = 5 \times 10^{-10}$ m^2/s, or pCTVB, $D_{pCTVB} = 2 \times 10^{-11}$ m^2/s) and D_{pCTVB}.[25,45] This apparent dependence of adsorption time on diffusivity suggests that diffusion is the rate-limiting step for adsorption at short times, often referred to as diffusion-limited adsorption. To test this, diffusive adsorption of both surfactant and aggregates to a spherical interface has been modeled.

Calculating an adsorption timescale requires detailed knowledge of both the transport mechanism and the equilibrium adsorption isotherm. This calculation is straightforward for smaller surfactants, and the procedure outlined by Alvarez *et al.* is followed here.[44] This is based on the analysis of Ward & Tordai and uses a simple mixing rule for the scaling of time constants between the radial and planar regimes.[43] The appropriate timescale, τ_s, for surfactant adsorption to a spherical interface is given by the following combination of planar depletion depth, h_p, spherical depletion depth, h_s, and surfactant diffusivity, D,

$$\tau_s = \frac{\left(h_s^3 h_p\right)^{1/2}}{D}, \tag{3.5}$$

where the spherical depletion depth depends on the radius of curvature, b, and h_p by

$$h_s = b\left[\left(\frac{3h_p}{b} + 1\right)^{1/3} - 1\right]. \tag{3.6}$$

The scaling for planar depletion depth, the quotient of equilibrium surface excess, Γ_{eq}, and bulk surfactant concentration, C_b, comes directly from the governing diffusion-adsorption equations:

$$h_p = \frac{\Gamma_{eq}}{C_b}.^{46}$$

(3.7)

Since the surface excess of CTAB is not known directly, an isotherm model must be used to connect surface excess with measured quantities, bulk concentration and surface tension. The Frumkin isotherm is used here as it has been shown to accurately describe adsorption of many charged surfactants.[47] Equilibrium CTAB data and isotherm parameters are provided in Figure 3.8.

Figure 3.8 shows the equilibrium adsorption data for CTAB that have been regressed using the Frumkin isotherm, of which a good discussion can be found here.[47] The Frumkin isotherm relates C_b and Γ such that

$$C_b = \frac{a\Gamma}{\Gamma_\infty - \Gamma} e^{h\left(\frac{\Gamma}{\Gamma_\infty}\right)}$$

(3.8)

where a is surfactant turnover concentration and h is a dimensionless measure of interaction between adsorbed molecules. The corresponding equation of state is given by

$$\gamma = \gamma_0 + RT\Gamma_\infty \left[\ln\left(1 - \frac{\Gamma}{\Gamma_\infty}\right) - \frac{h}{2}\left(\frac{\Gamma}{\Gamma_\infty}\right)^2 \right].$$

(3.9)

An analytical relationship cannot be obtained between γ and C_b, requiring simultaneous regression of both equations to determine the three model parameters.

Using a radius $b = 40$ μm as a nominal value during an experiment, diffusion time for adsorbing CTAB can be predicted (the dashed line in Figure 3.7).

53
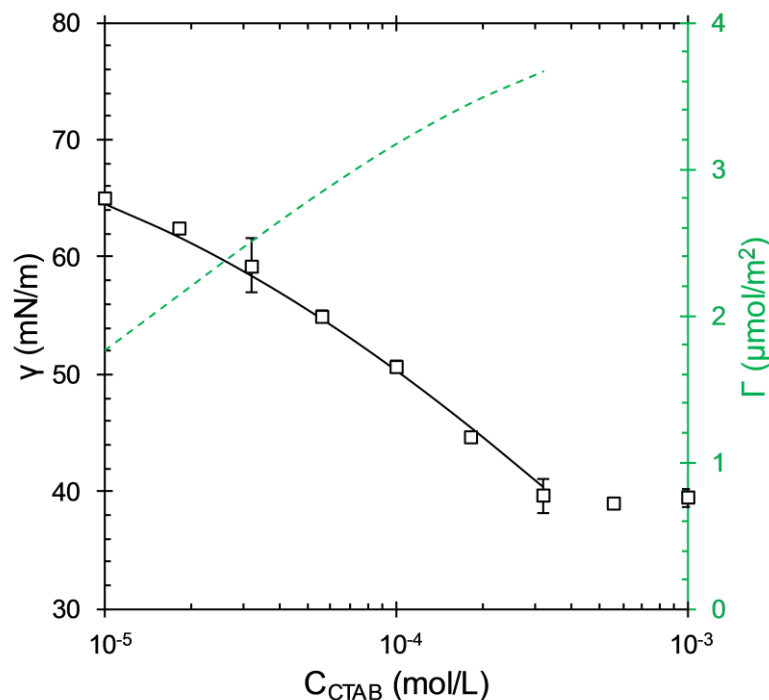
Figure 3.8. Equilibrium surface tension data (□) and isotherm fit for CTAB in 10 mM NaCl. Solid and dashed lines correspond with predictions of surface tension and surface excess, respectively, by the Frumkin model. Model parameters were determined by the local solver fmincon in MATLAB for a variety of starting conditions. Shown here is the fit that yielded the lowest mean squared error, 0.8373. This fit possesses the following parameter values: $\Gamma_\infty = 4.1262 \cdot 10^{-6}$ mol/m^2, $a = 4.8861 \cdot 10^{-6}$ mol/L, and $h = 2.3619$. Error bars are standard deviations from three replicates. Error bars smaller than the symbols are omitted.

The predicted diffusion times show good agreement with τ_Φ. If it is assumed that adsorbed polyelectrolyte contributes to surface pressure only minimally and does not affect the surface equation of state of the surfactant, then the apparent surface excess of CTA$^+$ on pCTVB interfaces can be estimated using Eq 3.9 for a given pCTVB surface pressure. The procedure of Alvarez *et al.* is repeated for these apparent surface excesses using the diffusivity of the aggregates instead of that of a surfactant monomer in Eq 3.5. A spherical diffusion time is calculated for each pCTVB data point and shown by open hexagons in Figure 3.7a. These points

slightly overestimate τ_Φ of the aggregates, but capture the shape of the data, suggesting that the surfactant CTA$^+$ arrives at the interface as part of an intact aggregate rather than as a freely diffusing species. Adsorption as an aggregate is also an appealing explanation for adsorption to solid/water interfaces where pCTVB has been shown to adsorb directly onto the substrate as intact aggregates.[29,30,32]

The interfacial properties of the pCTVB aggregate studied here show similarities to those seen in other polyelectrolyte/surfactant systems. Steady state interfacial tension data for pCTVB show the familiar synergistic lowering of interfacial tension below that of the pure surfactant at the same surfactant concentration, although without the nonmonotonic behavior observed in some systems.[18,33,48] The dilatational moduli of steady-state pCTVB layers are large and highly elastic, ~100 mN/m with $\phi < 10°$ at $\omega = 0.1$ Hz. The values of dilatational modulus reported here are similar in magnitude to the largest values reported by Noskov *et al.* for a similar system, sodium poly(styrene sulfonate) (NaPSS) and dodecyltrimethylammonium bromide (DTAB).[20] However, pCTVB interfaces do not show a reduction in modulus with increasing surfactant concentration that is associated with the reduced interfacial activity of NaPSS/DTAB complexes at charge parity. Monteux *et al.* argued that as NaPSS/DTAB complexes become increasingly insoluble by addition of surfactant above the CAC, the entrapment of the NaPSS in precipitating aggregates prevents adsorption of the elasticity-imparting polyelectrolyte to the interface.[17,19] Since pCTVB aggregates are

synthesized (and soluble) at charge parity, pVB$^-$ is available to the interface both above and below the CAC.

3.5 SUMMARY

Adsorbed layers of the polyelectrolyte-surfactant aggregate pCTVB at the air/water interface are characterized by large surface pressures (~ 30 mN/m above CAC) and highly elastic dilatational moduli at 0.1 Hz (~ 100 mN/m, $\phi < 10°$). Both surfactant and polyelectrolyte constituents of the pCTVB aggregate play crucial roles in its interfacial behavior. The surfactant CTA$^+$ is chiefly responsible for lowering surface tension of pCTVB interfaces. CTA$^+$ is free to partition itself between free solution and aggregates even when those aggregates are adsorbed at the air/water interface. The polyelectrolyte pVB$^-$ adsorbs strongly at all concentrations studied and does so irreversibly above the CAC. During adsorption, surfactant and polyelectrolyte remain bound together within the aggregate, resulting in the large diffusivity of the aggregate (relative to that of the surfactant monomer) being relevant to the diffusion-limited adsorption observed at spherical interfaces. The strong adsorption of the aggregates produces air/water interfaces that can be reversibly processed with solvent and additional surfactant.

(1)   Mayer; Terroine. *C. R. Seances Soc. Biol. Fil.* **1907**, *62*, 398–400.

(2)   Dervichian, D. G. *Discuss. Faraday Soc.* **1949**, *6*, 7.

(3)   Saito, S. *Kolloid Z.* **1957**, *1*, 19–29.

(4)   *Interactions of Surfactants with Polymers and Proteins*; Goddard, E. D., Ananthapadmanabhan, K. P., Eds.; CRC Press, Inc.: Boca Raton, 1993.

(5)   Braun, L.; Uhlig, M.; von Klitzing, R.; Campbell, R. A. *Adv. Colloid Interface Sci.* **2017**, *247* (July), 130–148.

(6)   Jones, M. *J. Colloid Interface Sci.* **1968**, *26* (4), 532–533.

(7)   Arai, H.; Murata, M.; Shinoda, K. *J. Colloid Interface Sci.* **1971**, *37* (1), 223–227.

(8)   Shirahama, K. *Colloid Polym. Sci. Kolloid Zeitschrift Zeitschrift fu r Polym.* **1974**, *252* (11), 978–981.

(9)   Taylor, D. J. F.; Thomas, R. K.; Penfold, J. *Adv. Colloid Interface Sci.* **2007**, *132* (2), 69–110.

(10)   Bain, C. D.; Claesson, P. M.; Langevin, D.; Meszaros, R.; Nylander, T.; Stubenrauch, C.; Titmuss, S.; von Klitzing, R. *Adv. Colloid Interface Sci.* **2010**, *155* (1–2), 32–49.

(11)   Jones, M. N. *J. Colloid Interface Sci.* **1967**, *23* (1), 36–42.

(12)   Lange, H. *Kolloid Z.* **1971**, *243* (2), 101.

(13)   Staples, E.; Tucker, I.; Penfold, J.; Warren, N.; Thomas, R. K.; Taylor, D. J. F. *Langmuir* **2002**, *18* (3), 5147–5153.

(14)   Penfold, J.; Tucker, I.; Thomas, R.; Zhang, J. *Langmuir* **2005**, *21*, 10061–10073.

(15)   Purcell, J. P.; Thomas, R. K.; Penfold, J.; Howe, A. M. *Colloids Surfaces A Physicochemical Eng. Asp.* **1995**, *94*, 125–130.

(16)   Asnacios, A.; Langevin, D.; Argillier, J. F. *Eur. Phys. J. B* **1998**, *5* (4), 905–911.

(17)   Monteux, C.; Llauro, M. F.; Baigl, D.; Williams, C. E.; Anthony, O.; Bergeron, V. *Langmuir* **2004**, *20* (13), 5358–5366.

(18)   Bhattacharyya, A.; Monroy, F.; Langevin, D.; Argillier, J. F. *Langmuir* **2000**, *16* (23), 8727–8732.

(19)   Monteux, C.; Fuller, G. G.; Bergeron, V. *J. Phys. Chem. B* **2004**, *108* (42), 16473–16482.

(20)   Noskov, B. A.; Loglio, G.; Miller, R. *J. Phys. Chem. B* **2004**, *108* (48), 18615–18622.

(21)   Noskov, B. A. *Curr. Opin. Colloid Interface Sci.* **2010**, *15* (4), 229–236.

(22)   Kline, S. R. *Langmuir* **1999**, *15* (8), 2726–2732.

(23)   Gerber, M. J.; Kline, S. R.; Walker, L. M. *Langmuir* **2004**, *20* (20), 8510–8516.

(24)   Gerber, M. J.; Walker, L. M. *Langmuir* **2006**, *22* (3), 941–948.

(25)   Kuntz, D. M.; Walker, L. M. *J. Phys. Chem. B* **2007**, *111* (23), 6417–6424.

(26)   Kuntz, D. M.; Walker, L. M. *Soft Matter* **2008**, *4* (2), 286.

(27)   Kuntz, D. M.; Walker, L. M. *Ind. Eng. Chem. Res.* **2009**, *48* (5), 2430–2435.

(28)   Lam, V. D.; Walker, L. M. *Langmuir* **2010**, *26* (13), 10489–10496.

(29)   Biggs, S.; Walker, L. M.; Kline, S. R. *Nano Lett.* **2002**, *2* (12), 1409–1412.

(30)   Biggs, S.; Kline, S. R.; Walker, L. M. *Langmuir* **2004**, *20* (4), 1085–1094.

(31)   Biggs, S.; Labarre, M.; Hodges, C.; Walker, L. M.; Webber, G. B. *Langmuir* **2007**, *23* (15), 8094–8102.

(32)   Hodges, C. S.; Biggs, S.; Walker, L. *Langmuir* **2009**, *25* (8), 4484–4489.

(33)   Staples, E.; Tucker, I.; Penfold, J.; Warren, N.; Thomas, R. K. *Langmuir* **2002**, *18*, 5139–5146.

(34)   Campbell, R. A.; Angus-Smyth, A.; Yanez Arteta, M.; Tonigold, K.; Nylander, T.; Varga, I. *J. Phys. Chem. Lett.* **2010**, *1* (20), 3021–3026.

(35)   Noskov, B. A.; Grigoriev, D. O.; Lin, S. Y.; Loglio, G.; Miller, R. *Langmuir* **2007**, *23*, 9641–9651.

(36)   Noskov, B. A.; Nuzhnov, S. N.; Loglio, G.; Miller, R. *Macromolecules* **2004**, *37* (7), 2519–2526.

(37)   Lucassen, J.; Van Den Tempel, M. *Chem. Eng. Sci.* **1972**, *27* (6), 1283–1291.

(38)   Reichert, M. D.; Alvarez, N. J.; Brooks, C. F.; Grillet, A. M.; Mondy, L. A.; Anna, S. L.; Walker, L. M. *Colloids Surfaces A Physicochem. Eng. Asp.* **2015**, *467*, 135–142.

(39)   Okuda, H.; Imae, T.; Ikeda, S. *Colloids and Surfaces* **1987**, *27* (1–3), 187–200.

(40)   Adamczyk, Z.; Para, G.; Warszyński, P. *Langmuir* **1999**, *15* (24), 8383–8387.

(41)   Svitova, T. F.; Wetherbee, M. J.; Radke, C. J. *J. Colloid Interface Sci.* **2003**, *261* (1), 170–179.

(42)   Théodoly, O.; Ober, R.; Williams, C. E. *Eur. Phys. J. E* **2001**, *5* (1), 51–58.

(43)   Ward, A. F. H.; Tordai, L. *J. Chem. Phys.* **1946**, *14* (7), 453–461.

(44)   Alvarez, N. J.; Walker, L. M.; Anna, S. L. *Phys. Rev. E - Stat. Nonlinear, Soft Matter Phys.* **2010**, *82* (1), 1–8.

(45)   Lindman, B.; Puyal, M. *J. Phys. Chem.* **1984**, *88* (21), 5048–5057.

(46)   Alvarez, N. J.; Walker, L. M.; Anna, S. L. *Langmuir* **2010**, *26* (16), 13310–13319.

(47)   Eastoe, J.; Nave, S.; Downer, A.; Paul, A.; Rankin, A.; Penfold, J. *Langmuir* **2000**, *16* (25), 4511–4518.

(48)   Monteux, C.; Williams, C. E.; Meunier, J.; Anthony, O.; Bergeron, V. *Langmuir* **2004**, *20* (1), 57–63.

CHAPTER 4

STRANDING SURFACE-ACTIVE POLYPEPTOIDS AT THE AIR/WATER INTERFACE BY CONTROLLING SOLVENT QUALITY

4.1 INTRODUCTION

Most of the existing literature on small-molecule surfactants describes their behavior at equilibrium. In aqueous solution, surfactant self-assembly follows the rules of mass action.[1–4] Surfactant molecules distribute between free solution and self-assembled structures according to a balance of thermodynamically reversible rates. The type of structure that forms is determined by a packing parameter, a geometric descriptor of the balance between hydrophilic head and hydrophobic tail.[5] For example, an anionic surfactant, sodium dodecyl sulfate, transitions from spherical to ellipsoidal micelles with increasing ionic strength because of the reduction is size of the head group from Debye screening.[6] A notable descriptor of nonequilibrium behavior is the hydrophile-lypophile balance (HLB), originally developed to determine the type of oil/water emulsions formed using ethylene-oxide-containing surfactants.[7]

Surfactant adsorption to fluid/fluid interfaces is also predominantly studied and modeled with equilibrium in mind.[8] Many surfactants adsorb according to the Gibbs adsorption isotherm, Eq 2.1, which relates the surface excess concentration of surfactant, interfacial tension, and bulk concentration of surfactant. Eq 2.1 is often the first stop for modeling surfactant adsorption as its high-concentration limit yields the surface excess of a saturated monolayer, Γ_∞, which can be used to calculate the interfacial area occupied by a single adsorbed surfactant. For Eq 2.1 to be valid, the interface must be in thermodynamic equilibrium with the adjacent

solution, which is assumed to be ideal. For the semi-dilute concentrations over which many surfactants exhibit the greatest change in their surface activity, this is often a good assumption.

One of the simplest tests of the validity of the Gibbs adsorption equation is by measuring surfactant desorption by exchanging the adjacent solution with one of pure solvent and no surfactant.[9] For an adsorbed surfactant to be at thermodynamic equilibrium, it must be free to desorb completely. If the surfactant is reversibly adsorbed, then solution exchange causes interfacial tension to increase to its "clean" value (prior to any adsorption). More interesting are circumstances in which surfactants adsorb irreversibly, that is that interfacial tension increases by a little or not at all during solution exchange. Irreversibly adsorbed systems can be used to create processable interfaces with properties that differ from interfaces at equilibrium.[10–12] For example, complexes of silica nanoparticles and a cationic surfactant, cetyltrimethylammonium bromide, adsorb to air/water interfaces when the silica nanoparticles are not surface active without the surfactant.[13] The surfactant completely desorbs from the interface, stranding the nanoparticles at the interface and imparting mechanical elasticity as a result.

This chapter furthers the study of irreversibly adsorbed surfactants at fluid/fluid interfaces by looking at the extreme scenario of stranding a surfactant to air/solution interfaces by exchanging the surfactant solution following initial adsorption with a nonsolvent for the surfactant. Four surface-active sequences of an amphiphilic polypeptoid. Polypeptoids are achiral, polypeptide analogues with substantially reduced hydrogen bonding. Precise sequence specificity enables the
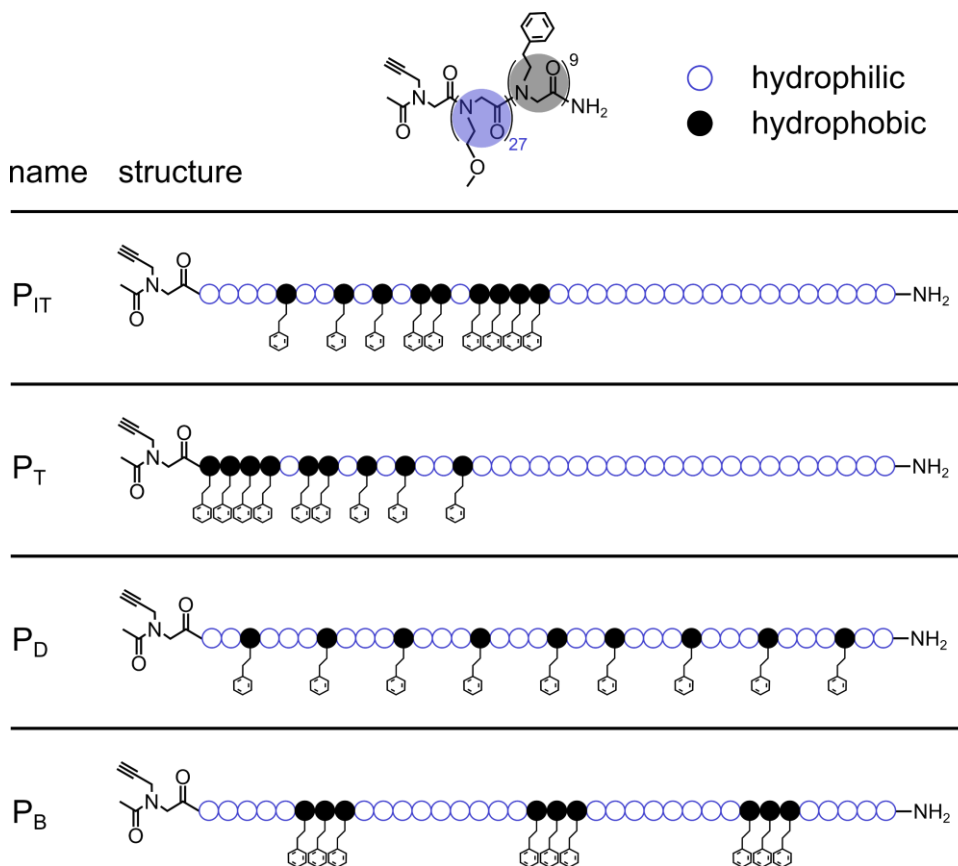
Figure 4.1. Chemical structure of polypeptoid molecules for the four sequences studied: distributed (P_D), blocky (P_B), taper (P_T) and inverse taper (P_{IT}). All four sequences have the same chemical formula, provided at the top, with a molecular weight of 4712 g/mol.

construction of structure-property relationships at the interface for subtle changes in the order of hydrophilic and hydrophobic moieties.

4.2 MATERIALS AND METHODS

Figure 4.1 shows the structure of the four polypeptoid sequences used in this chapter: inverse tapered (P_{IT}), tapered (P_T), distributed (P_D) and blocky (P_B). They are named according to the distribution of hydrophobic moieties in the backbone. Acetonitrile (ACN, 99%+) was purchased from Sigma. Deionized water, referred to as water, with a resistivity of 18.2 MΩ·cm was produced using a
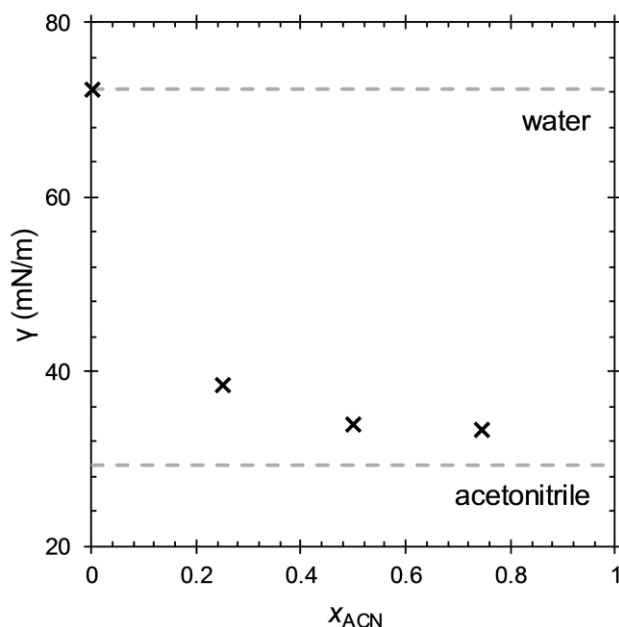
Figure 4.2. Surface tension of acetonitrile/water mixtures measured with the microtensiometer. Dashed lines are the surface tensions of the pure solvents.[17]

Barnstead Ultrapure water filtration system. Solutions were prepared in acid-washed vials.

These four polypeptoids are readily soluble in acetonitrile but insoluble in pure water. Polypeptoid solutions were prepared from lyophilized material,[14,15] ignoring nonideal mixing of water and ACN.[16] Mixtures have been prepared on a volumetric basis. For example, a 25/75 mixture of ACN/water is 25% ACN and 75% water by volume. The 25/75 mixture of ACN/water possesses just enough ACN to completely solubilize the polypeptoids.

Interfacial properties have been measured with a microtensiometer platform, described in detail in Section 1.2. All interfaces in this chapter are between an air-filled, hydrophobized capillary and a reservoir containing water or an ACN/water mixture. Water and ACN possess drastically different equilibrium surface tensions. Figure 4.2 shows the equilibrium surface tension of mixtures of

ACN and water as a function of the volume fraction of ACN, x_{ACN}, measured with the microtensiometer. The dashed lines denote the surface tension of individual components.[17] Equilibrium surface tensions of the three mixtures shown are much closer to the surface tension of pure acetonitrile than to that of water. In the absence of surface-active components, the equilibrium surface tension of ACN/water mixtures develops instantaneously and does not change with time.

4.3 RESULTS AND DISCUSSION

Figure 4.3 shows the development of an air/solution interface in a reservoir of 0.1 mM P_{IT} in 50/50 ACN/water. At time $t = 0$ s, a fresh interface is created and equilibrated (black diamonds). The interface instantaneously develops a surface tension ~35 mN/m that remains unchanged for 1600 s. The dashed, black line denotes the equilibrium surface tension of the 50/50 solvent mixture without P_{IT}. The overlap between the data points and dashed line at $t < 1600$ s shows that 0.1 mM P_{IT} does not adsorb to the air/solution interface from a 50/50 ACN/water mixture.

At $t = 1600$ s, 1 mL water is added to the reservoir that contains 1 mL of P_{IT} solution. Addition of water simultaneously decreases the concentration of P_{IT} from 0.1 mM to 0.05 mM and changes the solvent mixture from 50/50 to 25/75 ACN/water. This increases the surface tension of the air/solution interface initially to ~39 mN/m, followed by a decrease to 35 mN/m over 1000 s (green diamonds). The dashed green line denotes the increase in equilibrium surface tension that accompanies a change in x_{ACN} (see Figure 4.2). A decrease in surface tension below the equilibrium value shows the P_{IT} is surface active in the 25/75 ACN/water
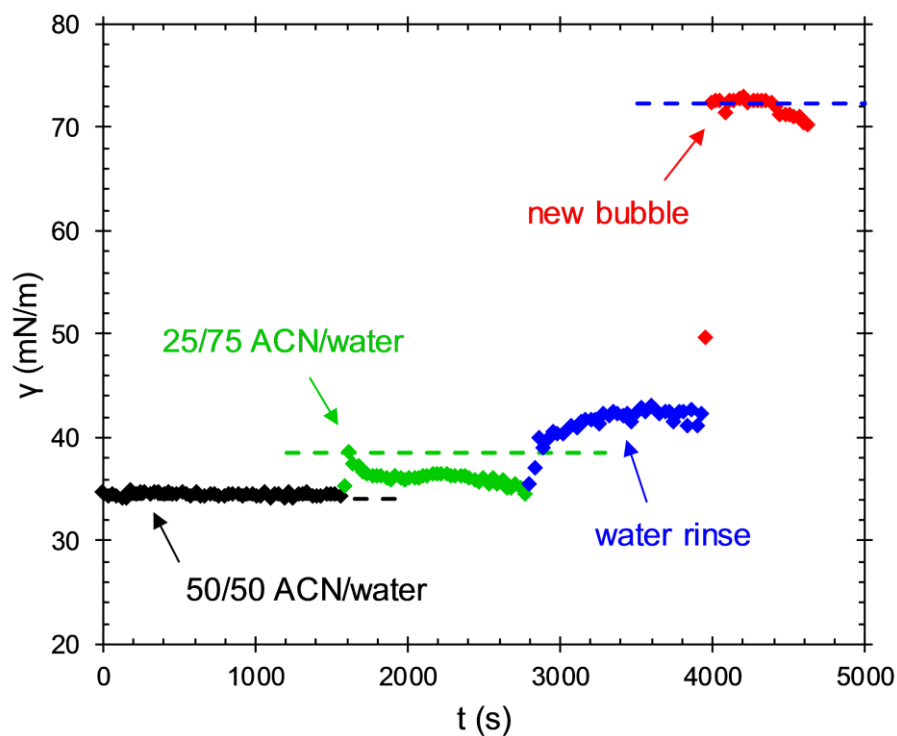
Figure 4.3. Dynamic surface tension of an air/liquid interface during exposure to 0.1 mM P_{IT} in 50/50 ACN/water (◆), after dilution of the P_{IT} solution to 0.05 mM in 25/75 ACN/water (◆), during continuous exchange of the P_{IT} solution with water (◆) and of a fresh interface formed in the exchanged reservoir (◆). The dashed lines denote the clean surface tension of the solvent mixtures without P_{IT}.

mixture. At $t = 2800$ s, the 0.05 mM P_{IT} solution is exchanged continuously with water ($\tau_R = 10$ s, $V = 3$ mL) until $t = 3800$ s where flow is ceased for an additional 200 s (blue diamonds). For the beginning of the rinse, the reservoir solution becomes cloudy with visible, microscopic aggregates before eventually clarifying. Surface tension increases sharply from the pre-rinse value of 35 mN/m ($t = 2800$ s) and eventually plateaus near $\gamma = 42$ mN/m. At this point, ACN has been removed from the reservoir, and the equilibrium surface tension of the reservoir solution (water) is 72 mN/m, given by the dashed blue line. The after-rinse plateau value of $\gamma = 42$ mN/m is significantly lower than the surface tension of pure water ($\gamma = 72$

mN/m), demonstrating that P_{IT} has formed a strongly, irreversibly adsorbed layer on the interface. At $t = 4000$ s, the existing interface is blown off to create a fresh, test interface (red diamonds). This is done to determine if any P_{IT} remains in the reservoir after rinsing. Surface tension of the test interface coincides with the clean value of pure water for approximately 400 s before beginning to drift downwards, signifying some adsorption. After aging for 600 s, the test interface reaches a surface tension near 70 mN/m. While the rinse did not remove all surface-active material from the bulk, the slow adsorption and modest surface tension ($\gamma = 70$ mN/m) of the test interface greatly contrasts with the substantially lower, after-rinse value ($\gamma = 42$ mN/m), demonstrating that the plateau in surface tension during the water rinse results from irreversibly adsorbed P_{IT} rather than a new equilibrium with a diluted bulk solution.

Figure 4.3 shows that P_{IT} can be used to create processible interfaces. Adsorption is driven by solvent quality—a 0.1 mM solution in a better solvent (50/50 ACN/water) shows no adsorption whereas a more dilute, 0.05 mM solution in a worse solvent (25/75 ACN/water) does show adsorption. When the P_{IT} solution is exchanged with a nonsolvent, water, surface tension plateaus to 42 mN/m, a value much lower than the clean value of 72 mN/m. While it is certain from the results of the test interface that this plateau signifies irreversibly adsorbed P_{IT}, it is unclear whether the interface after rinsing is exclusively comprised of P_{IT} present before rinsing or whether the precipitous decline in solvent quality stimulates additional adsorption beyond what is seen from the 25/75 mixture. Given that P_{IT} adsorbs
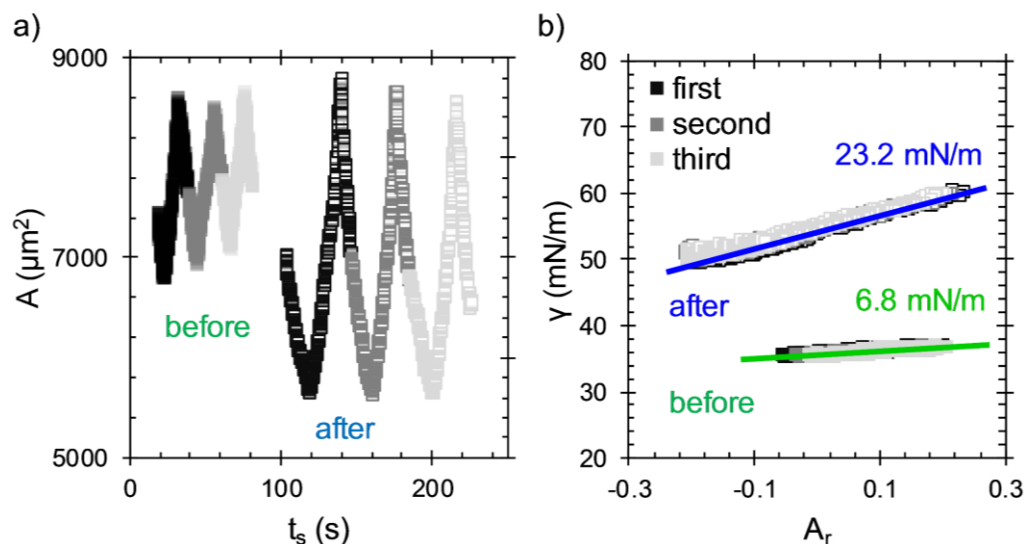
Figure 4.4. Surface area (a) and surface tension (b) during large amplitude compression before (filled points) and after rinse with water (empty points) of P_T-laden interfaces. Values of Ec calculated from these data are given in (b).

only modestly from the 25/75 mixture but remains strongly adsorbed after the rinse, the latter explanation is likely to be correct.

All subsequent experiments are carried out in a similar way to the one shown in Figure 4.3. An air/solution interfaces is first equilibrated against a 0.1 mM polypeptoid solution in a 25/75 ACN/water mixture (poor solvent) for 1000 s. The equilibrated interface is then rinsed with water ($\tau_R = 10$ s, $V = 3$ mL) for 1000 s and rested without flow for 200 s. The interface is then jettisoned to produce a fresh interface, used to test the composition of the reservoir after the rinse. Both before and after rinse, dilatational and compression moduli are measured.

Figure 4.4 shows the large-amplitude compressions of an interface with adsorbed P_T before and after rinse. Figure 4.4a shows interfacial area during the compression cycles. The points have been shifted along the x-axis to show conveniently data before (filled points) and after (empty points), now plotted

against shifted time, *ts*, on the same axes. Interfacial compression and expansion occur at a rate of 50 μm^2/s. Each interface is compressed/expanded three times with the first, second and third compressions given by the black, dark gray and light gray points, respectively. The smaller amplitude of before-rinse compressions is an experimental artifact. The capillary hydrophobization required to achieve suitable pinning of an air/water interface performs less well with ACN/water mixtures, and larger amplitudes than those shown cause the air/solution/glass contact line to shift during compression, invalidating the measurement.

Figure 4.4b shows the variation of surface tension during compression with nondimensionalized interfacial area, $A_r = (A-A_0)/A_0$, calculated by normalizing area by its value prior to compression, A_0. Both before and after rinse, the first, second and third cycles show no hysteresis. No hysteresis is observed for any of the compression cycles in this study, demonstrating that these interfaces are capable of recovering reversibly from large strains. Compression modulus can be read from the slopes of the data and is calculated by linear regression. The best fit lines and values for E_c are given in Figure 4.4b. Before rinse, E_c is low (6.8 mN/m) and increases with the rinse to a value of 23.2 mN/m. Compression modulus of all the polypeptoid-laden interfaces studied here increases with rinsing. E_c is a real quantity and does not by itself provide insight into the complex stress relaxation of the interface.

Figure 4.5 shows the real (filled symbols) and imaginary (empty symbols) components of dilatational modulus for the interfaces shown in Figure 4.4. Before rinse (green symbols), both elastic and viscous moduli are small (< 10 mN/m) over
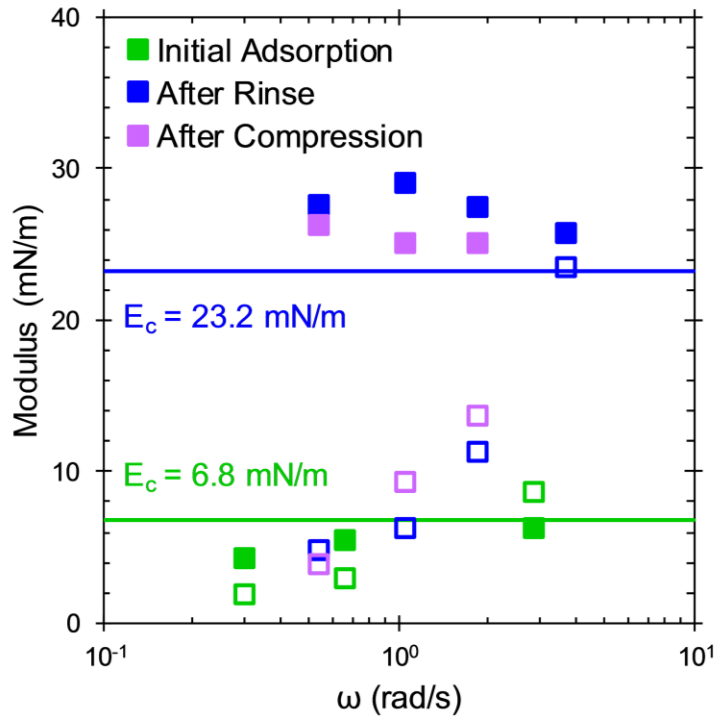
Figure 4.5. Elastic (■) and viscous (□) components of dilatational modulus after adsorption from 0.1 mM P_T in 25/75 ACN/water (■,□), after rinsing with water (■,□), and following the after-rinse large-amplitude compressions (■,□). The green and blue lines give values of compressional modulus before and after rinse, respectively, provided in Figure 4.4b.

the range of frequencies used, $0.3 < \omega < 3$ rad/s. Both moduli show a negligible dependence on frequency, and both have values near the compression modulus (green line), $E_c = 6.8$ mN/m. After rinse (blue symbols), the elastic modulus is substantially larger than before the rinse and depends little on frequency, $E' = 28 \pm 2$ mN/m. Viscous modulus after rinse increases with increasing frequency, at low frequencies near the pre-rinse values, $E''(\omega = 0.55$ rad/s$) = 5$ mN/m, and at high frequencies near that of the elastic modulus, $E''(\omega = 4$ rad/s$) = 27$ mN/m. After rinse, the value of elastic modulus is close to the compression modulus, and the viscous modulus is less then E_c at all but the largest frequency, $\omega = 4$ rad/s.

Dilatational modulus is measured in the small-amplitude, or linear, limit prior to the compressions shown in Figure 4.4. To check that the measurement of compression modulus is not itself processing the interface and changing its stress response, dilatational modulus has been again measured after rinse, after the large-amplitude compressions. The purple points in Figure 4.5 show good quantitative agreement with the after-rinse data prior to compressions (blue points), showing that the effects of the large-amplitude (and possibly nonlinear) compressions used to measure E_c do not linger beyond the measurement. This is consistent with the lack of hysteresis observed in Figure 4.4 and with the small values of viscous modulus at low frequencies in Figure 4.5. Viscous contributions at low frequencies are quite small, resulting in an in-phase stress response at all but the highest frequencies probed.

A comparison between elastic and compression moduli is provided in Figure 4.6. Agreement between E_c and E' across all frequencies suggests that dilatational stresses are not relaxed by material exchange with the interface during oscillation. Many small-molecule surfactants adsorb reversibly and are capable of exchange with the adjacent solution during interfacial compression/expansion, often with a rate limited by diffusion.[18–20] Exchange acts both to lower the measured value of dilatational modulus and to push the stress response to one dominated by the out-of-phase, viscous component. Instead, elastic modulus is constant across all frequencies, dominates at low frequencies and coincides with the compression modulus (the low frequency limit), contrasting with an explanation of relaxation by diffusional exchange which would suppress the elastic response at
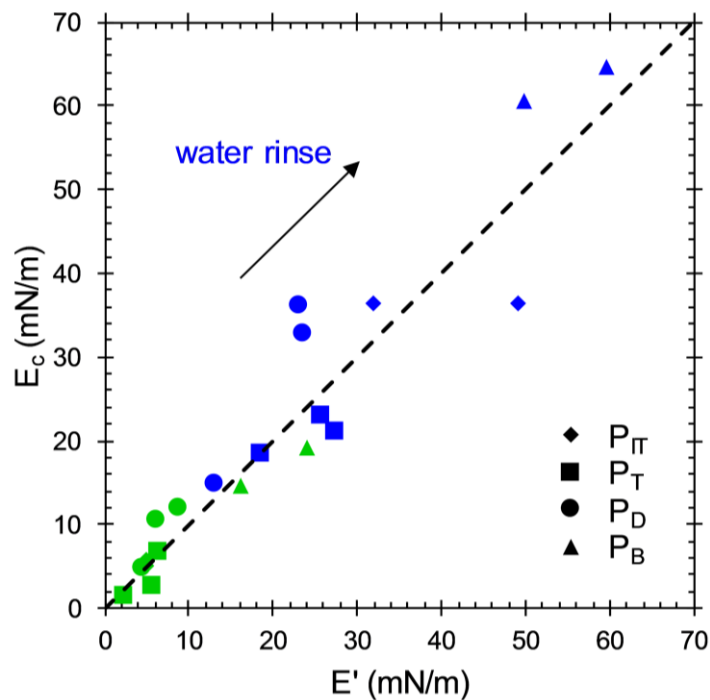
Figure 4.6. Comparison of compression modulus and elastic modulus at 1 rad/s after adsorption from a 0.1 mM solution in 25/75 ACN/water (green) and after water rinse (blue). The dashed line is a guide for the eye, representing perfect agreement.

lower frequencies. It is not surprising that the after-rinse moduli do not point towards material exchange given that water is a nonsolvent for these polypeptoids. The data show that the viscous modulus contributes more significantly at higher frequencies, a response that is not predicted by models of diffusional exchange. These dilatational data would be better described by a constitutive model focused on the interface.[21,22]

Figure 4.6 shows surface tension (a) and elastic modulus at 1 rad/s (b) for all four sequences before (solid) and after rinse (gray) with error bars providing standard deviations across the three replicates. Before-and-after values of surface tension do not show any significant differences among sequences. Each polypeptoid adsorbs modestly from an initial 0.01 mM solution in 25/75
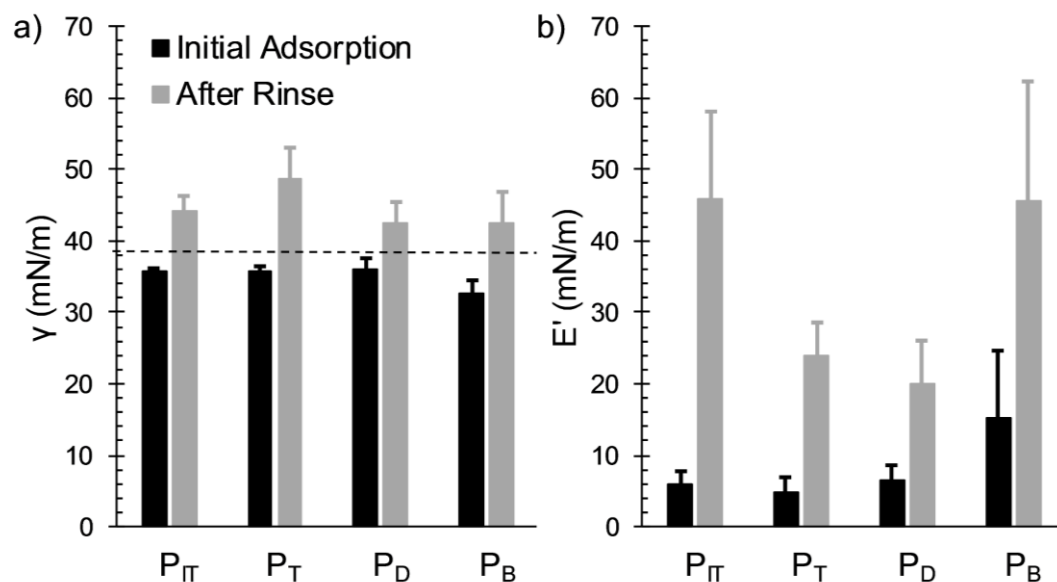
Figure 4.7. Surface tension (a) and elastic modulus at 1 rad/s (b) after initial adsorption from a 0.1 mM polypeptoid solution in 25/75 ACN/water (black) and after water rinse (gray). Error bars are standard deviations from three measurements.

ACN/water. The dashed line gives the equilibrium surface tension of the solvent mixture without polypeptoid. Exchanging the polypeptoid solution with water causes surface tension to increase by ~10 mN/m to a final value well below the surface tension of pure water, 72 mN/m.

Figure 4.6b shows the elastic modulus at 1 rad/s for polypeptoid-laden interfaces before and after rinse. Before rinse, the elastic modulus of all sequences is small, $E' < 20$ mN/m. Elastic modulus increases with rinsing with values up to 60 mN/m. The after-rinse values of elastic modulus show a sequence dependence. Both the inverse taper and blocky sequences have higher after-rinse moduli than the tapered and distributed sequences with the inverse tapered and distributed moduli having a statistically significant difference ($p < 0.05$). The increase in elastic modulus with rinsing is not correlated with the increase in surface tension beyond the general, positive trend. It is difficult to find the origin of the differences

among after-rinse moduli without a direct measurement of the adsorbed layers (e.g., ellipsometry or neutron reflectometry); however, some headway can be made by looking to adsorption in similar systems.

A surface equation of state relates the amount of adsorbed material to an interface (surface excess concentration) and the energy of the interface (surface tension).[23] Typically, surface tension is measured at many solution concentrations for a single surfactant and used to determine both an equation of state and an adsorption isotherm, relating surface excess and solution concentration. For most equations of state, surface tension monotonically decreases with increasing surface excess, meaning that a measurement of surface tension is also a measurement of surface excess concentration. Given the similarity in before-rinse values of surface tension shown in Figure 6a all at the same solution concentration, it is not unreasonable to assume that these four sequences have similar equations of state in the 25/75 ACN/water mixture. Exchanging the solvent mixture with water increases surface tension similarly for the four sequences, suggesting that the same is true in water. As mentioned in the discussion of Figure 4.3, it is likely that the amount of adsorbed polypeptoid after rinse is greater than that before rinse; however, the "bonus" adsorption appears to be similar across sequences. Assuming that before-rinse adsorption and additional adsorption during the rinse are the same for all sequences requires that the after-rinse surface excess concentration also to be the same.

After-rinse dilatational elasticity varies with sequence, with P_{IT} and P_B having the largest values. Assuming that surface concentrations are comparable,

then the difference in dilatational stress response must be explained by specific intermolecular interactions rather than by the number of interacting molecules (if surface concentration varied). The intermolecular interactions between adsorbed molecules will depend on sequence and orientation. P_B has a larger after-rinse modulus than P_D, although both have hydrophobic groups somewhat distributed along the chain. Because the hydrophobic groups of P_B are grouped in threes, P_B is likely to adopt a flatter conformation at the interface than P_D. In other words, thermal energy is more likely to pull a single phenyl ring into the water than three. As a result of the flatter conformation, a single P_B molecule would occupy more space, increasing the likelihood of interaction between neighboring chains via hydrophobic interactions (e.g., π-π stacking).[24]

P_{IT} should adopt a flatter conformation than P_T for similar reasons. The hydrophobic groups of P_T are tapered in a way that resemble a traditional one-tailed surfactant or a diblock copolymer whereas the hydrophobic groups of P_{IT} are biased towards the center of the chain in a way that resembles an asymmetric, ABA triblock copolymer (where block A is soluble and B is selective). An ABA triblock copolymer occupies more space at an interface than a diblock copolymer by a phenomenon known as dangling tails.[25] Essentially, a triblock copolymer of the same mass as a diblock packs less efficiently because the diblock can more easily form a brush in the solvent, lowering the size of its adsorption site. For the same number of adsorbed molecules, P_{IT} would lie flatter than P_T and have stronger intermolecular interactions because of it.

4.4 SUMMARY

Solvent quality controls the adsorption of amphiphilic polypeptoids. The four sequences studied here are not surface active in a good solvent, a 50/50 mixture of ACN/water, but they do adsorb modestly (lower γ by ~5 mN/m) to the air/liquid interface from a 0.1 mM solution in a poor solvent, 25/75 ACN/water. After adsorption, exchange of the polypeptoid solution with pure water strands the molecules at the interface; surface tension increases slightly but remains ~30 mN/m below the clean value of air/water, 72 mN/m. The small dilatational elasticity before the water rinse ($E' < 20$ mN/m) increases by at least a factor of two with the exchange, up to 60 mN/m. Agreement between the values of elastic and compression moduli suggests that material exchange between the interface and the solution is not responsible for relaxing dilatational stresses. The values of after-rinse elastic modulus show a dependence on molecular sequence with P_{IT} and P_B forming more elastic interfaces than P_T and P_D. It is likely that the P_{IT} and P_B sequences adopt flatter conformations at the interface, enabling their hydrophobic groups to interact more strongly than those of P_T and P_D.

(1)   Puvvada, S.; Blankschtein, D. *J. Chem. Phys.* **1990**, *92* (6), 3710–3724.

(2)   Srinivasan, V.; Blankschtein, D. *Langmuir* **2003**, *19* (8), 9932–9945.

(3)   Srinivasan, V.; Blankschtein, D. *Langmuir* **2003**, *19* (8), 9946–9961.

(4)   Alexandridis, P.; Olsson, U.; Lindman, B. *J. Phys. Chem.* **1996**, *100* (1), 280–288.

(5)   Israelachvili, J. N.; Mitchell, D. J.; Ninham, B. W. *J. Chem. Soc. Faraday Trans. 2 Mol. Chem. Phys.* **1976**, *72*, 1525–1568.

(6)   Mazer, N.; Benedek, G.; Carey, M. *J. Phys. Chem.* **1976**, *80* (7), 1075–1085.

(7)   Griffin, W. *J Soc Cosmet. Chem.* **1946**, 311–326.

(8)   Eastoe, J.; Dalton, J. . *Adv. Colloid Interface Sci.* **2000**, *85* (2–3), 103–144.

(9)   Fainerman, V. B.; Miller, R.; Ferri, J. K.; Watzke, H.; Leser, M. E.; Michel, M. *Adv. Colloid Interface Sci.* **2006**, *123–126* (SPEC. ISS.), 163–171.

(10)   Reichert, M. D.; Walker, L. M. *J. Colloid Interface Sci.* **2015**, *449*, 480–487.

(11)   Kirby, S. M.; Anna, S. L.; Walker, L. M. *Langmuir* **2015**, *31* (14), 4063–4071.

(12)   Davidson, M. L.; Walker, L. M. *Langmuir* **2018**, *34* (43), 12906–12913.

(13)   Kirby, S. M.; Anna, S. L.; Walker, L. M. *Soft Matter* **2017**, *14* (1), 112–123.

(14)   Zuckermann, R. N.; Kerr, J. M.; Moosf, W. H.; Kent, S. B. H. *J. Am. Chem. Soc.* **1992**, *114* (26), 10646–10647.

(15)   Patterson, A. L.; Danielsen, S. P. O.; Yu, B.; Davidson, E. C.; Fredrickson, G. H.; Segalman, R. A. *Macromolecules* **2019**, *52* (3), 1277–1286.

(16)   Oh, J.; Park, S. *J. Chem. Eng. Data* **1997**, *20* (8), 517–522.

(17)   Tahery, R.; Modarress, H.; Satherley, J. *J. Chem. Eng. Data* **2006**, *51* (3), 1039–1042.

(18)   Lucassen, J.; Van Den Tempel, M. *Chem. Eng. Sci.* **1972**, *27* (6), 1283–1291.

(19)   Joos, P. *Dynamic Surface Phenomenon*; Fainerman, V., Loglio, G., Lucassen-Reynders, E. H., Petrov, P., Miller, R., Eds.; VSP BP: The Netherlands, 1999.

(20)   Lucassen-Reynders, E. H.; Cagna, A.; Lucassen, J. *Colloids Surfaces A Physicochem. Eng. Asp.* **2001**, *186* (1–2), 63–72.

(21)   Scriven, L. E. *Chem. Eng. Sci.* **1960**, *12* (2), 98–108.

(22)   Kotula, A. P.; Anna, S. L. *J. Rheol. (N. Y. N. Y).* **2015**, *59* (1), 85–117
.
(23)   Berg, J. C. *An Introduction to Interfaces and Colloids: The Bridge to Nanoscience*; World Scientific Publishing Co. Pte. Ltd.: Danvers, 2010.

(24)   Hunter, C. A.; Sanders, J. K. M. *J. Am. Chem. Soc.* **1990**, *112* (14), 5525–5534.

(25)   Evers, O.; Scheutjens, J.; Fleer, G. *J. Chem. Soc. Farad. Trans.* **1990**, *86* (9), 1333–1340.

CHAPTER 5

PROCESSING IRREVERSIBLY ADSORBED, SOLVENT-RESPONSIVE NANOPARTICLES AT THE OIL/WATER INTERFACE

5.1 INTRODUCTION

Steric stabilization of nanoparticles often involves grafting polymers to the nanoparticle surface. At short interparticle distances, solvent-swollen polymer brushes provide the repulsive forces necessary to arrest particle aggregation. In aqueous systems, poly(ethylene oxide) (PEO) has been a popular choice for studying interparticle interactions of sterically stabilized particles because of the ability of certain Hofmeister salts to affect the water solubility of the PEO chain.[1] For example, Na_2CO_3 and Na_2SO_4 beyond a critical concentration will "salt out" free PEO chains from solution while NaCl will not. More salting-out electrolyte is needed as PEO molecular weight decreases.[2,3] Grafted PEO chains on the surface of nanoparticles share a similar sensitivity to salting-out electrolytes, and PEO-grafted nanoparticles have been shown to form strongly bound aggregates above a critical concentration of electrolyte.[4]

PEO-coated nanoparticles have been shown to be surface active at fluid interfaces.[5–8] This is not surprising given the well-documented surface activity of PEO homopolymers.[9,10] Suspensions of PEO-coated gold nanoparticles showed increased adsorption with higher concentrations of K_2CO_3 and form liquid-like structures above a critical salt concentration at air/water interfaces.[5] PEO-coated fluoroparticles have been shown to possess salt-responsive adsorption to toluene/water interfaces using Na_2CO_3 and Na_2SO_4. Measurements with small-angle neutron scattering show the PEO corona to collapse by 0.5 nm (from 2.3 to

1.8 nm) at 0.6 M Na_2CO_3 for the suspended particles. In both systems, increasing the concentration of salting-out electrolyte worsens the solvent quality for the grafted PEO, lowering interfacial tension beyond that seen for a neat suspension without electrolyte.

A key feature of the experiments discussed thus far is that nanoparticle adsorption has been measured from suspensions with varying amounts of salting-out electrolyte. Prior to the interfacial measurements, electrolyte has been added to stable suspensions, allowing the PEO chains to equilibrate with the electrolyte solution. The suspensions are then redispersed if necessary and contacted with the interface. Jonsson *et al.* (manuscript in preparation) have shown that the interfacial tension dynamics of PEO-coated fluoroparticles are faster (and adsorb to lower values) for suspensions with more Na_2CO_3; however, it is unclear from these measurements whether the additional lowering in interfacial tension below the no-salt case is due to changing the wetting of the particles or increasing the number of adsorbed particles.

This chapter focuses on the salt-responsiveness of adsorbed PEO-coated particles in a way that deconvolutes the enhanced driving force for adsorption of an unstable suspension from changes in interparticle interactions at the interface. By adsorbing particles to an oil/water interface from a suspension without electrolyte and washing out particles from the bulk that do not adsorb, it is possible to produce a persistent, particle-laden interface that can be processed with salting-out electrolyte. Changes in interfacial tension and dilatational mechanics are then

representative of interfacial forces rather than the aggregation of an unstable suspension in the bulk.

5.2 MATERIALS AND METHODS

The PEO-coated fluoroparticles used here have been prepared by surfactant-free synthesis described in detail elsewhere.[11] The core-shell particles are composed of a poly(2,2,3,3,4,4,4-heptafluorobutyl methacrylate) (PHFBMA) core and thin poly(ethylene oxide) (PEO) shell. The core radius and polydispersity are 96 Å and 5.5%, respectively. The brush region is composed of 2000 g/mol PEO homopolymer and has a thickness of 2.3 nm in water. Particle suspensions were first dialyzed using Por/Spectra RC tubing (1000 kg/mol cutoff) purchased from Repligen. 3 mL of 1 wt % suspension was dialyzed against 500 mL of water, and the dialysate was replaced daily. Dialysis is necessary to remove ungrafted PEO homopolymers that remain after particle synthesis.

Sodium sulfate (Na_2SO_4) was purchased from Sigma and baked for 6 h at 450 °C to remove hydrates and impurities. Aromatic 200 was used as received from ExxonMobil. Deionized water, referred to as water, with a resistivity of 18.2 MΩ·cm was produced using a Barnstead Ultrapure water filtration system. Solutions were prepared in acid-washed vials.

Interfacial properties have been measured with a microtensiometer platform, described in detail in Section 1.2. All interfaces in this chapter are made between an aqueous reservoir and oil-filled, hydrophobized capillary. The equilibrium interfacial tension between water and Aromatic 200 has been measured to be 42.1 mN/m initially with a value of 38.7 mN/m after 1 h, suggesting some

adsorption of surface-active impurities from within the oil. Concentrated electrolyte, 0.9 M Na_2SO_4, does not noticeably affect interfacial tension by itself with initial and 1 h values of 41.8 and 39.5 mN/m, respectively.

5.3 RESULTS

Figure 5.1 shows the interfacial tension throughout sequential processing of an aromatic 200/water interface that has been initially exposed to a 0.1 wt % suspension of particles. A fresh interface is produced at $t = 0$ and interfacial tension begins to decrease immediately (●) from the clean value (42 mN/m) given by the dashed line. This interface is preserved throughout the processing. Within 1200 s, interfacial tension has reached steady state near 22 mN/m. The interface is then subjected to small-amplitude oscillations and large-amplitude compressions, shown by the wider band of points beginning at 1200 s. The particle suspension is then rinsed out with 100 mL of pure water (without particles) over 600 s (○). Interfacial tension increases slightly during the rinse. The interface is again tested by small- and large-amplitude means. Near 2600 s, the interface is exposed to the first of three solutions of Na_2SO_4 (without particles) of increasing concentration (0.3 M ■, 0.6 M ◆ and 0.9 M ▲)—all steps involve the exchange of 100 mL of solution over 600 s, separated by small- and large-amplitude dilations. During exposure to the salt solutions, interfacial tension drifts downwards slightly to a final value near 21 mN/m. At 5500 s, the 0.9 M Na_2SO_4 solution is exchanged with 100 mL of water (without particles) over 600 s and against tested with small and large-amplitude dilations (△). Interfacial tension increases to a value near 22.5 mN/m. Without changing the reservoir solution, a fresh interface is created to test the composition
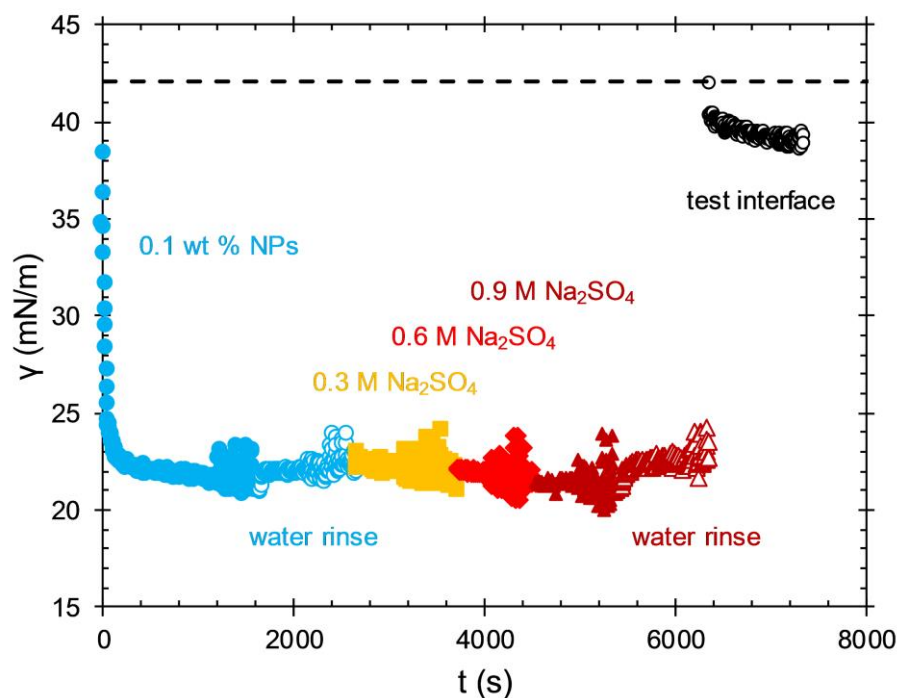
Figure 5.1. Sequential processing of an aromatic 200/water interface: initial adsorption from a suspension of 0.1 wt % nanoparticles (NPs) in water (●), rinse with water (○), rinse with Na_2SO_4 solutions (0.3 M ■, 0.6 M ◆ and 0.9 M ▲), rinse with water (△) and creation of a new interface to test reservoir conditions (○). 100 mL of new solution is exchanged in each step over 600 s followed by small-amplitude oscillations and large-amplitude compressions.

of the reservoir (○). The interfacial tension of the test interface begins at the clean

value and decreases by 3 mN/m over 1000 s to a value near 39 mN/m, showing that

the reservoir is mostly free from surface active material.

Clearly these particles adsorb strongly and irreversibly at the aromatic

200/water interface.   Adsorption happens quickly from a stable 0.1 wt %

suspension. Interfacial tension changes little throughout processing, showing that

the particles that adsorb initially remain at the interface even as particles are

removed from the bulk. It is not surprising that interfacial tension remains low as

water is replaced with electrolyte—increasing Na_2SO_4 concentration lowers the

solvent quality in the bulk for the PEO-coated particles.[1,12] The slight drift downwards during processing with electrolyte may be due to adsorption of surface active impurities or surface rearrangements in the oil as similar drift has been observed at higher interfacial tensions for bare aromatic 200/water interfaces beyond an hour. Given the worsening solvent conditions in the bulk for the particles and decreasing interfacial tension, these phenomena are not likely to displace adsorbed particles from the interface. The final exchange with water does see an increase in interfacial tension beyond that seen during the first water rinse, suggesting that some may desorb here. Any desorption would be slight as can be seen by the early plateau near 5700 s. While Figure 5.1 shows that these particles adsorb irreversibly, the measurement of interfacial tension alone does not provide enough information to describe the response of the particle-laden interfaces throughout processing.

Figure 5.2 shows the result of large-amplitude compressions for the interface shown in Figure 5.1 following the first exchange with water (a) and processing with 0.3 M (b), 0.6 M (c) and 0.9 M (d) Na_2SO_4. Each subplot shows the results of three compression cycles: first (○), second (□) and third (△). There is no distinguishable difference either in compression or expansion or among any of the three cycles. Compression cycles have similar initial interfacial area, A_0, near 6000 μm^2 and begin with compression followed by expansion. Interfacial tension decreases during compression and increases during expansion. For irreversibly adsorbed particles, this corresponds to an increase in surface coverage as the interface compresses unmitigated by relaxation provided by exchange of
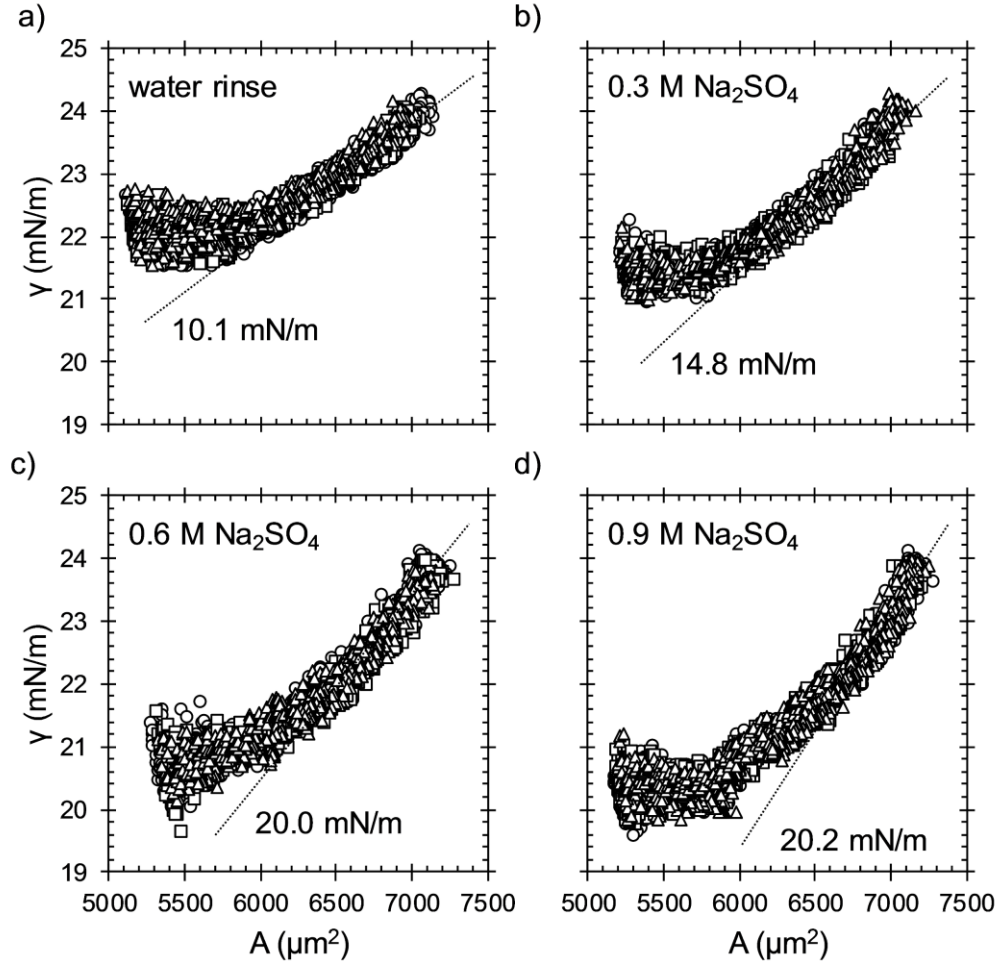
Figure 5.2. Large-amplitude compression of a particle-laden interface after rinsing with water (a), 0.3 M Na$_2$SO$_4$ (b), 0.6 M Na$_2$SO$_4$ (c) and 0.9 M Na$_2$SO$_4$ (d). Three compression cycles are shown for each interface: first ($\bigcirc$), second ($\square$) and third ($\triangle$). The value of compression modulus, E_c, calculated from large-A data is given on each plot next to the dotted line. Data are from Figure 5.1.

material between the interface and the bulk. The compression modulus, E_c, at lower coverages (higher γ) is given in each of the subplots and provided by the dotted lines. E_c increases with electrolyte concentration with most of the increase occurring from 0 to 0.6 M Na$_2$SO$_4$. At smaller areas, the rate of change of interfacial tension decreases. The cycles trend to lower interfacial tensions as
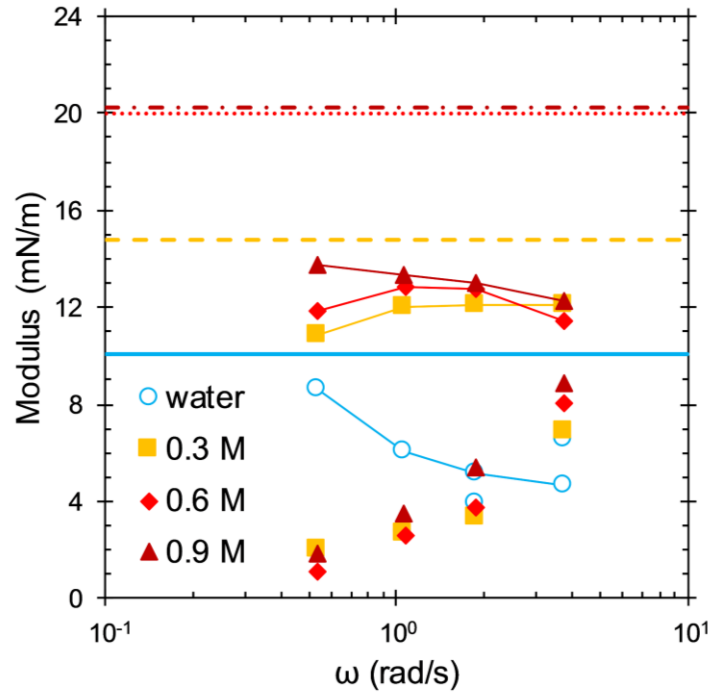
Figure 5.3. Frequency-dependence of real (E', connected symbols) and imaginary (E'', symbols only) components of dilatational modulus after processing a particle-laden interface with water (○) and Na_2SO_4 (0.3 M ■, 0.6 M ◆ and 0.9 M ▲). The solid, dashed, dotted and dash-dotted lines correspond with values of E_c after processing with water, 0.3 M, 0.6 M and 0.9 M Na_2SO_4, respectively. These dilatational measurements were taken just prior to the large-amplitude results shown in Figure 5.2.

electrolyte increases, representative of the slight drift downwards of interfacial tension shown in Figure 5.1.

Small-amplitude oscillations serve to compliment large-amplitude compressions as they sample a frequency-dependent stress response in the linear limit. Figure 5.3 shows the elastic (E', connected symbols) and viscous (E'', symbols only) contributions to dilatational modulus for the interfaces shown in Figure 5.2. Measurements were taken at $A = 6000$ μm^2 prior to large-amplitude compressions. Both E' and E'' are small throughout processing. Elastic modulus increases once the interface is exposed to 0.3 M Na_2SO_4 and increases little with

increasing electrolyte. Viscous modulus does not change throughout the processing and increases with increasing frequency. Shown by the lines, E_c in each step is greater than both E' and E'' (and $|E^*|$). This is indicative either of a dilation-thinning stress response or of the capture of higher-order effects (nonlinearities) by the large-amplitude test. Regardless, it is evident that the dilatational response is weakly elastic and that elasticity increases slightly with increasing bulk electrolyte.

While the nanoparticles adsorb irreversibly from a 0.1 wt % suspension in water, they do not exhibit a mechanical response that strongly depends on electrolyte concentration. It is likely that the suspension loading used in Figures 5.1-3 is too dilute to drive sufficient particles to the interface change the mechanical response. However, these particles have been shown to lower the interfacial tension of a toluene/water interface below 20 mN/m with a 1 wt % suspension. Instead of using a more concentrated suspension, the experiment shown in Figure 5.1-3 has been repeated by initially operating the microtensiometer in a pseudo-unstable fashion that is useful in promoting additional adsorption beyond what is possible by equilibration alone.

In the microtensiometer, interfaces larger than hemispherical caps ($R = R_c$) are inherently unstable. This is a consequence of the Laplace instability because the Laplace pressure provided by the capillary fluid is greater than the Laplace pressure necessary to satisfy the force balance at the interface (Laplace equation) even though the radius of curvature of an interface greater than a hemisphere will be the same as one with a radius of curvature small than a hemisphere.[13] For an air/liquid interface, air immediately jets from within the capillary once $\Delta P > 2\gamma/R_c$.
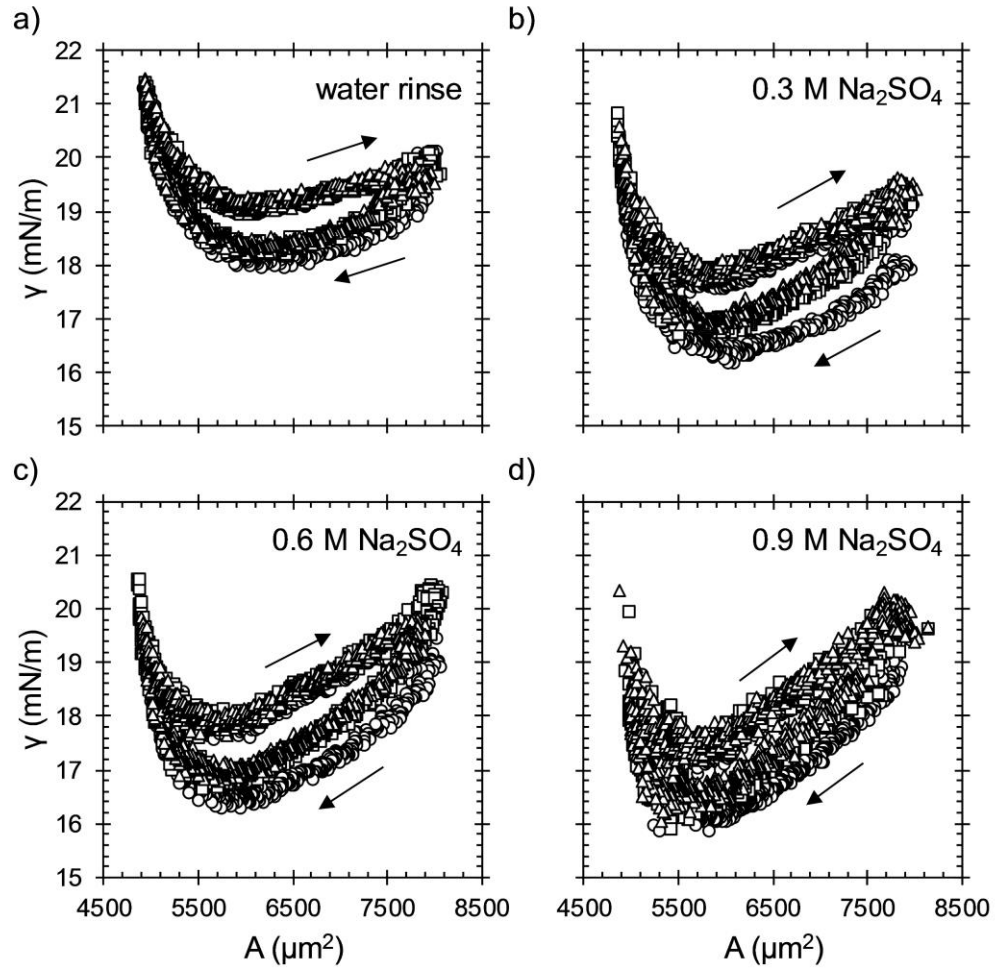
Figure 5.4. Large-amplitude compression of a particle-laden interface after rinsing with water (a), 0.3 M Na$_2$SO$_4$ (b), 0.6 M Na$_2$SO$_4$ (c) and 0.9 M Na$_2$SO$_4$ (d). Three compression cycles are shown for each interface: first (○), second (□) and third (△). These interfaces correspond to an experiment performed in the exact same way as that depicted by Figure 5.1 but to a lower initial interfacial tension from the particle suspension. Arrows denote the direction of the compression and expansion.

For an oil/water interface, the higher viscosity of the oil relative to that of air gives an unstable interface a lifetime of seconds, beyond which the Laplace pressure must be quickly decreased to avoid irreversible growth and subsequent loss of the interface. A larger-than-hemispherical oil/water interface possesses a larger interfacial area than the corresponding stable interface with the same radius of

curvature. For the irreversibly adsorbed particles used here, the larger interface can be equilibrated against the bulk and then compressed below R_c to produce an interface with a lower interfacial tension (higher surface coverage) than what is solely possible by equilibration of the smaller interface. Using this trick, the experiment shown in Figures 5.1-3 has been repeated at a lower initial interfacial tension with details provided in Table 5.1.

Figure 5.4 shows the large-amplitude compressions performed after processing adsorbed particles at an aromatic 200/water interface with 100 mL water (a) and 0.3 M (b), 0.6 M (c) and 0.9 M (d) Na_2SO_4. Each subplot shows the results of three compression cycles: first ($\bigcirc$), second ($\square$) and third ($\triangle$). The interface has an initial area, A_0, between 7740 and 7930 μm^2 (details in Table 5.1). Initially, interfacial tension decreases as the interface compresses until reaching a minimum value. Continued compression increases interfacial tension until the re-expansion, and the interfacial tension decreases again. During expansion, interfacial tension experiences a local minimum before increasing for the remainder of the expansion. The second minimum occurs at a noticeably higher value of interfacial tension and a slightly surface area. The second and third compression cycles show the same hysteresis and are distinguishable from the first compression by higher values of interfacial tension during the compression stage ($\square,\triangle$ points above $\bigcirc$). All three cycles are indistinguishable during expansion.

5.4 DISCUSSION

The compressions in Figure 5.4 differ from those shown in Figure 5.2 in several ways. First, the compressions in Figure 5.4 occur at lower interfacial

tensions than those shown in Figure 5.2 as a result of the aforementioned trick to stimulate additional adsorption of the particles. The second set of compressions also begin at higher initial interfacial areas ($\sim$ 7800 μm^2 vs $\sim$ 6000 μm^2). Not only is the surface coverage of particles initially greater in Figure 5.4, but the increase in surface coverage during the compression is also greater. In Figure 5.4, interfacial tension experiences two minima that differ along both axes and with bulk composition.

For small interfacial deformations, compression of surface-active species varies depends on adsorption strength. For an irreversibly adsorbed surfactant or particle, reducing interfacial area (increasing surface coverage) lowers interfacial tension according to that material's equation of state. For a reversibly adsorbed surfactant, the variation of interfacial tension during compression depends on the rate of exchange of the surfactant between the interface and the bulk.[14,15] If the compression happens faster than desorption, interfacial tension experiences an abrupt minimum before increasing to its value prior to compression.[16] If the compression happens at a similar timescale as desorption, interfacial tension experiences a less abrupt minimum, and the minimum occurs later than in the first case. Driven by material exchange between the interface and bulk, the stress relaxation is shifted out of phase with the deformation.

The interfacial stress response for large deformations is inherently more complicated due to the prevalence of higher-order effects. The compressions in Figure 5.4 show a time-dependent stress response. This is evident by the first compression cycle having a lower interfacial tension on compression than the
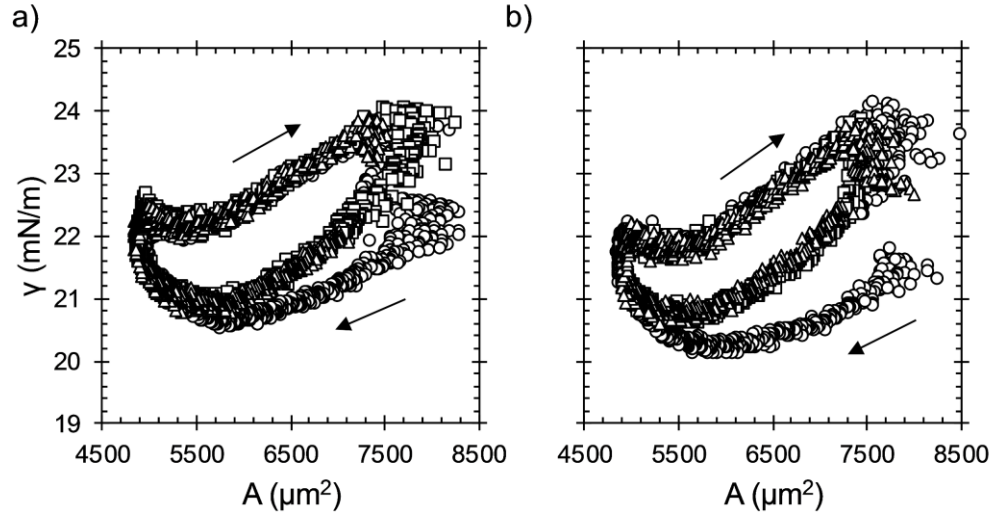
Figure 5.5. Large-amplitude compression of a particle-laden interface after rinsing with water: (a) immediately after cessation of water rinse and (b) 300 s after the compressions in (a). Three compression cycles are shown for each interface: first ($\bigcirc$), second ($\square$) and third ($\triangle$). Arrows denote the direction of the compression and expansion.

subsequent two. During the interfacial tension increase that happens during compression, the second and third cycles converge with the first. The timescale of this relaxation can be estimated by the time needed to complete a single compression cycle, 50 s. Figure 5.5 shows that waiting for 300 s (6 cycles) is enough to erase the memory of the previous compressions.

In the microtensiometer, interfacial stress is varied by changing the Laplace pressure rather than directly prescribing a change in interfacial area. As a result, a nonlinear interfacial tension response can be calculated by linear pressure and radius signals that are out of phase. In other words, the change in radius of curvature as a result of changing the Laplace pressure is beholden to the stress response of the interface. In fact, shifting the time-dependent radius by 25 s (1/2 cycle) for the data shown in Figure 5.4 restores the expected monotonic relationship

between the measured Laplace pressure and calculated interfacial tension—interfacial tension decreases with decreasing pressure and increases during expansion. This makes precise analysis of the shape of the compression cycles difficult. It is much easier to assess the impact of electrolyte on the large-amplitude stress response of the interface by comparison of a single point such as the area at which interfacial tension is at a minimum.

The minimum area decreases with increasing bulk electrolyte. Each compression is done with the same interface at the same compression rate (50 s/cycle), suggesting that the change in area is representative of an electrolyte-responsive process. At air/water interfaces, charged silica particles have been shown to experience hard-sphere repulsion at a critical surface coverage that can be varied by changing the concentration of bulk electrolyte.[17] It was assumed that the hard-sphere interparticle interactions occur at the same surface coverage independent of bulk electrolyte, meaning the particles that interact over larger distances (lower electrolyte, less charge screening) will reach that critical coverage with less compression than smaller particles (more electrolyte, greater charge screening). In a similar way, the areas of minimum interfacial tension are interpreted here to represent a critical coverage of particles necessary to facilitate the nonlinear response in Figure 5.4. These critical areas, A_c, are determined by calculating the regions of zero slope (γ vs $\Delta A/A_0$) during compression using a moving average over 3 s (45 points). Data points are considered to be within the minima if the magnitude of the local slope is less than 2 mN/m, the lower bound on the measurement of E with the microtensiometer.
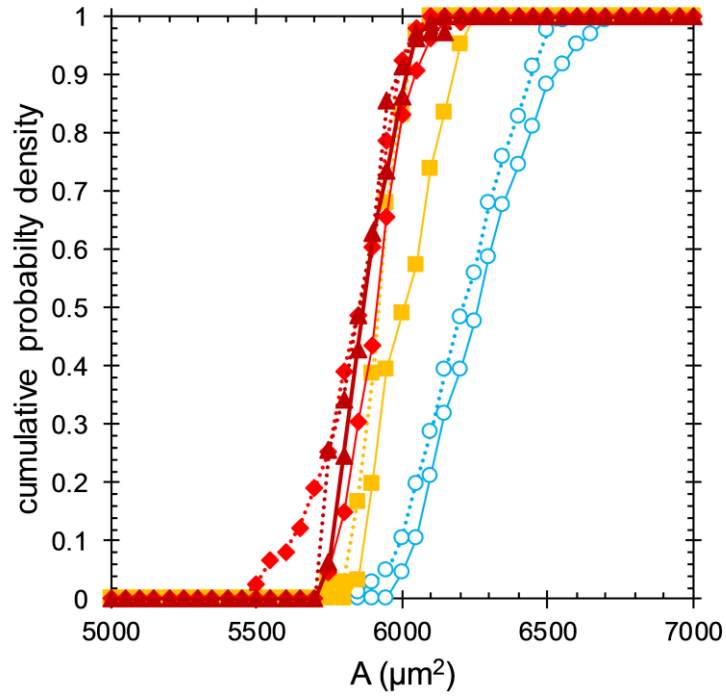
Figure 5.6. Cumulative probability density of minima of interfacial tension for large-amplitude compressions shown in Figure 5.4. Symbols correspond to processing with water (○) and Na_2SO_4 (0.3 M ■, 0.6 M ◆ and 0.9 M ▲) where solid and dotted lines connect symbols for minima during compression and expansion, respectively. Each curve represents the aggregated values for the first, second and third compressions or expansions.

Figure 5.6 shows the position of critical area for compression (solid lines) and expansion (dotted lines) as a cumulative probability density constructed with a bin size of 50 μm^2. This bin size was selected to be more than twice the uncertainty in the measurement of A, ± 10 μm^2, and large enough to provide sufficient sample sizes (~ 50 points). For example, the 6200 μm^2 bin contains all zero-slope points from 6151-6200 μm^2. Figure 5.6 highlights the two features visible in Figure 5.4— the critical area decreases with increasing electrolyte, and the critical area during expansion, A_c^{exp}, is lower than that during compression, A_c^{comp}. Table 5.1 lists

values of A_c read from Figure 5.6 at the midpoint, a cumulative probability density of 0.5.

The interfacial area occupied by adsorbed nanoparticles is described by Eq 5.1

$$N \cdot a_p = \phi_p \cdot A \qquad (5.1)$$

where N is the number of adsorbed particles, a_p is the area occupied by a single particle and ϕ_p is the surface coverage of adsorbed particles. If it is assumed that the interface experiences a minimum in interfacial tension at the same surface coverage and that particles do not desorb, then the shift in critical area measures a size change of the particles. Table 5.1 shows the quotient of the critical area during compression for the ith processing step with the critical area after the first water rinse, A_c^i/A_c^0. Using Eq 5.1, A_c^i/A_c^0 is converted into the change in area of an adsorbed particle and used to calculate its change in radius, Δr_p, assuming that particles are initially adsorbed at the maximum possible area corresponding with a particle radius of 98.3 nm.

Table 5.1. Comparison of results of large-amplitude compressions during interfacial processing with bulk measurements with SANS showing the collapse of the PEO corona. Compression data have been taken from Figures 5.4 and 5.6. SANS data were taken of equilibrated particles in a similar salt, Na_2CO_3.[18]

	γ_0 (mN/m)	A_0 (μm^2)	γ_{min} (mN/m)	A_c^{comp} (μm^2)	A_c^{exp} (μm^2)	A_c^i/A_c^0	Δr_p (nm)	δ_{PEO} (nm)
0.1 wt % NPs	17.7	7830	16.4	6250	6100			2.3
water	19.3	7780	18.0	6300	6250	1	0	2.3
0.3 M Na_2SO_4	18.0	7780	16.2	6050	5950	0.960	-2.0	2.3
0.6 M Na_2SO_4	19.1	7930	16.3	5950	5900	0.944	-2.8	1.8
0.9 M Na_2SO_4	18.9	7740	15.9	5900	5900	0.937	-3.2	1.8
water	19.3	7790	17.5	5950	5900	0.944	-2.8	2.3

From Table 5.1, the radius of the adsorbed particles decreases by a maximum of 3.2 nm with the most concentrated salt solution, 0.9 M Na_2SO_4. After the concentrated electrolyte has been replaced with water, particle radius does not restore to its value prior to processing with electrolyte, showing that this process is irreversible within the experimental timescale (~ 1000 s). This is consistent with a study showing that PEO-grafted particles form semi-permanent aggregates above a critical electrolyte concentration.[4] Table 5.1 also shows form factor fits for the thickness of the PEO corona from small-angle neutron scattering (SANS) of aged suspensions with varying concentrations of Na_2CO_3, an electrolyte with similar ability to salt out PEO.[18] SANS measurements show that the PEO layer collapses from 2.3 to 1.8 nm at 0.6 M Na_2CO_3. The calculated reduction in radius from Figure 5.4 is greater than the expected collapse, although within an order of magnitude and trending in the expected direction. It is possible that the decrease in solvent quality with increasing electrolyte also shifts the adsorbed particles towards the oil side of the interface, explaining the larger-than-expected reduction in particle size.

5.5 Summary

The interfacial properties of solvent-responsive, core-shell nanoparticles can be tuned with interfacial processing. Particles adsorb irreversibly to an oil/water interface from a neat suspension in pure water; interfacial tension (γ ~ 22 mN/m) and dilatational modulus (E'~ 10 mN/m) of the interface change negligibly as it is processed with pure water or increasing concentrations of Na_2SO_4. At lower surface coverages of the particles (larger γ), interfaces show compressional reversibility. At greater surface coverages (lower γ), large-

amplitude compressions result in a complex, nonlinear stress response. For the same interface, the extent of compression required to induce the nonlinear response increases with increasing electrolyte in the bulk. Assuming that this state occurs at the same critical surface coverage for all interfaces, the corresponding decrease in particle size due to the "salting out" of the polyethylene oxide shell lies in the same order of magnitude as data from small-angle neutron scattering. The adsorption irreversibility and salt-responsive mechanical response of these particles show that this system would be ideal to study interfacial, particle-particle interactions within the context of complex phenomena like wetting or coalescence.

(1)   Hey, M. J.; Jackson, D. P.; Yan, H. *Polymer (Guildf).* **2005**, *46* (8), 2567–2572.

(2)   Dumetz, A. C.; Lewus, R. A.; Lenhoff, A. M.; Kaler, E. W. *Langmuir* **2008**, *24* (18), 10345–10351.

(3)   Bleier, B. J.; Anna, S. L.; Walker, L. M. *J. Phys. Chem. B* **2018**, *122* (14), 4067–4076.

(4)   Jonsson, G. K.; Ulama, J.; Persson, R. A. X.; Oskolkova, M. Z.; Sztucki, M.; Narayanan, T.; Bergenholtz, J. *Langmuir* **2019**, *35* (36), 11836–11842.

(5)   Zhang, H.; Wang, W.; Mallapragada, S.; Travesset, A.; Vaknin, D. *Nanoscale* **2017**, *9* (1), 164–171.

(6)   Zhang, H.; Wang, W.; Akinc, M.; Mallapragada, S.; Travesset, A.; Vaknin, D. *Nanoscale* **2017**, *9* (25), 8710–8715.

(7)   Garbin, V.; Crocker, J. C.; Stebe, K. J. *J. Colloid Interface Sci.* **2012**, *387* (1), 1–11.

(8)   Zanini, M.; Isa, L. *J. Phys. Condens. Matter* **2016**, *28* (31).

(9)   Shuler, R. L.; Zisman, W. A. *J. Phys. Chem.* **1970**, *74* (7), 1523–1534.

(10)   Cao, B. H.; Kim, M. W. *Faraday Discuss.* **1994**, *98*, 245–252.

(11)   Ulama, J.; Zackrisson Oskolkova, M.; Bergenholtz, J. *J. Phys. Chem. B* **2014**, *118* (9), 2582–2588.

(12)   Taboada, M. E.; Asenjo, J. A.; Andrews, B. A. *Fluid Phase Equilib.* **2001**, *180* (1–2), 273–280.

(13)   Adamson, A.; Gast, A. *Physical Chemistry of Surfaces*, 6th ed.; Wiley-Interscience: New York, 1997.

(14)   Lucassen, J.; Van Den Tempel, M. *Chem. Eng. Sci.* **1972**, *27* (6), 1283–1291.

(15)   Joos, P. *Dynamic Surface Phenomenon*; Fainerman, V., Loglio, G., Lucassen-Reynders, E. H., Petrov, P., Miller, R., Eds.; VSP BP: The Netherlands, 1999.

(16)   Miller, R.; Joos, P.; Fainerman, V. B. *Adv. Colloid Interface Sci.* **1994**, *49* (C), 249–302.

(17)   Kirby, S. M.; Anna, S. L.; Walker, L. M. *Soft Matter* **2017**, *14* (1), 112–123.

(18)   Jonsson, G. K. Salting-out of Colloidal Latex Particles Grafted with Poly(ethylene glycol), University of Gothenberg, 2020.

CHAPTER 6

CONTROLLING SPONTANEOUS EMULSIFICATION AT THE OIL/WATER INTERFACE

6.1 INTRODUCTION

Emulsions are colloidal dispersions of two immiscible fluids stabilized by surfactants.[1,2] Most emulsions are metastable, formed by shearing two liquid phases with a surfactant, referred to as the emulsifier. The emulsifier plays a large role in emulsion stability, which can range from minutes for oil-and-vinegar salad dressing to years for some paints and personal care products. Emulsions have interesting rheological properties.[3,4] They often have apparent viscosities higher than either of their constituent fluids and are shear-thinning, exhibiting yield stresses at high volume fractions of the dispersed phase.[5] Emulsion processing (mixing, pumping, etc.) is further complicated by the nonequilibrium nature of the colloid. Handling an emulsion requires detailed knowledge of both stability and formation because of the extent by which the flow properties of an emulsion differ from those of the separate phases.

Spontaneous emulsification is the process by which emulsification occurs without addition of mechanical energy or the application of a thermal gradient.[6–9] For the purpose of this chapter, this definition does not include microemulsions which are equilibrium structures having sizes much smaller (< 10 nm) than most emulsion droplets (~ μm).[10] Beyond this simple definition, the phenomenon of spontaneous emulsification is poorly understood. Proposed mechanisms for spontaneous emulsification fall into one of two categories: mechanical instability at the interface by which droplets "pinch off" or by the nucleation and growth of
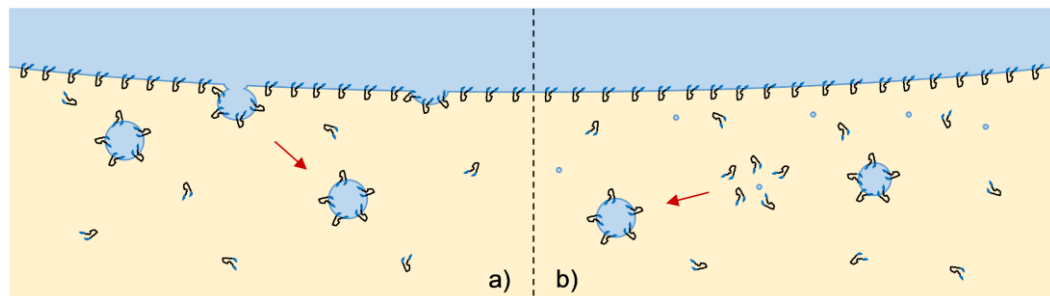
Figure 6.1. Candidate mechanisms of spontaneous emulsification. (a) Pinch off of micron-sized droplets directly from the oil/water interface facilitated by surfactant adsorption. (b) Growth of sub-microscopic nuclei into micron-sized droplets due to transport gradients of water and surfactant in oil.

droplets near the interface, shown in Figure 6.1. Examples of spontaneous emulsification by instability include interfacial turbulence at ultralow values of interfacial tension $(\gamma \ll 1 \text{ mN/m})$,[6] destabilization of oil/surfactant vesicles[11] and disintegration of long tubules of surfactant in the lamellar liquid crystalline phase.[12,13] In these systems, interfacial properties matter directly. Interfacial tension and mechanics directly impact the emulsification event because the droplet forms by pinch off from the larger interface.

Spontaneous emulsification by growth of small nuclei differs from the first mechanism because interfacial properties do not directly affect the emulsification. Instead, the interface provides a boundary condition near which gradients of emulsifier and liquid arise. The most notable examples of the second mechanism involve emulsifiers (often an alcohol) which are soluble in both fluid phases. This phenomenon, also known as diffusion and stranding[6] or as diffusion path theory,[14] occurs away from the interface with appreciable values of interfacial tension ($\gamma \sim$ 10 mN/m). Diffusion of the soluble emulsifier and trace solvent across the interface produce regions of local supersaturation in which emulsion droplets form by

spinodal decomposition. Using diffusion path theory, predictions have been made for the phenomenon by using a ternary phase diagram in combination with local concentration information from a simple, planar diffusion model. Phase diagrams have been successfully sued to predict spontaneous emulsification with so-called "Ouzo effect' systems.[15] This phenomenon is so named because of the ability of the Mediterranean alcoholic beverage ouzo (ethanol, water and anise oil) to spontaneously emulsify when diluted with water.

A shortcoming of existing models is that they cannot be easily extended to spontaneously emulsifying systems in which the emulsifier is a surfactant.[16,17] The existing descriptions of spontaneous emulsification focus on thermodynamics and ignore the role of surfactant in changing the properties of the oil/water interface. To understand spontaneous emulsification with surfactant emulsifiers, interfacial properties must be the focus. The work in this chapter demonstrates that the interface-focused approach provides the necessary tools to control spontaneous emulsification with oil-soluble surfactants using interfacial processing.

6.2 MATERIALS AND METHODS

N-dodecane (99%), referred to as dodecane, was purchased from Sigma and passed through serological pipettes packed with basic alumina powder to remove surface-active impurities. Deionized water, referred to as water, with a resistivity of 18.2 MΩ·cm was produced using a Barnstead Ultrapure water filtration system. Solutions were prepared in acid-washed vials. The water content of dodecane and dodecane solutions was determined by Karl Fischer titration using a Mettler-Toledo Titrator Compact C10SX. The lower limit of water detection is 15 ppm.
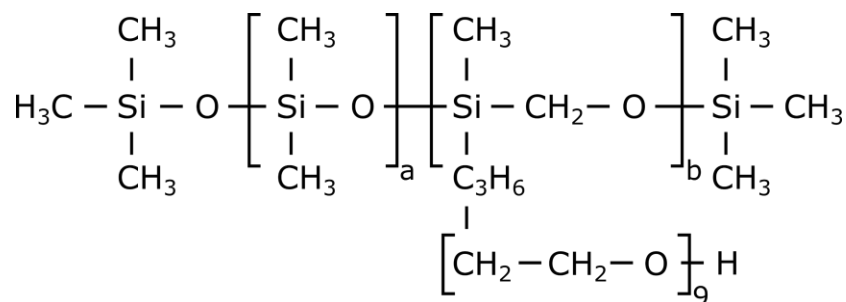
Figure 6.2. Molecular structure of the rake surfactant R-LL. Molecular weight is between 4000 and 15000 g/mol with unspecified monomer content *a* and *b*.

The diblock and triblock surfactants used here are identical to those described in detail in Section 2.2 with an addition, $E_{39}D_{240}$. $E_{39}D_{240}$ has been synthesized with a similar purity and monodispersity as those discussed for the other molecules in Table 2.1. The oil-soluble, silicone polyether (SPE) R-LL has been provided by Dow with a molecular weight range of $4000 - 15000$ g/mol.[18] An R-LL molecule resembles a rake, composed of a polydimethyl siloxane (PDMS) backbone with 9-unit oligomers of ethylene oxide (EO) at one end.

Spontaneously emulsifying dodecane/water interfaces have been imaged with a microtensiometer platform, described in detail in Section 1.2, in two extremes of interfacial curvature. Oil/water interfaces are defined to be concave for dodecane/surfactant within the capillary and convex for dodecane/surfactant within the reservoir. The equilibrium interfacial tension of dodecane/water is initially measured to be 52.5 mN/m and decreases by less than 1 mN/m in 1000 s without surfactant.

101

6.3 RESULTS

6.3.1 Observations with oil-soluble diblock and triblock copolymer amphiphiles
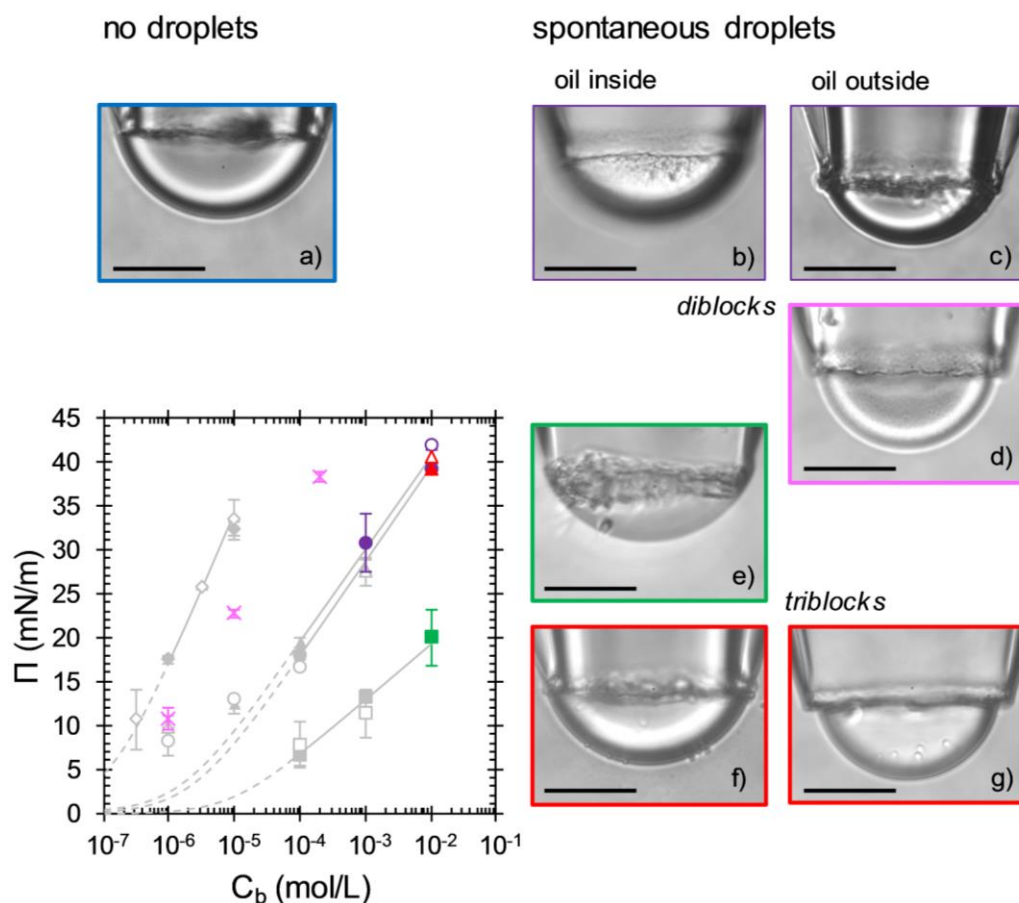
Figure 6.3. Spontaneous droplet formation with PEO-PDMS block copolymers used in Chapter 2. The plot is adapted from Figure 2.1 and shows steady-state adsorption for $E_{11}D_{80}$ ($\blacklozenge$,$\lozenge$), E_6D_{29} ($\bullet$,$\circ$), $E_{39}D_{240}$ ($\times$), $E_{11}D_{160}E_{11}$ ($\blacksquare$,$\square$) and $E_6D_{80}E_6$ ($\blacktriangle$,$\triangle$). Colored points correspond with spontaneous droplet formation. Images are of dodecane/water interfaces on the microtensiometer platform for (a) no droplets with $E_{11}D_{80}$ and spontaneous droplets with (b,c) E_6D_{29}, (d) $E_{39}D_{240}$, (e) $E_{11}D_{160}E_{11}$ and (f,g) $E_6D_{80}E_6$. The scale bars represent 40 μm.

The exploration into the phenomenon of spontaneous emulsification was motivated by observations during the work of Chapter 2, summarized by Figure 6.3. Spontaneous emulsification is defined here to mean the spontaneous formation of droplets near a liquid/liquid interface without addition of mechanical energy or

application of a thermal gradient. The plot shows steady-state interfacial pressure, Π, with bulk concentration, C_b, for five PEO/PDMS block copolymers (adapted from Figure 2.1). Although spontaneous emulsification has been observed with these surfactants with silicone oil/water interfaces, all data shown here are for dodecane/water interfaces. The colored points show the conditions that correspond with spontaneous emulsification (droplet formation) near the interface in the microtensiometer. The images show interfaces during spontaneous emulsification with diblocks E_6D_{29} (●,○) and $E_{39}D_{240}$ (×) and triblocks $E_6D_{80}E_6$ (▲,△) and $E_{11}D_{160}E_{11}$ (■). The diblock $E_{11}D_{80}$ (◆,◇) has not been observed to spontaneous emulsify oil/water interfaces. Unlike the other block copolymers, spontaneous emulsification is seen with $E_{39}D_{240}$ at every bulk concentration tested. Spontaneous emulsification is seen after these interfaces have reached steady state apart from $E_{39}D_{240}$ that emulsifies rapidly. The values of Π shown for $E_{39}D_{240}$ (×) correspond with steady-state measurements albeit with spontaneous droplets present.

The images in Figure 6.3 show that the spontaneous droplets have a diameter of at most ~10 μm and manifest differently among the surfactants. For example, the droplets in the image with $C_b = 10^{-6}$ mol/L $E_{39}D_{240}$ (d) are small and uniformly distributed across the entire interface. This contrasts with the droplets for $C_b = 10^{-2}$ mol/L $E_{11}D_{160}E_{11}$ (e) which are larger, less uniform in size and localized near the capillary. Spontaneous droplets appear in the oil for diblocks (b-d) and in the water for triblocks (e-g). The position of the droplets relative to the two phases is independent of the curvature of the interface at the tip of the capillary as shown by (b, c) with E_6D_{29} and (f, g) with $E_6D_{80}E_6$. As the curvature of the
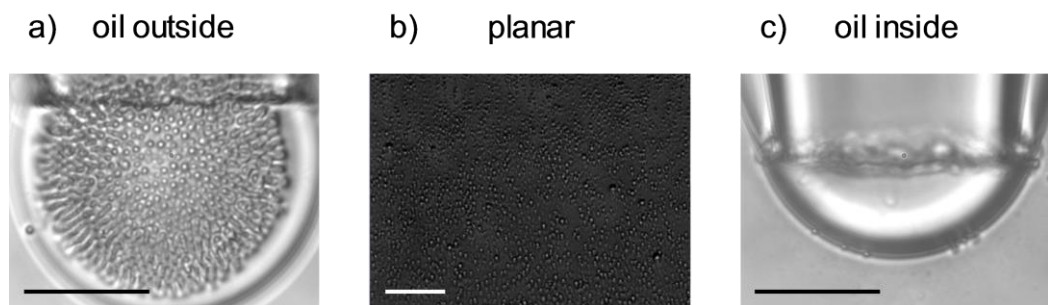
Figure 6.4. Spontaneous emulsification of dodecane/water interfaces with $C_b = 10^{-2}$ M $E_6D_{80}E_6$ after two hours. Images were taken on the microtensiometer for (a) surfactant/oil outside (convex) and (c) surfactant/oil inside (concave). (b) The planar image was taken of the midpoint of an oil/water interface in a glass vial. The scale bars represent 40 μm.

captive interface changes from concave to convex, the ratio of the volumes of the two liquid phases changes by six orders of magnitude—the volume of fluid within the capillary is O(nL) compared with the reservoir volume of O(mL).

The size, homogeneity and position of the spontaneous droplets do not depend simply on bulk concentration or steady-state interfacial properties. Spontaneous emulsification occurs over four orders of magnitude of bulk concentration from $C_b = 10^{-6}$ mol/L $E_{39}D_{240}$ to $C_b = 10^{-2}$ mol/L with E_6D_{29}, $E_6D_{80}E_6$ and $E_{11}D_{160}E_{11}$. Likewise, steady-state interfacial pressure and dilatational modulus provide no indication of whether an interface will spontaneously emulsify with these surfactants. Shown by Figure 6.3, spontaneous emulsification occurs across a wide range of interfacial pressure from $\Pi = 11$ mN/m for $E_{39}D_{240}$ to $\Pi > 40$ mN/m for E_6D_{29} and $E_6D_{80}E_6$. Figure 2.3 shows that the dilatational modulus, E, covers the entire range of values measured with $|E^*| < 3$ mN/m for E_6D_{29} to $|E^*| = 52$ mN/m for $E_{11}D_{160}E_{11}$. Measurements of E were taken after interfaces had reached steady state which occurred prior to the observation of the spontaneous droplets. Although the maximum surface coverage, Γ_∞, varies among the

surfactants (provided in Table 2.2), spontaneous emulsification is always observed within the linear region of the adsorption isotherm. In other words, the coverage of adsorbed surfactant is near its thermodynamic limit, Γ_∞. As an aside, the slope of high-C_b data of $E_{39}D_{240}$ is consistent with the packing arguments made with modified-SF theory in Chapter 2, having a lower slope than $E_{11}D_{80}$. This shows that a single adsorbed molecule of $E_{39}D_{240}$ occupies more interfacial area than one of $E_{11}D_{80}$, consistent with a packing limitation introduced by the larger PDMS brush.

Although the composition of the spontaneous droplets has not been measured directly, it is assumed that the droplets are primarily composed of the immiscible liquid. Figure 6.3b shows droplets within the oil for $C_b = 10^{-3}$ mol/L E_6D_{29}. This image contrasts with the others in Figure 6.3 because the focus has been shifted to the bottom of the spherical cap. At the time at which the image was taken, spontaneous droplets are only visible towards the bottom of the interface. This is consistent with a water-in-oil (W/O) emulsion whose droplets have sedimented under gravity given the density difference between dodecane ($\rho_d = 750$ g/mL) and water ($\rho_w = 998$ g/mL). The density difference works oppositely for oil-in-water (O/W) emulsions where oil droplets in water would rise under their own buoyancy.

Figure 6.4 shows the spontaneous emulsification of three dodecane/water interfaces with $C_b = 10^{-2}$ mol/L $E_6D_{80}E_6$ at three distinct interfacial curvatures: a) convex, b) planar and c) concave. The images with curved interfaces were taken in the microtensiometer, and the planar image was taken at the midpoint of a

macroscopic dodecane/water interface in a glass vial. The planar interface was formed by gently pipetting 1 mL of water then 1 mL of surfactant solution into a glass vial. No emulsion droplets were recorded initially. Images were taken two hours after the formation of the interfaces. As noted previously, the size and homogeneity of the droplets does not depend on the curvature of the interface with a droplet diameter $d_e \approx 5$ μm. It is not possible to tell the composition of the droplets from the middle image, but the position of droplets near the curved interfaces suggests an O/W emulsion as shown in Figure 6.3.

Although the size of the spontaneous droplets does not depend on interfacial curvature, the number of droplets observed at two hours does vary with curvature. The number of spontaneous droplets is quite numerous for convex (a) and planar (b) interfaces, and the number of droplets is far lower for the concave interface (c). In fact, the prevalence of spontaneous droplets at two hours for the concave interface (Figure 6.4c) is similar to that of the convex interface after approximately 15 minutes (Figure 6.3g). Clearly interfacial curvature impacts the rate of spontaneous emulsification without changing the nature of the droplets. In fact, the rate of emulsification in Figure 6.4 correlates with the effect of geometry on diffusion-limited surfactant adsorption where transport from within the spherical cap is significantly slower than transport from outside the cap or to a planar interface.[19] This suggests that the rate of spontaneous emulsification is controllable by varying molecular transport to the interface which is the focus of the following section.

### 6.3.2 Controlling spontaneous emulsification with a silicone polyether
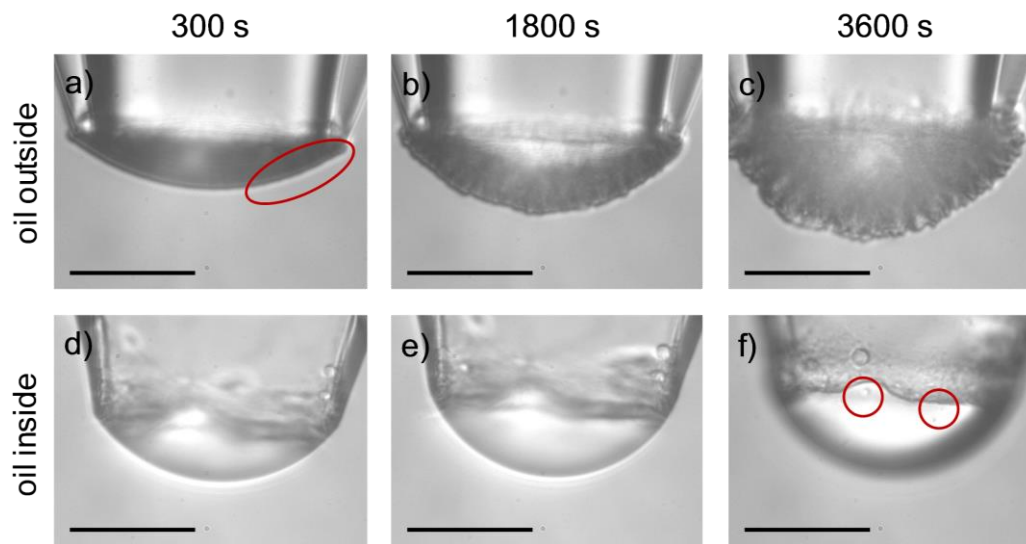
Figure 6.5. Spontaneous emulsification of dodecane/water interfaces with $C_b = 0.1$ wt % R-LL for (a-c) R-LL/oil outside and (d-f) R-LL/oil inside the capillary. Interfaces were monitored for an hour with images shown for interfacial ages of 300 s (a,d), 1800 s (b,e) and 3600 s (c,f). Red circles highlight the earliest observations of spontaneous emulsification. The scale bars represent 40 μm.

Spontaneous emulsification has been previously observed with the silicone polyether R-LL at the interface of water and cyclic silicones.[20] Similar to the diblocks and triblocks in the previous section, R-LL also emulsifies dodecane/water interfaces. The remainder of the work in this chapter focuses on data with R-LL because of limited availability of the diblock and triblock surfactants discussed in the previous section. The price for this is that in using a commercial grade material. the precise relationship between molecular detail and the phenomenon is blurred. As such, all concentrations of R-LL solutions will be given on a mass basis.

R-LL was chosen as an acceptable surrogate for the previous system because of the similarity between its spontaneous emulsification and that seen with $E_6D_{80}E_6$. The impact of interfacial curvature on the rate of spontaneous emulsification of a dodecane/water interface with $C_b = 0.1$ wt % R-LL is shown in

Figure 6.5. The two rows correspond to different interfaces (top—oil outside, bottom—oil inside) tracked for one hour after formation. Spontaneous emulsification is first visible for the convex interface at 300 s and manifests as a roughening of the interface, highlighted by the red ellipse. The droplets are present in the oil phase and grow in number as time progresses until they completely cover the interface. The bottom row shows that the rate of spontaneous emulsification is significantly slower for surfactant adsorbing from within the cap. For the concave interface, the first observation of spontaneous emulsification is at 3600 s, highlighted by the red circles. As with E_6D_{29}, focus has been shifted to the bottom of the liquid cap (Figure 6.5f). The spontaneous water droplets first appear towards the bottom of the less-dense oil.

Spontaneous emulsification with R-LL and $E_6D_{80}E_6$ is similar. The spontaneous emulsification occurs at large interfacial pressures ($\Pi > 40$ mN/m). Despite both concave and convex interfaces possessing the same interfacial pressure, the rate of spontaneous emulsification in Figure 6.5 is greater for the convex interface (oil outside) than for the concave interface (oil inside). The difference between R-LL and $E_6D_{80}E_6$ is the emulsion type. R-LL forms a W/O emulsion where $E_6D_{80}E_6$ forms an O/W emulsion. Despite this difference, the rate of emulsification still correlates with the diffusion-limited adsorption of the surfactant==oil/surfactant outside is faster than oil/surfactant inside. The stark difference in emulsification rate is not likely to be due to depletion of the surfactants to the interior glass surface of the capillary. If it is assumed that the surfactant adsorbs to the glass at a coverage of 1 g/m^2, then the solution concentration would
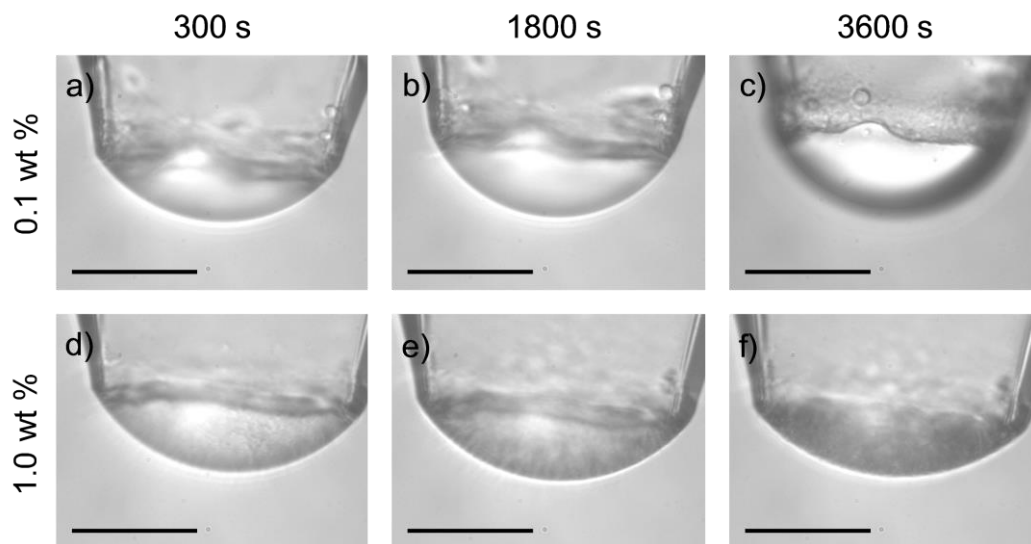
Figure 6.6. Spontaneous emulsification of dodecane/water interfaces with oil inside the capillary: (a-c) C_b = 0.1 wt % and (d-f) C_b = 1.0 wt % R-LL. Interfaces were monitored for an hour with images shown for interfacial ages of 300 s (a,d), 1800 s (b,e) and 3600 s (c,f). The scale bars represent 40 μm.

change by less than 1 %. This is corroborated by the large interfacial pressure (Π > 40 mN/m) that is the same for both convex and concave interfaces.

The rate of spontaneous emulsification can be increased at the concave interface (oil inside) by increasing the surfactant loading in the oil. Figure 6.6 compares the spontaneous emulsification for two concave, dodecane/water interfaces with C_b = 0.1 wt % (top) and C_b = 1 wt % R-LL (bottom) for one hour. At both surfactant concentrations, interfacial pressure is large (Π > 40 mN/m) and reaches its steady-state value within 100 s. The top images are those shown in Figure 6.5, showing the first observation of spontaneous emulsification at 3600 s. By increasing the concentration of R-LL to 1 wt %, spontaneous emulsification is seen as early as 300 s (Figure 6.6d). The emulsion droplets grow in time, which is seen as the darkening of the liquid cap in the bottom row of images. It is difficult to quantify this in order to compare to the convex interface with 0.1 wt % R-LL;
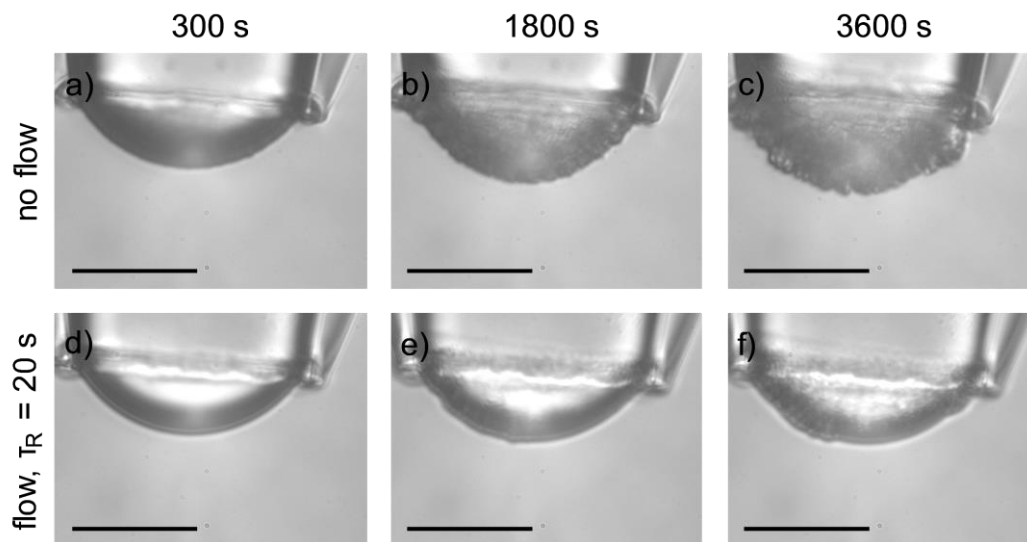
Figure 6.7. Spontaneous emulsification of dodecane/water interfaces using $C_b = 0.1$ wt% R-LL in the reservoir without (a-c) and with (d-f) flow recirculation ($\tau_R = 20$ s) in the microtensiometer reservoir. Interfaces were monitored for an hour with images shown for interfacial ages of 300 s (a,d), 1800 s (b,e) and 3600 s (c,f). The scale bars represent 40 μm.

however, these images suggest that surfactant inside the capillary must be approximately 10 times as concentrated as that outside the capillary to emulsify the interface at a similar rate. This is consistent with an interpretation that the rate of spontaneous emulsification depends on the transport of surfactant to the interface.

The rate of surfactant adsorption can be affected by several factors, not limited to interfacial curvature and bulk concentration. Not surprisingly, bulk convection (flow) has been shown to accelerate adsorption in diffusion-limited systems.[21] If the rate of spontaneous emulsification depends on the diffusion of surfactant to the interface as Figures 6.4-5 suggest, then flowing the oil within the microtensiometer reservoir should increase the rate of spontaneous emulsification of convex interfaces. Figure 6.7 compares the rate of spontaneous emulsification of a convex (oil outside), dodecane/water interface with $C_b = 0.1$ wt % R-LL with (bottom) and without flow (top). In the bottom images, flow occurred with a

110
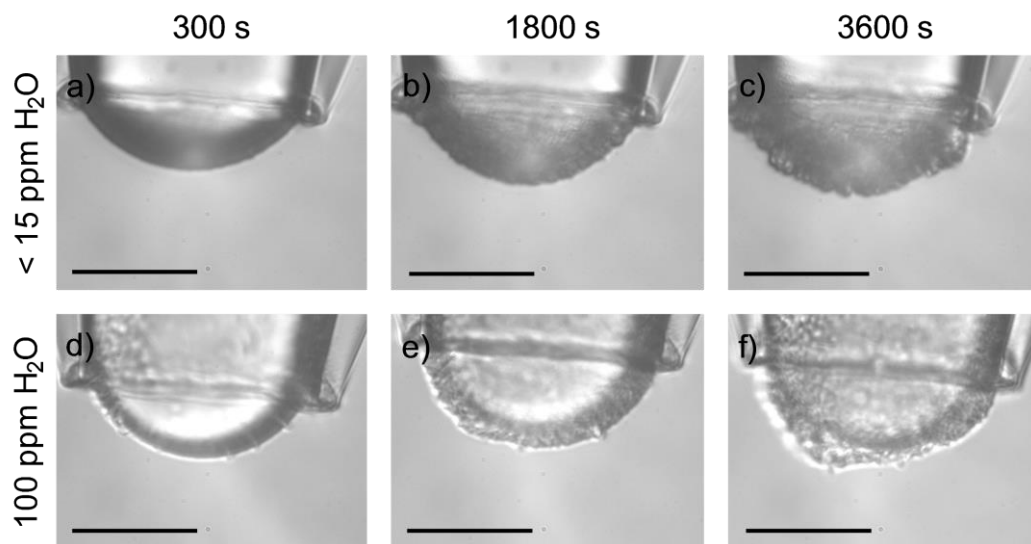
Figure 6.8. Spontaneous emulsification of dodecane/water interfaces using $C_b = 0.1$ wt% R-LL in the reservoir with water content in the oil (a-c) < 15 ppm and (d-f) = 100 ppm. Interfaces were monitored for an hour with images shown for interfacial ages of 300 s (a,d), 1800 s (b,e) and 3600 s (c,f). The scale bars represent 40 μm.

residence time $\tau_R = 20$ s (reservoir volume = 2 mL). Approximately 8 mL of R-LL solution was recirculated constantly using a peristaltic pump. The flow-in port of the reservoir is to the right of the images.

Figure 6.7 qualitatively shows the opposite of what was expected—the rate of spontaneous emulsification decreases during flow. The difference is particularly stark at 3600 s, where much of the interface in Figure 6.7f is bare. If the rate of emulsification were controlled only by the interfacial availability of surfactant, then the rate should have either increased or remained the same. The rate would have increased if transport were in a diffusion-limited or mixed regime and remained unchanged if transport were kinetically limited. While surfactant is certainly necessary to facilitate the emulsification, the droplets themselves are thought to be comprised primarily of the immiscible liquid, water. It is known that water is slightly soluble in oil, and convection in the oil would have the opposite effect on

111

the concentration of water in oil near the interface.[22] In the dodecane, water would be plentiful near the interface and less so further into the oil. Convection would accelerate the transport of water away from the interface, lowering its concentration in the oil near the interface. The water content of all R-LL solutions shown thus far has been measured with Karl-Fischer titration to be below 15 ppm, the lower limit of instrumental resolution. This is significantly lower than the concentration at saturation, which has been measured to be 72 ppm. The measurement of water-saturated dodecane was made by titrating dodecane after stirring with water and allowing the liquids to separate.

If the rate of spontaneous emulsification is limited both by transport of surfactant to the interface and transport of water into the oil, then saturating the R-LL solution with water prior to the measurement should increase the rate of emulsification compared with the drier R-LL solution. Figure 6.8 shows this comparison using dry (< 15 ppm water) and saturated (100 ppm water) $C_b = 0.1$ wt % R-LL solutions (convex interface, oil outside). The saturated solution was prepared by addition of liquid R-LL melt to pre-saturated dodecane to avoid the emulsification that results from mixing the R-LL solution with water directly. It is difficult to conclude from these images whether saturating the oil influences the rate of emulsification, although this appears to be the case. At 300 s, the interface with the saturated oil (Figure 6.8d) appears rougher than that with the dry oil (Figure 6.8a). Neither interface possesses any emulsion droplets initially at $t = 0$. At 3600 s, the saturated interface is less spherical than its dry counterpart. This

may be due to the increased number of droplets in the saturated case as the size and location of the droplets appear to be the same in both rows of images.

6.4 DISCUSSION

As mentioned in the introduction, spontaneous emulsification should only occur by one of two mechanisms—either micron-sized droplets pinch off from the interface, causing periodic disturbances in the Laplace pressure or interfacial curvature, or they grow from sub-micron nuclei in the oil, near the interface. Figure 6.9 shows Laplace pressure (a), radius of curvature (b), uncertainty in the fit of radius of curvature, δR, (c) and corresponding power spectra (d) for a spontaneously emulsifying, dodecane/water interface with $C_b = 0.1$ wt % R-LL as shown in Figure 6.5a-c. The sampling rate of the data is 15 s^{-1} with some points omitted from Figure 6.9a-c for clarity. Uncertainty in the radius is provided by an annulus fitting routine in LabVIEW® and gives the expected distance of the actual interface from the best-fit circle determined by minimizing δR within a prescribed region. Interfacial pressure is large and consistent throughout experiment ($\Pi > 40$ mN/m), resulting in relatively constant values of Laplace pressure (a) and radius of curvature (b). The sporadic spikes in R result from a temporary loss of focus as spontaneous droplets populate the oil near the interface. During the experiment, δR increases linearly with time, beginning near the usual value for dodecane/water ($\delta R = 0.3$ μm) and finishing approximately 10 times larger ($\delta R = 3 \pm 1$ μm). For a dodecane/water interface at this interfacial pressure that is not undergoing spontaneous emulsification, δR would remain low near its initial value of 0.3 μm.
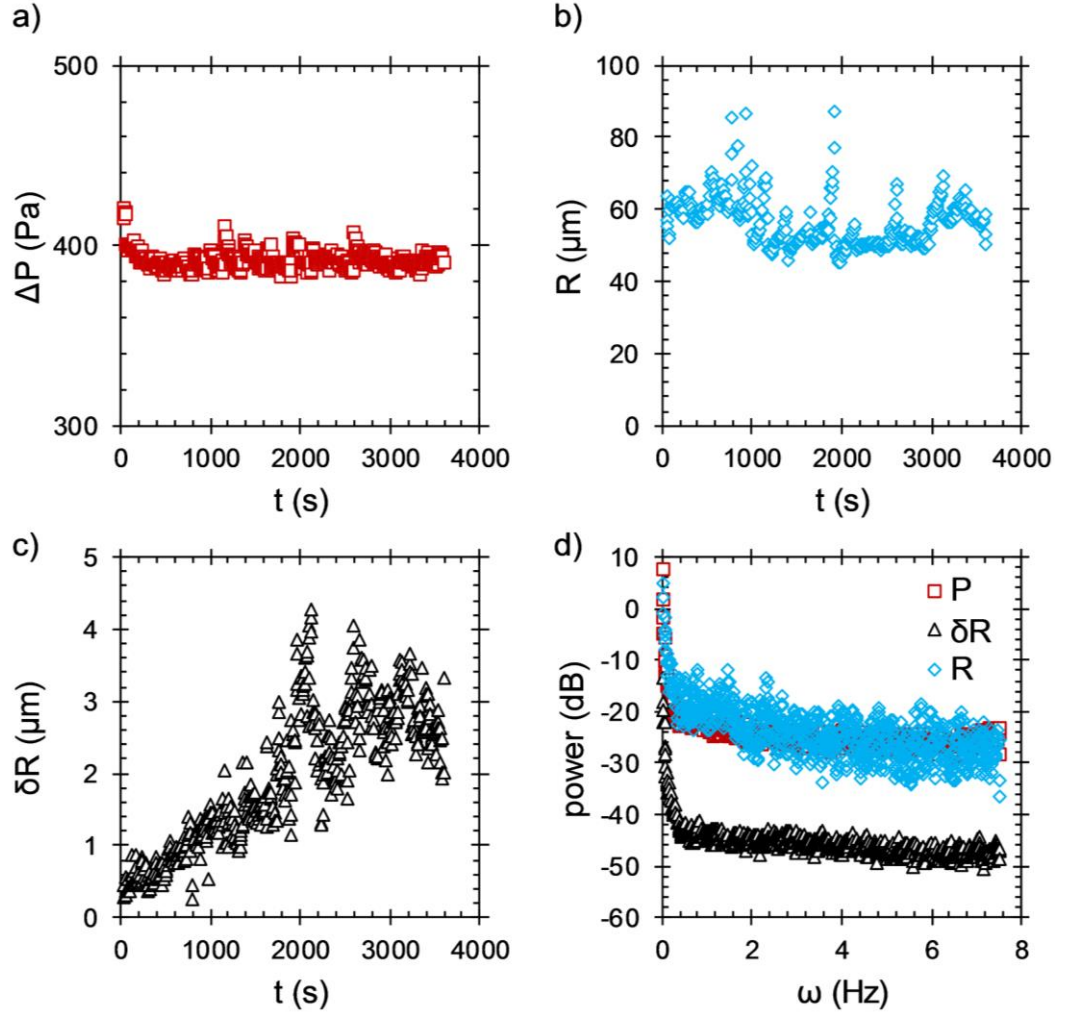
Figure 6.9. Signal analysis for the spontaneous emulsification of a dodecane/water interface with C_b = 0.1 wt % R-LL: (a) Laplace pressure, (b) radius of curvature of the pinned interface, (c) uncertainty in the fit of radius of curvature and (d) power spectra of (a-c) taken with a sampling rate of 15 s^{-1}. The data correspond with the images shown in Figure 6.5 (oil outside).

The spontaneous droplets observed in the corresponding micrographs (Figure 6.5a-c) have approximate diameters, $d_e \approx 5$ μm. If the micron-sized droplets form by pinch off from the larger interface, then this will be detected in either ΔP or R provided that the disturbance produced by pinch off of one or more droplets is sufficiently large compared to the signal noise. The uncertainty in ΔP is 10 Pa, and the uncertainty in R is given by δR. The effect of pinch off can be predicted with

114

the Laplace equation, Eq 1.1. At the measured interfacial pressure of 42 mN/m (γ = 10 mN/m), a spontaneous droplet with d_e = 5 μm will possess a substantially greater Laplace pressure than the larger interface, ΔP_e = 8000 Pa. However, the power spectrum of ΔP (Figure 6.9d, □) shows no evidence of any periodic disturbances. The power of the pressure signal is low and uniform (Gaussian) across most frequencies with an upturn in the low-frequency limit to the expected value for DC.

The radius signal can be analyzed in a similar way. A single droplet immediately after pinch off would possess a surface area, A_e, equivalent to that lost by the larger interface, ΔA, during the pinch off event. A droplet with d_e = 5 μm has a surface area A_e = 80 μm². The pinch off event would be detected as a fluctuation in R provided that the corresponding increase in R (due to ΔA) is greater than δR. This is true even if the spontaneous droplet has a much lower interfacial tension such that it possesses the same Laplace pressure as the larger interface. Detection is complicated by the steady increase in δR during the experiment. This is captured by calculating a minimum, detectable droplet diameter, d_{min}, by calculating the surface area of an emulsion droplet that would induce an increase in R by exactly δR. For the conditions shown in Figure 6.9, d_{min} increases from 1.8 μm to 2.8 μm throughout the experiment as δR increases from 0.3 to 4 μm. The value of capillary radius, R_c, in Figure 6.9 is 40 μm. The pinch off of micron-sized droplets seen in Figure 6.5 would be detected even at later times when the interface is coated with droplets, yet the power spectrum of R (Figure 6.9d, ◇) has the same

features as the spectrum of ΔP, showing definitively that spontaneous, micron-sized droplets do not pinch off the interface.

Despite not directly measuring the rate of spontaneous emulsification from either the pressure or radius signals, Figure 6.9c shows that the uncertainty in the radius signal correlates with the phenomenon. At short times before the appearance of any droplets, $\delta R = 0.3$ μm as expected for an oil/water interface. As the number of spontaneous droplets grow in the oil (Figure 6.7-8), δR increases with time. When interfacial curvature is reversed (oil inside the capillary), $\delta R = 0.3$ μm despite spontaneous emulsification (Figure 6.6). No physical meaning is assigned to the values of δR, but using δR is assumed to be a consistent measure of spontaneous emulsification across the various interfaces. R and d_e are similar among the interfaces, so the increase in δR during emulsification arises from the number of spontaneous droplets that disturb the interface's measured shape from a spherical cap.

Figure 6.10 shows the effect of flow on the rate of spontaneous emulsification as measured by an increase in δR with time for $C_b = 0.1$ wt % R-LL (oil in the reservoir). The data correspond with the images shown in Figure 6.7 with flow ($\tau_R = 20$ s, □,△,◇) and without flow (●,■,▲,◆) in the reservoir. One interface was monitored without flow prior to the flow experiments as a control (●). Initially, no spontaneous droplets are present ($\delta R = 0.3$ μm), and δR increases with time both with and without flow. δR increases more rapidly without flow than with flow, agreeing with qualitative observations in Figure 6.7. On average, δR is twice as large for interfaces that do not experience flow. Comparison of the slopes of
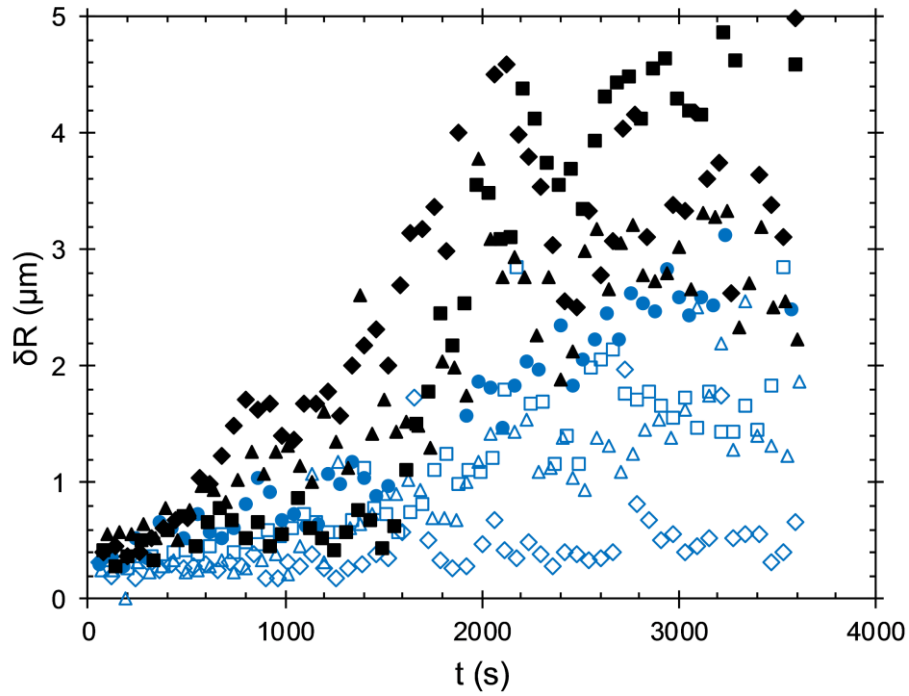
Figure 6.10. Uncertainty in the fit of radius of curvature for one hour during the spontaneous emulsification of dodecane/water interfaces with $C_b = 0.1$ wt % R-LL with ($\square,\triangle,\diamond$) and without ($\bullet,\blacksquare,\blacktriangle,\blacklozenge$) flow in the reservoir.

best fit lines for data with and without flow show a statistically significant difference ($p < 0.05$, details in Table 6.1).

The same comparison can be done between the experiments with $C_b = 0.1$ wt % R-LL for $C_w < 15$ ppm and $C_w = 100$ ppm. Figure 6.11 shows the rate of spontaneous emulsification as measured by the increase in δR for dry ($\square,\triangle,\diamond,\bullet,\blacksquare,\blacktriangle,\blacklozenge$) and saturated ($\color{red}\blacksquare,\blacktriangle,\blacklozenge$) reservoirs. The data for dry solutions have been replotted from Figure 6.10. The difference between dried and saturated R-LL solutions is more pronounced than the difference between flow and no-flow conditions. The interfaces in contact with saturated solutions begin with the expected $\delta R = 0.3$ μm, but δR increases more rapidly than in the other two cases.

117
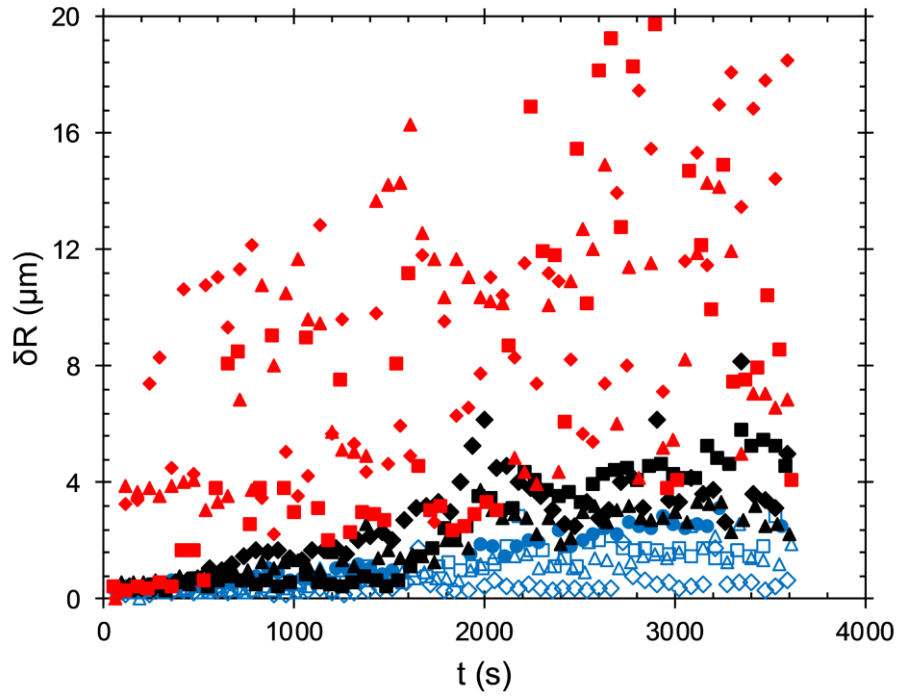
Figure 6.11. Uncertainty in the fit of radius of curvature for one hour during spontaneous emulsification of dodecane/water interfaces with $C_b = 0.1$ wt % R-LL. Empty ($\square,\triangle,\diamond$) and filled ($\bullet,\blacksquare,\blacktriangle,\blacklozenge$) points have been replotted from Figure 6.10 and describe spontaneous emulsification with and without flow in the reservoir, respectively. The black and blue points show data for dodecane initially with water content $C_w < 15$ ppm. The red points show data for dodecane (no flow) with initial water content $C_w = 100$ ppm ($\blacksquare,\blacktriangle,\blacklozenge$).

δR fluctuates more rapidly and over a wider range for the saturated solutions. The large fluctuations are likely due to the rapid pace of spontaneous emulsification, necessitating frequent focus adjustments to keep δR at its smallest value. Throughout the hour of emulsification, δR of the saturated experiments in approximately 10 times greater than that of the dry experiments. This is captured by a statistically significant difference between the slopes of the two no-flow cases ($p < 0.001$, details in Table 6.1), greater than that observed between the two dry cases.

As mentioned in the discussion of Figures 6.5-7, the observed changes in the rate of spontaneous emulsification with interfacial curvature, convection in the reservoir and water-content in the R-LL solution are consistent with a mechanism that depends on both C_b and C_w. Figure 6.5 shows that the rate of spontaneous emulsification significantly diminishes when $C_b = 0.1$ wt % R-LL solution is within the capillary. In Figure 6.6, the rate of spontaneous emulsification increases when R-LL loading increases tenfold to $C_b = 1$ wt %. Measurements of interfacial pressure at short times are high ($\Pi > 40$ mN/m) for all three interfaces. As interfacial pressure is a measurement of the amount of adsorbed surfactant, indistinguishable interfacial pressures suggests that adsorbed surfactant does not play a direct role in the emulsification, consistent with the spectral analysis in Figure 6.9. However, surfactant is still necessary for the emulsification. For a slower transport regime with R-LL solution inside the capillary, emulsification is slower than for the faster transport regime with R-LL solution in the reservoir.[23] The rate of emulsification for R-LL solution inside the capillary is accelerated by

Table 6.1. Details of linear regressions performed on data in Figures 6.11-12 for experiments without flow, with flow ($\tau_R = 20$ s) and with a water-saturated R-LL solution. Lines were fit of the form $\delta R = mt + \delta R_0$ where m is the slope and δR_0 prescribes the initial uncertainty, 0.3 μm.

	no flow		flow, $\tau_R = 20$ s		$C_w = 100$ ppm	
experiment	m ($\mu m/h$)	R^2	m ($\mu m/h$)	R^2	m ($\mu m/h$)	R^2
1	6.2	0.89	2.0	0.75	14	0.35
2	4.3	0.60	1.8	0.78	17	0.27
3	3.0	0.79	0.48	0.17	13	0.36
4	2.9	0.94				

increasing the C_b which hastens surfactant transport. If the surfactant is not diffusing to adsorb at the large interface at the capillary tip, then it must be diffusing to adsorb to the interfaces of the spontaneous droplets. The amount of interface created by the emulsification is substantial. For example, 100 droplets with $d_e = 5$ μm ($A_e = 80$ μm^2) doubles the total area of dodecane/water interface from $A = 8000$ μm ($R = 40$ μm) to 16000 μm.

As shown by Figures 6.7-8, surfactant is necessary for spontaneous emulsification but not sufficient. If only surfactant was required for the emulsification, then Figure 6.7 would see an increase in the rate of spontaneous emulsification for the flowing reservoir as convection accelerates surfactant transport to the interface. Instead, the opposite is observed—convection in the R-LL solution lowers the rate of spontaneous emulsification. This is the first evidence that the spontaneous droplets grow from surfactant-covered, aqueous nuclei in the oil near the interface. Flow convects the nuclei away from the interface before they grow into observable droplets. Far from the dodecane/water interface, the nuclei would not have access to the water within the capillary to grow into observable droplets. The experiment in Figure 6.8 adds validity to the nucleation and growth mechanism, showing that increasing the initial availability of water in the oil stimulates additional emulsification. Specifically, the initial rate of spontaneous emulsification spikes, shown by the sudden increase in δR at short times (Figure 6.11). It appears that saturating the oil dopes the solution with nuclei that are ready to grow into observable droplets shortly after contact with the larger, dodecane/water interface.
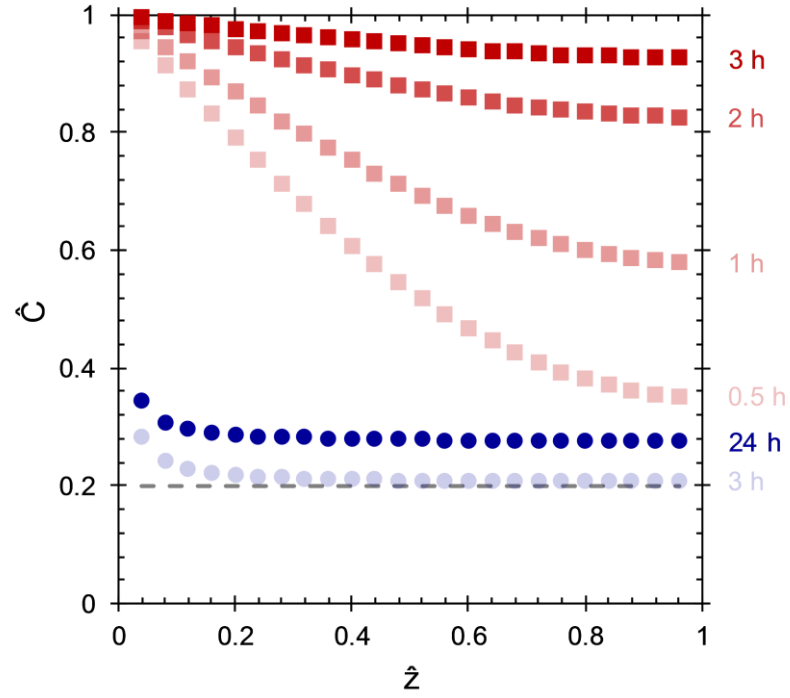
Figure 6.12. Numerical solution for unsteady diffusion of water into dodecane from planar (■) and concave (●) interfaces. Initial conditions are the same for both geometries, given with the dashed line. The time of each concentration profile is given to the right of the corresponding profile.

The nucleation-and-growth mechanism is corroborated by modeling the unsteady diffusion of water into the dodecane. Figure 6.12 shows numerical solutions using a boundary-value solver in MATLAB® to the scaled diffusion equation for planar (Eq 6.1, ■) and curved (Eq 6.2, ●) interfaces,

$$\frac{\partial \hat{C}}{\partial \hat{t}} = \frac{\partial^2 \hat{C}}{\partial \hat{z}^2} \tag{6.1}$$

$$\frac{\partial \hat{C}}{\partial \hat{t}} = \frac{1}{\hat{z}^2}\frac{\partial}{\partial \hat{z}}\left(\hat{z}^2 \frac{\partial \hat{C}}{\partial \hat{z}} \right) \tag{6.2}$$

with the following scalings for concentration $\hat{C} = C_w / C_w^{sat}$, time $\hat{t} = t \cdot D_w / l^2$ and

space $\hat{z} = z/l$. $\hat{C} = 1$ at the left boundary (at $\hat{z} = 0$ planar, $\hat{z} = 0.04$ curved) and

$\dfrac{\partial \hat{C}}{\partial \hat{z}} = 0$ at the right, $\hat{z} = 1$. The dashed line provides the initial condition ($\hat{C} = 0.2$)

corresponding to the maximum possible water content as measured by Karl Fischer

titration ($C_w = 15$ ppm) which is the same for both geometries. The times to the

right of the axes correspond with the nearest concentration profiles and were

calculated using $D_w = 2.5 \cdot 10^{-5}$ cm^2/s and $l = 1$ cm.[24]

Within three hours of diffusion from a planar interface (■), the oil is almost

uniformly saturated. Diffusion is much slower from a spherical interface (●, $R = 40$ μm) with $\hat{C}$ increasing only by 0.1 (7.5 ppm) in 24 hours. This is to be expected

as the spherical interface is surrounded by 10^3 times more fluid volume than is

adjacent to the planar interface with the same cross-sectional area as the sphere ($l = 1$ cm). As a result of the slow transport of water away from the spherical

interface, small nuclei that are convected away from the interface (Figure 6.7) will

find insufficient water in the bulk to continue their growth. It also follows from the

slow transport of water that saturation prior to the experiment (Figure 6.8)

noticeably effects the rate of spontaneous emulsification. Within three hours, little

water has penetrated into the oil, explaining why the rate of spontaneous

emulsification for dry oil without flow (Figure 6.5a-c, 6.10) does not increase for

subsequent interfaces. The three, one-hour experiments were conducted back to

back without any change in the rate of spontaneous emulsification.

6.5 SUMMARY

The mechanism behind spontaneous emulsification in surfactant/oil/water systems has eluded understanding for decades. With the exception of so-called "Ouzo effect" systems, little work had been done to ascertain the origins of the spontaneous droplets. The present work has determined that the spontaneous emulsion formed in the oil-soluble, silicone polyether R-LL/dodecane/water system results from the growth of small, aqueous nuclei in the oil rather than by the pinch-off of micron-sized droplets from the larger oil/water interface. The rate of the emulsification depends on both the concentration of the emulsifying surfactant to stabilize the droplet interface and the water in the oil to grow the droplets. As such, the rate of spontaneous emulsification can be controlled by interfacial processing. Emulsification can be effectively turned off by slowing the transport of the emulsifier to the interface whereas increasing the concentration of R-LL hastens the transport of surfactant to the interface and increases the rate of spontaneous emulsification. Controlling the gradient of water in the oil is also effective in changing the rate of spontaneous emulsification. By flowing the oil phase across the interface, the rate of spontaneous emulsification slows as the aqueous nuclei are convected away from their water source, unable to grow in the bulk. Saturating the oil with water prior to exposure to the bulk water in the microtensiometer has the opposite effect and increases the rate of spontaneous emulsification. This is especially noticeable at short times, likely by pre-forming aqueous nuclei prior to exposure to the bulk water. This chapter stops short of defining the driving force for spontaneous emulsification but motivates continued

study of surfactant self-assembly in oils that specifically focuses on the role water

plays in the structure and formation kinetics of the aggregates.

(1)   *Encyclopedia of Emulsion Technology vol 2*; Becher, P., Ed.; Dekker: New York, 1987.

(2)   Bonn, D.; Ross, D. *Reports Prog. Phys.* **1999**, *62*, 969–1033.

(3)   Palierne, J. F. *Rheol. Acta* **1990**, *29* (3), 204–214.

(4)   Barnes, H. A. *Colloids Surfaces A Physicochem. Eng. Asp.* **1994**, *91* (C), 89–95.

(5)   Princen, H. M. *J. Colloid Interface Sci.* **1983**, *91* (1), 160–175.

(6)   Davies, J.; Rideal, E. *Interfacial Phenomena*, 2nd ed.; Academic Press Inc., 1963.

(7)   Miller, C. A. *Colloids and Surfaces* **1988**, *29* (1), 89–102.

(8)   López-Montilla, J. C.; Herrera-Morales, P. E.; Pandey, S.; Shah, D. O. *J. Dispers. Sci. Technol.* **2002**, *23* (1–3), 219–268.

(9)   Solans, C.; Morales, D.; Homs, M. *Curr. Opin. Colloid Interface Sci.* **2016**, *22*, 88–93.

(10)   *Microemulsions and Related Systems*; Bourrel, M., Schechter, R., Eds.; Dekker: New York, 1988.

(11)   Shahidzadeh, N.; Bonn, D.; Meunier, J. *Europhys. Lett.* **1997**, *40* (4), 459–464.

(12)   McBain, J.; Woo, T. *Proc. R. Soc. A Math. Phys. Eng. Sci.* **1937**, *163* (A913), 182–188.

(13)   Rang, M.; Miller, C.; Hoffmann, H.; Thunig, C. *Ind. Eng. Chem. Res.* **1996**, *35* (9), 3233–3240.

(14)   Ruschak, K. J.; Miller, C. A. *Ind. Eng. Chem. Fundam.* **1972**, *11* (4), 534–540.

(15)   Vitale, S. A.; Katz, J. L. *Langmuir* **2003**, *19* (10), 4105–4110.

(16)   Silva, P. S.; Zhdanov, S.; Starov, V. M.; Holdich, R. G. *Colloids Surfaces A Physicochem. Eng. Asp.* **2017**, *521*, 141–146.

(17)   Bochner De Araujo, S.; Merola, M.; Vlassopoulos, D.; Fuller, G. G. *Langmuir* **2017**, *33* (40), 10501–10510.

(18)   Dimitrova, T. D.; Saulnier, L.; Verhelst, V.; Van Reeth, I. *ACS Symp. Ser.* **2010**, *1053*, 243–265.

(19)   Alvarez, N. J.; Walker, L. M.; Anna, S. L. *Phys. Rev. E - Stat. Nonlinear, Soft Matter Phys.* **2010**, *82* (1), 1–8.

(20)   Anseth, J. W.; Bialek, A.; Hill, R. M.; Fuller, G. G. *Langmuir* **2003**, *19* (16), 6349–6356.

(21)   Alvarez, N. J.; Vogus, D. R.; Walker, L. M.; Anna, S. L. *J. Colloid Interface Sci.* **2012**, *372* (1), 183–191.

(22)   Bleier, B. J.; Anna, S. L.; Walker, L. M. *J. Phys. Chem. B* **2018**, *122* (14), 4067–4076.

(23)   Alvarez, N. J.; Walker, M.; Anna, S. L. *Soft Matter* **2012**, *8*, 8917–8925.

(24)   Su, J. T.; Duncan, P. B.; Momaya, A.; Jutila, A.; Needham, D. *J. Chem. Phys.* **2010**, *132* (4).

CHAPTER 7

CONCLUSIONS AND FUTURE WORK

7.1 CONCLUSIONS

This thesis has shown the utility of interfacial processing both in augmenting classical tests of adsorption as well as in quantifying and controlling a complex, interfacial phenomenon, spontaneous emulsification. Interfacial processing can mean several things, all of which introduce an additional experimental timescale. Interfacial processing has been used to test adsorption reversibility, the ability of an adsorbed surfactant to desorb from the interface as the concentration in the bulk is lowered. Interfaces have been processed along a gradient of solvent quality, promoting adsorption in poor solvents and stranding adsorbed surfactants with a nonsolvent. Interfaces have been processed sequentially to study changes in strongly adsorbed layers with solvent composition. Finally, interfacial processing has been used to control the rate of spontaneous emulsification, providing necessary evidence to determine the mechanism of spontaneous emulsification of oil/water interfaces with an oil-soluble surfactant.

Testing adsorption reversibility is one of the simplest forms of interfacial processing. This test measures the timescale of desorption of a surfactant, which can be calculated from adsorption dynamics but never measured and determines whether an adsorbed surfactant is truly at equilibrium with the bulk. Isotherm models like those used in Chapters 2 and 3 are only valid for so-called reversibly adsorbed, or soluble, surfactants. As shown in Chapter 2 by testing the local adsorption reversibility of PEO-PDMS block copolymers, measuring desorption

dynamics provides additional insight into the relaxation of dilatational stresses. For the molecules studied, desorption occurs too slowly to relax these stresses, so the source of the relaxation must be from the reorientation of the adsorbed surfactant. In Chapter 3, desorption measurements provide a compositional probe of the interface after exposure to a solution containing pCTVB aggregates. Following adsorption from a solution of the aggregates, desorption dynamics for interfacial pressure plateau to a finite value, contrasting with those with CTAB alone (no aggregates) which return to the clean value prior to any adsorption. This demonstrates that the entire aggregate adsorbs to the air/water interface instead of merely leeching CTA^+, corroborated by the measurements of dilatational elasticity.

In Chapter 5, the irreversible adsorption of the PEO-HFBMA particles enables additional processing. Because interfacial tension changes little when the interface is rinsed with solvent (water) or Na_2SO_4 solutions, it has been assumed that the number of particles on the interface remains constant throughout the processing. With this assumption, the nonlinear dilatational response of an interface titrated with several salt concentrations has been interpreted as a decrease in the size of adsorbed particles with increasing salt concentrations, as has been seen in the bulk. The polyelectrolyte-surfactant aggregates in Chapter 3 have been processed in a similar way using CTAB. The pCTVB aggregates adsorb strongly and leave behind an interfacial layer enriched in polyelectrolyte after the interface is rinsed with water. When these interfaces are rinsed with dilute CTAB, interfacial tension restores to its pre-rinse value. For the amount of CTAB used, interfacial tension will not reach the measured value at a bare air/water interface that the

polyanion-coated interface achieves. Not surprisingly, the polyanion provides additional driving force for the adsorption of the cationic surfactant, demonstrating that there is an equilibrium between free CTA^+ and CTA^+ with polyanion at the interface, similar to the equilibrium between free CTA^+ and aggregates in the bulk.

Interfacial processing is not limited to the back end of an experiment but can be used to control adsorption to a bare interface as well. In Chapter 4, the adsorption of four amphiphilic polypeptoids has been controlled by varying solvent quality. Initially, no adsorption is seen from a good solvent (50/50 mixture of acetonitrile/water) to the air/solution interface. By diluting the solution with pure water to 25/75 ACN/water, polypeptoids adsorb to modest surface pressures. By rinsing these interfaces with a nonsolvent (pure water), irreversibly adsorbed layers develop with large surface pressures. Next to a nonsolvent, adsorbed polypeptoids exhibit stronger dilatational responses that vary with subtle changes in molecular sequence. The sequence-dependence of the dilatational response only manifests after the polypeptoid-laden interfaces have been processed with the nonsolvent.

Determining the mechanism of spontaneous emulsification with PDMS-containing copolymers is made possible with interfacial processing. Steady state (near equilibrium) measurements of interfacial pressure and dilatational elasticity are no help in predicting the phenomenon. Dodecane/water interfaces are seen to spontaneously emulsify over a wide range of interfacial pressure, dilatational elasticity and solution concentration. Careful inspection of Laplace pressure and radius of curvature of the captive interfaces with FFT does not show the periodic disturbances that would be evident from the pinch off of the emulsion droplets,

suggesting that the microscale droplets grow from small nuclei near the larger interface. By varying the gradients of surfactant and water in the oil, the rate of spontaneous emulsification can be controlled. Specifically, the rate of spontaneous emulsification has been decreased by flowing the surfactant solution over the oil/water interface. Convection accelerates the transport of surfactant to the interface but also transports the aqueous, pre-emulsion nuclei deeper into the oil phase (and away from the water), thus lowering the rate of spontaneous emulsification.

7.2 FUTURE WORK

The work contained within this thesis is ripe for continuation and falls into roughly one of two categories, with some overlap. The first category focuses on the first goal outlined in Section 1.1 by suggesting first steps to test many of the physical interpretations made in this thesis. These recommendations include alterations to surfactant structure and composition. The second category focuses on the second goal, employing interfacial processing to explore interfacial phenomena. This is suggesting as extending the techniques established in this thesis to additional phenomena or by using them to precisely control spontaneous emulsification.

Despite the widespread industrial use of oil-soluble surfactants, the majority of published, interfacial data is with water-soluble surfactants. Chapter 2 provides a useful launch point to study the effects of chain flexibility on interfacial properties of oil-soluble block copolymers. Substitution of the methyl groups along the Si-O backbone in the PDMS with an alkane or an aromatic will increase chain stiffness

both in solution and in the brush region that forms in the oil at the oil/water interface.

In Chapter 3, a crucial finding is that CTA^+ controls the adsorption of the aggregate while the aggregate size sets the diffusion timescale and adsorption time, suggesting that pCTVB aggregates can be tuned to precisely control interfacial properties. This can be readily tested by synthesizing aggregates of various lengths and hydrophobicity. For example, reducing aggregate size by lowering the concentration of free-radical initiator during synthesis should hasten adsorption dynamics without affecting steady-state interfacial tension or dilatational elasticity. However, preserving aggregate length but decreasing the number of carbons in the CTA^+ (e.g., from 16 to 12) should simultaneously increase steady-state interfacial tension and decrease dilatational elasticity. In other words, the 12-carbon aggregates will be more hydrophilic and less capable of delivering polyanion to the interface than the 16-carbon aggregates of the same length.

The polypeptoids in Chapter 4 show sequence-dependent, dilatational elasticities after the polypeptoid solution is exchanged with a nonsolvent, water. It was proposed that this difference could be due to a difference in the strength of hydrophobic interactions of the adsorbed molecules. This can be tested by changing the hydrophobic R group to a larger alkane or aromatic. Conversely, if the dilatational elasticity is due to the hydrophilic R group of the polypeptoids, then elasticity could be increased by increasing the size of the PEO group.

Irreversibly adsorbed particles show potential to study coalesce of fluid/fluid interfaces. In Chapter 5, the PEO-HFBMA particles remain adsorbed to

131

the oil/water interface during large-amplitude compressions while titrated with Na$_2$SO$_4$. At large interfacial areas and small surface coverages coalescence may occur more easily than at larger surface coverages. The salt-responsiveness of the PEO-HFBMA system provides an additional means to control the surface coverage of the particles by changing the interfacial area occupied by a single particle.

In Chapter 6, the rate of spontaneous emulsification with R-LL of dodecane/water interfaces depends on the amount of water in the oil. By saturating the R-LL solution with water prior to the creation of the oil/water interface, the rate of spontaneous emulsification is increased. This suggests that precise control over the rate of spontaneous emulsification is available by controlling the saturation of water in the oil and the flux of the water into the oil. Using curved interfaces in the microtensiometer, water flux can be varied easily by changing interfacial curvature either with Laplace pressure or with smaller or larger capillaries. Increasing the saturation of water in the oil would require changing either the oil or changing the surfactant. To access water loadings in between the two extremes offered in Chapter 6, R-LL solutions could be equilibrated in a humid environment prior to experiment.